

THERMAL-HYDRAULIC OPTIMIZATION
FOR HIGH PRODUCTION OF LOW-ENRICHED
URANIUM BASED MOLYBDENUM-99

A Thesis
presented to
the Faculty of the Graduate School
at the University of Missouri-Columbia

In Partial Fulfillment
of the Requirements for the Degree
Master of Science

by
JEFF SCOTT
Dr. Gary Solbrekken, Thesis Supervisor

MAY 2009

The undersigned, appointed by the dean of the Graduate School, have examined the thesis entitled

THERMAL-HYDRAULIC OPTIMIZATION
FOR HIGH PRODUCTION OF LOW-ENRICHED
URANIUM BASED MOLYBDENUM-99

presented by Jeff Scott,

a candidate for the degree of master of science,

and hereby certify that, in their opinion, it is worthy of acceptance.

Professor Gary Solbrekken

Professor Yuwen Zhang

Professor Shi-Jie Chen

ACKNOWLEDGEMENTS

I would like to thank Dr. Gary Solbrekken for everything he has done to help me throughout the research process. His foresight was invaluable, and his constant patience and guidance provided an atmosphere that allowed this research to be accomplished. I would also like to thank Ron Govoro for his work leading up to this research, Kyler Turner for his insight, and Rachel Mahan for ensuring this thesis is readable, on the off chance someone would actually want to do so. Finally, I would like to thank Charlie Allen, Les Foyto, and all the people at MURR who are working hard to make this project a reality.

TABLE OF CONTENTS

Acknowledgements.....	ii
Nomenclature.....	vi
List of Illustrations.....	vii
List of Tables.....	xii
Abstract.....	xiii
Chapter 1: Introduction	
1.1 Motivation.....	1
1.2 Nuclear background.....	2
1.3 Thermal/neutronics background.....	7
1.4 Target design.....	8
1.5 Current reactor setup.....	12
Chapter 2: Objectives	
2.1 Past research.....	15
2.2 Goals.....	17
2.2.1 Hydraulic model for a single channel.....	18
2.2.2 Thermal model for a single channel.....	18
2.2.3 Evaluation of multiple channels.....	19
2.2.4 Maximizing heat transfer.....	19
Chapter 3: Boundary Conditions	
3.1 Hydrodynamic model - boundary conditions.....	21
3.2 Thermal model - boundary conditions.....	28

Chapter 4: Hydrodynamics – Resistance Network

4.1	Background.....	32
4.2	Hydraulic model for a single channel.....	33
4.3	Hydraulic model for multiple channels.....	46

Chapter 5: Heat Transfer – Resistance Network

5.1	Background.....	51
5.2	Single channel heat transfer.....	52
5.3	Multiple channel heat transfer.....	57

Chapter 6: Entropy Generation

6.1	Background.....	60
6.2	Hydrodynamic entropy generation.....	60
6.2.1	Entropy from friction.....	61
6.2.2	Entropy from minor losses.....	63
6.3	Thermal entropy generation.....	64

Chapter 7: Results & Discussion

7.1	Single channel results.....	67
7.1.1	Analytic model validation.....	67
7.1.2	Optimization.....	69
7.1.3	Resistor ratios.....	73
7.1.4	Target geometry.....	75
7.1.5	Saturation temperature.....	80
7.2	Multiple channel results.....	81
7.2.1	Analytic model validation.....	82

7.2.2	Optimization	83
7.2.3	Plate targets.....	91
Chapter 8: Conclusions.....		95
Chapter 9: Recommendations		
9.1	Enhanced cylinder geometry.....	97
9.2	Utilization of surroundings.....	99
Appendices		
A	FLUENT tutorial.....	101
B	Single channel Matlab code.....	116
C	Multiple channel Matlab code.....	124
References.....		135

NOMENCLATURE

<p>A area</p> <p>c specific heat, incompressible</p> <p>C undefined constant</p> <p>D diameter</p> <p>D_h hydraulic diameter</p> <p>E energy</p> <p>f friction factor</p> <p>f function matrix</p> <p>g gravity</p> <p>h heat transfer coefficient</p> <p>h enthalpy</p> <p>I turbulence intensity</p> <p>J Jacobian matrix</p> <p>k thermal conductivity</p> <p>k_p turbulent kinetic energy</p> <p>K contraction/expansion coefficient</p> <p>L target length</p> <p>\dot{m} mass flow rate</p> <p>n neutron</p> <p>n number of parallel channels</p> <p>P pressure</p> <p>\mathcal{P} perimeter</p> <p>q, \dot{Q} rate of heat transfer</p> <p>R radius</p> <p>R resistance</p> <p>s specific entropy</p> <p>\dot{S}_{gen} entropy generation rate</p> <p>T temperature</p> <p>u specific internal energy</p> <p>U_τ frictional velocity</p> <p>v specific volume</p> <p>V velocity</p> <p>W work</p> <p>x^i guess matrix</p> <p>y distance from wall</p> <p>z downstream length</p>	<p>α thermal diffusivity</p> <p>β^- beta particle (electron)</p> <p>γ gamma radiation</p> <p>ζ hydrodynamic losses</p> <p>θ temperature difference</p> <p>ν kinematic viscosity</p> <p>$\bar{\nu}_e$ antineutrino</p> <p>ρ density</p> <p>τ_w wall shear stress</p> <p style="text-align: center;">Subscripts</p> <p>a annular</p> <p>c cylinder (target)</p> <p>c contraction</p> <p>e expansion</p> <p>f fluid (water)</p> <p>fd fully developed</p> <p>i inner</p> <p>o outlet</p> <p>w wall</p> <p style="text-align: center;">Dimensionless Numbers</p> <p>Ma Mach number</p> <p>Nu Nusselt number</p> <p>Pr Prandtl number</p> <p>Re Reynolds number</p> <p style="text-align: center;">Abbreviations</p> <p>CFD computational fluid dynamics</p> <p>FNM flow network modeling</p> <p>HEU high-enriched uranium</p> <p>LEU low-enriched uranium</p> <p>MURR University of Missouri Research Reactor</p> <p>NTU number of transfer units</p>
--	---

LIST OF ILLUSTRATIONS

Figure	Title	Page
1.1	Two common target designs	9
1.2	Sketch of reactor core surrounded by wedges	12
1.3	Sketch of wedge currently used for testing	13
2.1	Flow chart of the steps which led to the final model	20
2.2	Sketch of reactor pool and flow channel of interest	18
3.1	Diagram of the reactor flow loop	21
3.2	Pressure distribution in the reservoir	23
3.3	Picture of anemometer probe assembly	24
3.4	Location of velocity measurement on anemometer	25
3.5	Driving pressure vs. measured velocity at anemometer	25
3.6	The three 2-D geometries examined in FLUENT	26
3.7	Mass flow rate vs. driving pressure across the N-1 channel for 3 cases	28
3.8	Thermal properties of the target for a constant heat flux at the LEU foil	30
3.9	Thermal properties of the target for a constant wall temperature	31

4.1	Simplified reactor flow loop	33
4.2	Comparison of pressure in FLUENT simulations with and without gravity	34
4.3	Single channel system with resistors	40
4.4	Diagram of flow around the target	41
4.5	Diagram of a 3-channel system	46
4.6	Hydraulic resistance network for a two channel system	47
4.7	Hydraulic diameters for 2 and 3 parallel channels	50
5.1	Axisymmetric representation of heat flow	51
5.2	Thermal resistance network for a two channel system	58
6.1	Energy boundary along a section of channel for friction	61
6.2	Energy boundary for a minor loss	63
7.1	Single channel model used to compare analytic and numeric results	67
7.2	Comparison of analytic and numeric mass flow rates for single channel	68
7.3	Comparison of analytic and numeric heat transfer rates for single channel	69
7.4	Heat transfer from a single channel for a variable drain diameter	70
7.5	Heat transfer from a single channel for a variable	71

	channel diameter	
7.6	Transition to laminar flow in the single channel model	72
7.7	Hydraulic resistor ratio for a variable channel diameter	74
7.8	Hydraulic resistor ratio for a variable drain diameter	75
7.9	Effect of target length on the rate of heat transfer with a varying drain diameter	77
7.10	Effect of target length on the rate of heat transfer with varying channel diameter	77
7.11	Effect of target length on the hydrodynamic resistor ratio	78
7.12	Total heat transfer vs. channel diameter for multiple outer diameters of the target. Drain = 0.04445m.	79
7.13	Total heat transfer vs. channel diameter for multiple outer diameters of the target. Drain = 0.060m.	79
7.14	Effect of saturation temperature on the heat transfer with varying channel diameter	80
7.15	Effect of saturation temperature on the heat transfer with varying drain diameter	81
7.16	Diagram of the numeric 3-dimensional model used to confirm the analytic model	82
7.17	Total heat transfer vs. number of channels using the existing drain diameter	84
7.18	Heat transfer per channel vs. number of channels using the existing drain diameter	84
7.19	Resistor ratio vs. number of channels for the existing drain diameter	85

7.20	Total heat transfer vs. number of channels for the existing channel diameter	86
7.21	Resistor ratio vs. number of channels for existing channel diameter	86
7.22	Total heat transfer vs. channel diameter for multiple channels. Drain = 0.100m.	87
7.23	Total heat transfer vs. channel diameter for multiple channels. Drain = 0.150m.	88
7.24	Heat transfer per channel vs. channel diameter for multiple channels. Drain = 0.100m	89
7.25	Heat transfer per channel vs. channel diameter For multiple channels. Drain = 0.150m	89
7.26	Heat transfer per channel vs. drain diameter For multiple channels.	90
7.27	Diagram of in-channel plate target configuration	92
7.28	Total heat transfer vs. drain diameter for plate target model	93
7.29	Total heat transfer vs. channel diameter for plate target model	94
9.1	Temperature contour around heated annular cylinder	97
9.2	Temperature distribution of the flow at varying downstream distances from the annular cylinder	98
9.3	Picture of target holder	100
A.1	A 2-D axisymmetric diagram of the reservoir with an empty N-1 channel	102
A.2	Demonstration of coarse and fine meshes	104

A.3	Union of quad and tri meshes	106
A.4	FLUENT boundary conditions window	109
A.5	Iteration process in FLUENT	111
A.6	Divisions of turbulent flow near wall	114

LIST OF TABLES

Number	Title	Page
3.1	Simulation parameters for determining minimum reservoir size	22
4.1	Element-by-element comparison of electrical and hydraulic systems	39
5.1	Element-by-element comparison of electrical and thermal systems	56
7.1	Resultant mass flow rates from specified static pressure drops for single channel	68
7.2	Dimensions currently used at MURR	70
7.3	Comparison of geometry and heat transfer rate for current and optimized single channel configurations.	73
7.4	Effect of target length on maximum rate of heat transfer	76
7.5	Comparison of the numeric and analytic data from a multiple channel simulation	83
A.1	Default vs. updated properties of water in FLUENT	108

ABSTRACT

Technetium-99m is currently the most widely used nuclear isotope in the medical field. Globally, more than 20 million samples are used annually to diagnose many different forms of cancer. Despite this, there are only four main nuclear reactors worldwide that produce molybdenum-99, the parent isotope of technetium-99m. In an attempt to address the growing demand, as well as to motivate the current reactors to stop using high-enriched uranium, the University of Missouri Research Reactor (MURR) has begun to produce molybdenum-99 using low-enriched uranium.

The fission of uranium-235, for which one of the products is molybdenum-99, generates approximately 2 kW of heat per 4-gram target. Continually removing this heat from the fission reaction is the limiting factor in the high-volume production process. The objective of this report is to find a reactor wedge setup with maximum rate of heat removal, thereby maximizing the amount of molybdenum-99 that can be created in the reactor.

To determine the best heat transfer, a quasi 1-D analytic model, calibrated numerically, is created to hydraulically and thermally model the coolant flow through the current reactor setup. Using flow network modeling (FNM), this analytic model is expanded to analyze other potential geometries that could maximize heat transfer. The findings show that for a single channel under the existing reactor configuration, a maximum of 19.18 kW can be dispersed. By opening the drain and slightly shrinking the

channel diameter, this can be improved to 22.77 kW. When the system is expanded to 10 parallel channels, the rate of heat transfer for the current drain and target geometries tops out at 47 kW. With changes to these parameters, this value can be raised to over 250 kW, though the neutronics of the MURR reactor may limit this. The final setup that is examined uses 8 plate targets in each of 3 parallel channels. The optimum rate of heat transfer for this configuration is 190 kW.

Chapter 1

INTRODUCTION

1.1 Motivation

Each year in the United States, almost 1.3 million people are diagnosed with cancer (Hayat, 2008), many of whom will die from it. In an effort to cure current cases and prevent future ones, many measures have been taken; however, since there are more than 100 types of cancer (Hayat, 2008), a global cure proves to be a daunting task. Still, regardless of the final treatment, the first step must always be detection of the problem. In the last 50 years or so (Williams, 1976), nuclear medicine has become a serious contender for this task. Radioisotopes such as rubidium-82 and thallium-201 have both been utilized in an attempt to detect cancer earlier and with a better accuracy than ever before.

Perhaps the most promising nuclear medicine of all, technetium-99m is used in about 85% of all diagnostic procedures that involve nuclear medicine. Worldwide, this translates to more than 20 million samples used every year, with more always in demand. Unfortunately, as a product of nuclear fission, technetium-99m is only able to be produced by governments or companies that have enough resources to make the initial investment and are not restricted to do so by outside factors. Currently, this is limited to only a few reactors worldwide: HFR (Petten) in the Netherlands, BR2 in Belgium, NRU in Canada, and SAFARI-1 in South Africa, as well as a few others. With so few locations

able to create this radioisotope, when one of the reactors stops producing, whether due to routine maintenance or because of a more serious problem, the global production of technetium-99m decreases sharply. This problem is emphasized by the realization that, due to the short nuclear life spans of the materials in question, a backup supply of more than two weeks cannot be accumulated. Recognizing the potential gap in production, the University of Missouri Research Reactor (MURR) is attempting to establish a domestic production source of technetium-99m through the use of low-enriched uranium (LEU). Since MURR was not initially designed for this purpose, analysis is necessary to show either that the current reactor setup can support this project or what alterations are necessary.

1.2 Nuclear Background

While there are many factors that determine if a material should be used as radiopharmaceutical, none is more important than the health and safety of the patient. If the examination method does more harm than the problem being observed, then the patient is no better off in the end. As such, the types and amounts of radiation being expelled from the decay process must be understood before the radioisotope can be administered to the patient. For technetium-99m, the chain begins with low-enriched uranium. With a half life of 7.04×10^8 years (Table of nuclides, 2008), uranium-235 decays extremely slowly and therefore has a relatively low activity when left to itself. However, in a high neutron flux, such as near the core of a nuclear reactor, the uranium begins to undergo fission.

One of the many products that results from uranium-235 fission is molybdenum-99. As with all unstable isotopes, the molybdenum continues to decay naturally until it finally becomes stable. This is not done, though, in a single step. After only a few days of becoming molybdenum-99, a significant amount of the mass will have already converted into a metastable form of technetium via negative beta decay,



at which point it is finally ready to administer to the patient. Here, $\bar{\nu}_e$ represents an antineutrino, which plays no significant part in the research. Because the technetium-99m begins to decay and release gamma rays immediately through the reaction



scans of the patient with a gamma camera can begin as soon as the tracer reaches its destination. Typically, this takes only a few minutes.

While having only a short time to wait is convenient, the reaction in Eq. (1.2) is more important for what it does not contain. Since the technetium is progressing from a metastable state to a ground state of the same element, there are no protons, neutrons, or electrons emitted. This means that there is no alpha or beta radiation present in the reaction. Outside the body, alpha and beta radiation are relatively harmless, as the skin prevents them from entering the body. In the case of a radiopharmaceutical, though, any tracers given to a patient will be through injection, ingestion, or inhalation, causing them to bypass the defenses of the skin. Being relatively short-ranged, any alpha or beta

radiation generated by the decaying isotope will be quickly absorbed by nearby organs, bones, and muscles with potentially detrimental effects to the patient. Since neither of these types of radiation is present in the case of technetium-99m, the scans can be performed without worrying about the potential effects of reactionary byproducts. Once these scans are complete and the technetium-99m gradually reaches the technetium-99 ground state, from the perspective of the patient, it effectively becomes dormant. The nucleus is definitely still experiencing decay as it transforms to the stable form of ruthenium-99 (again through negative beta decay);



however, this process has a half-life of 2.11×10^5 years (Table of nuclides, 2008). With the volume of technetium-99m that is being injected into each person, the patient will see a negligible amount of activity from the residual technetium-99 that is not excreted from the body.

Along with the minimization of harm to the patient, there are a few reasons why technetium-99m is such an attractive option as a radiopharmaceutical. The first of these deals with the radioisotope when it is in the form of molybdenum-99, before it even becomes technetium-99m. With a half-life of 65.94 hours (Table of nuclides, 2008), the transformation of molybdenum-99 to technetium-99m provides an important delay. Since hospitals and nuclear reactors are not usually located at the same site, the decay time of the molybdenum allows it to be transported from the reactor to the hospitals or clinics before it has reached a stable state. Recall, for a product to be useful as a radioisotope, it must still be decaying when it is injected into the patient. This is enhanced by the fact that

the half-life of the technetium-99m is only 6.01 hours (Table of nuclides, 2008). Although such a short half-life means that the technetium must be used almost immediately, it also has a useful aspect. In nuclear decay, for a given amount of time, a shorter half-life means more activity during that time. As such, less technetium-99m can be used than if there were a longer half-life while still achieving the same resolution from the gamma camera. For the patient this translates to less exposure, and for the hospital, more samples per batch of molybdenum-99.

Though an abbreviated description of the process that occurs once the radioisotope has reached the hospital may sound simply like “inject and examine the result,” the full cancer detection process that begins at the hospital is actually a complex union of biological, chemical, mechanical, and nuclear sciences. The molybdenum-99 arrives at the destination in a lead-enclosed glass tube designed to hold both the isotope and the radiation that is constantly produced during transportation. While the conversion to technetium-99m is a constantly occurring reaction inside the container, it is not needed as such. As it is given to patients in finite doses, the technetium cannot be gradually siphoned from the container and used as produced. Instead, it accumulates in the container and, when needed, the technetium-99m is chemically separated from the molybdenum-99 through the use of a saline solution (Zolle, 2007). Before it can be given to the patient, though, the technetium must first be combined chemically with a molecule through chelation. This process is where a central metal ion (technetium-99m) bonds to two or more atoms of a bi-ligand, also known as a chelator. The total compound is referred to as a tracer molecule. In the case of nuclear medicine, the chelator is a molecule which has a well-established ability to interact with a certain part of the body. For

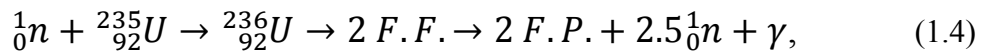
example, certain tin compounds are able to attach to red blood cells, allowing the technetium to flow through and highlight defects in the circulatory system. Similarly, technetium attached to calcium can be used to detect damage done specifically to the heart. Regardless of the intent, the technetium-99m requires a chelator in some form or another in order to function in the body.

Once the chelator and technetium are bonded, the tracer is finally ready to be administered to the patient. After the compound has been injected and reaches the tumor or desired area of the body, the patient is then examined with the aid of a gamma camera. In a rudimentary sense, a gamma camera is able to see high frequency electromagnetic radiation in much the same way that a normal digital camera senses the visible spectrum. The electromagnetic rays enter the camera, strike an electromagnetic-sensitive medium, and these hits collectively form an image. In a gamma camera, the EM-sensitive medium is typically an iodide crystal, which emits a localized flash of light when struck by gamma radiation. The emitted light is then detected and amplified by a photomultiplier tube and passed on to a computer for signal processing. The final image represents the density of the light detected by the photomultiplier tubes. In areas of the body with a higher mass density, such as near organs or tumors, the radiation is more frequently absorbed in the body, while areas of lower density will allow more of the radiation to escape and be detected by the camera. This difference provides the contrast from which an image is formed and used for diagnosis.

1.3 Thermal/Neutronics Background

Like any fission reaction, the transformation of uranium-235 into molybdenum-99 and other products generates a significant amount of heat. From the nuclear aspect, there is no way to avoid this heat, as it is a result of two inescapable sources: electromagnetic radiation and kinetic energy.

The chain reaction that describes the fission process is



where F.F. are the fission fragments and F.P. are the fission products. These two differ because the fission fragments are highly unstable nuclei while the fission products are longer lived, though still unstable, nuclei. The conversion from the fission fragments to the fission products occurs almost instantly after the initial split and is accompanied by a gamma ray and an average of 2.5 neutrons. Depending on the fission products, the actual number of neutrons released typically ranges between 0 and 5.

At the moment after fission, the fission fragments formed have a velocity of approximately 9×10^6 m/s (CANDU reactor, 2004), which accounts for a majority of the energy created in the fission. Through ionization and inelastic collisions, this energy is transferred to nearby atoms. Then, after the fission fragments break down, the neutrons produced have energies of around 2 MeV, much of which is kinetic. By colliding with other nuclei, these “fast” neutrons lose their energy to the surroundings, becoming “slow” or “thermal” neutrons.

Between the electromagnetic radiation and kinetic energy, far too much heat is generated in the fissioning materials to be safely dissipated without the aid of a continuous coolant. Commonly, normal or heavy water serve as the coolant, though a few reactors use carbon dioxide or even liquid metals. For the purposes of this research, the coolant is regular water.

The end goal of this research is to find the geometric configuration that will produce the maximum amount of molybdenum-99. As molybdenum-99 is one of the eventual products of uranium-235 fission, its production will be maximized when the most uranium undergoes fission. More fission reactions mean more heat, and since heat is the limiting factor of the production process, the real goal of this research is to calculate the maximum rate of heat transferrable away from the fission reaction.

In the end, each gram of uranium-235 that fissions completely releases 8.2×10^{10} J of energy (CANDU reactor, 2004). However, the uranium is irradiated in the reactor for just 1 week. With such a short irradiation period, only a small amount of the uranium-235 ($\approx 3\%$) will actually undergo fission. After taking into account many other factors specific to MURR, such as the fission cross-section and neutron flux, the heat generated from fission is calculated to be about 500 W per gram of uranium-235 initially placed in the reactor (Allen and Peters, 2008). For a 4-gram sample of uranium-235, (a number that will be explained in the next section,) the heat transfer rate becomes 2 kW.

1.4 Target Design

Up to this point, there has been no mention as to what the uranium looks like when it is placed in the reactor. Clearly, it cannot just be dumped into the reactor pool

after being enriched. Instead, a secondary structure must be designed to hold the uranium at the correct position with respect to the neutron flux source. Currently, the flat plate is the most commonly used target type for fuel elements, with the Petten target (bottom) in Fig. 1.1 being an example of this. It consists of a compound of UAl_x dispersed in a

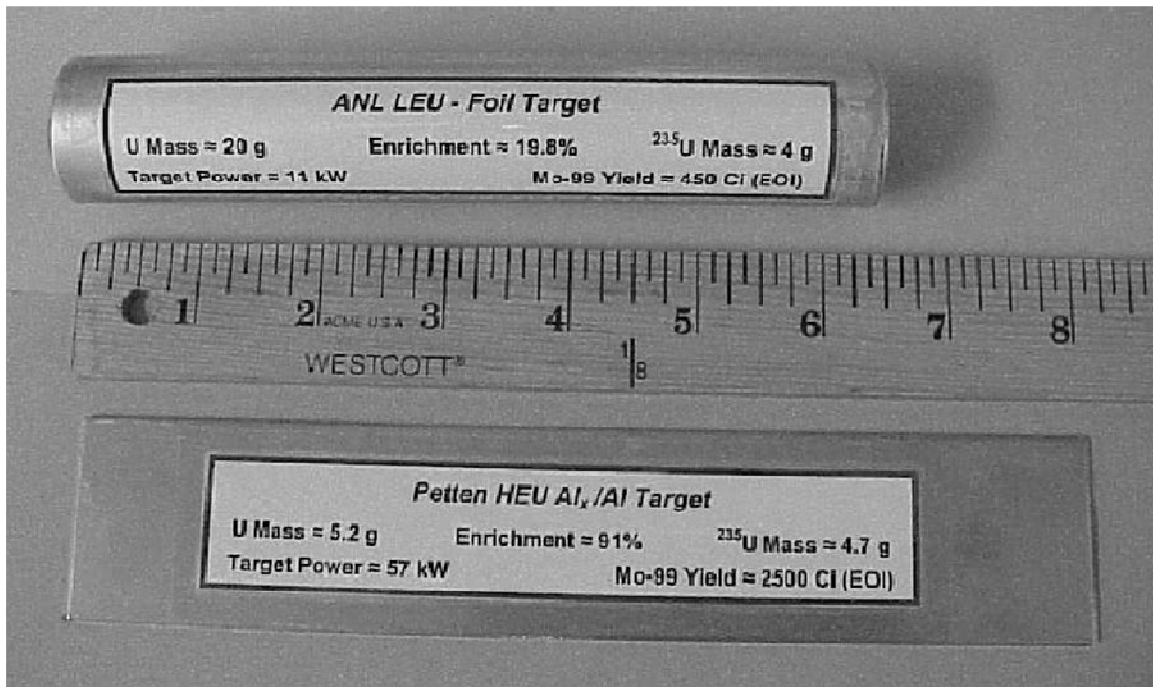


Figure 1.1 Two common target designs (Allen et al., 2007)

powdered aluminum matrix, which is then rolled into a plate (Vandegrift, Connor et al, 1997). The uranium/aluminum plate is then sandwiched between two non-fissioning cover plates, which are then welded together to result in the final target. It is easy to manufacture and easy to use; however, it is not perfect. These targets use high-enriched uranium (HEU). Currently, the four main reactors all use HEU as the parent material from which the technetium-99m is eventually created. Consisting of approximately 90% uranium-235, HEU can also be a primary component in nuclear weapons. As a result, there is pressure for these reactors to switch to the alternative of LEU, which consists of < 20% uranium-235.

While the switch away from HEU will increase safety, it is also the motivating factor behind the switch from the dispersion target to the foil target. Because LEU has only a fraction of the uranium-235 content that HEU has per unit weight, more LEU is required to achieve the same output of molybdenum-99. Therefore, if LEU were to be used in a dispersion target, the volume of the target would increase dramatically. But, by switching to a uranium foil and eliminating the aluminum that was used in the dispersion target, the mean uranium-235 density of the foil target is much higher than that of a comparable dispersion target. As a result, the amount of uranium-235 in and volume of an LEU foil target will approximately match the amount of uranium-235 in and volume of an HEU dispersion target. Specifically, the dispersion targets from Petten use 5.2 g uranium and an enrichment of 91% for a total of 4.7 g of uranium-235 (Allen et al., 2007). The foil targets designed by Argonne National Laboratory feature 20 g of LEU, enriched to 19.8% (Allen et al., 2007). This means that the foil target contains about 4 g uranium-235, which is about 14.9% less than the 4.7 g present in the dispersion targets.

The switch in target shape away from flat plate is also a result of the switch from HEU to LEU. In the HEU dispersion plate targets, the UAl_x plate effectively fuses to the cover plates during fission, resulting in one solid mass. In the LEU foil targets, a thin nickel layer located between the LEU and the cover plates prevents their fusing. This is done so that the products can be easily removed after fission. The downside of this is that for a flat plate foil target, there is the possibility that as the uranium begins to fission and the temperature begins to increase, the target walls will expand. At some point, the walls will eventually force themselves away from contact with the uranium, an effect called “pillowing.” Leaving a gap between the uranium and the outer walls of the target, the

heat would then be transferred to the walls by radiation, as compared to conduction. Since radiation is ineffective except at extreme temperatures, the heat would build up inside the target, potentially melting the uranium. To ensure pillowing cannot happen, an annular cylinder foil target has been proposed. A sample of this geometry is demonstrated in ANL target (top) in Fig. 1.1. In this geometry the uranium is rolled into a foil and then sandwiched between two concentric, circular aluminum tubes. In this way, the thermal stresses that develop in the target walls would develop into a hoop stress that would hold the target together.

Although the flat plate and the annular cylinder targets are currently the most popular, they are not the only designs that were used. Up until at least 1997, the Australian Nuclear Science and Technology Organization used low-enriched pellets of UO_2 in their reactor (Snelgrove et al., 1997). In Southeast Asia around the same time, the National Atomic Energy Agency (BATAN) of Indonesia was using a different type of HEU target. An early inspiration for the annular target being looked at today, BATAN used a stainless steel tube with a thin coating of UO_2 on the inner wall, called the Cintichem target. This method had already been abandoned by the United States in the late 1980s, when it was shown that the switch to LEU was not possible while maintaining the method that was used to produce these HEU targets (Snelgrove et al., 1997). Then, in the late 1990s and early 2000s, the Argentine National Atomic Energy Commission began using “miniplates.” They contained 1.1 g of HEU (Vandegrift, Koma et al., 2000) and were enriched to above 90%, meaning about 1.0 g of uranium-235.

1.5 Current Reactor Setup

While a fully functioning technetium-99m mass production process is still years away, the first steps toward this goal have already been taken close to home. At the

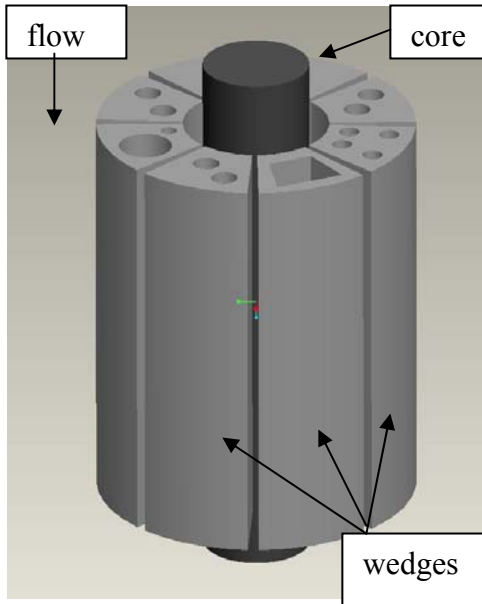


Figure 1.2 Sketch of reactor core surrounded by wedges.

University of Missouri Research Reactor (MURR), active fission trials are already being run utilizing the current reactor geometry. In the present setup, the core of the reactor is surrounded by separate wedges, as demonstrated in Fig. 1.2. Although all of the wedges have some sort of water flow through them, they each serve a different purpose. As a result, there is one wedge that lends itself to study, and it is the wedge that is used in the current molybdenum-99 production

tests. This wedge is characterized by two holes that run lengthwise through the wedge and then arrive at a shared exit drain just before the bottom. One of the holes is significantly larger than the other, with the larger being dubbed the “N-6 channel” and the smaller the “N-1 channel.” Figure 1.3 pictorially outlines the features of this wedge. During operation, the N-6 channel is plugged up, allowing water only to pass through the N-1 channel for this particular wedge. The annular cylinder target is then placed in the center of the N-1 channel and held there for the duration of the irradiation period.

The reason behind covering the uranium foil with aluminum brings up an important topic of discussion: reactor safety regulations. In the context of this analysis, there are three regulations that are worth mentioning. The first of these requires that none

of the uranium or fission products may come in direct contact with the cooling water that flows through the channels, a condition sufficiently fulfilled by the concentric aluminum cylinders that seal in the uranium foil. The aluminum also serves the dual purpose of providing structural stability to the extremely thin uranium foil, though the research in this thesis is not concerned with this aspect. Secondly, no material may exceed half the melting temperature of the material with the lowest melting point. In this case, the limiting material is the aluminum surrounding the uranium foil. Being made from Al-3003, this cladding has a melting temperature of approximately 650 °C, meaning that no temperature in the target (or anywhere else) may surpass 325 °C. The final safety regulation deals with the cooling water that flows through all of the wedges. Initially at a temperature of approximately 50 °C, the water must always remain a liquid.

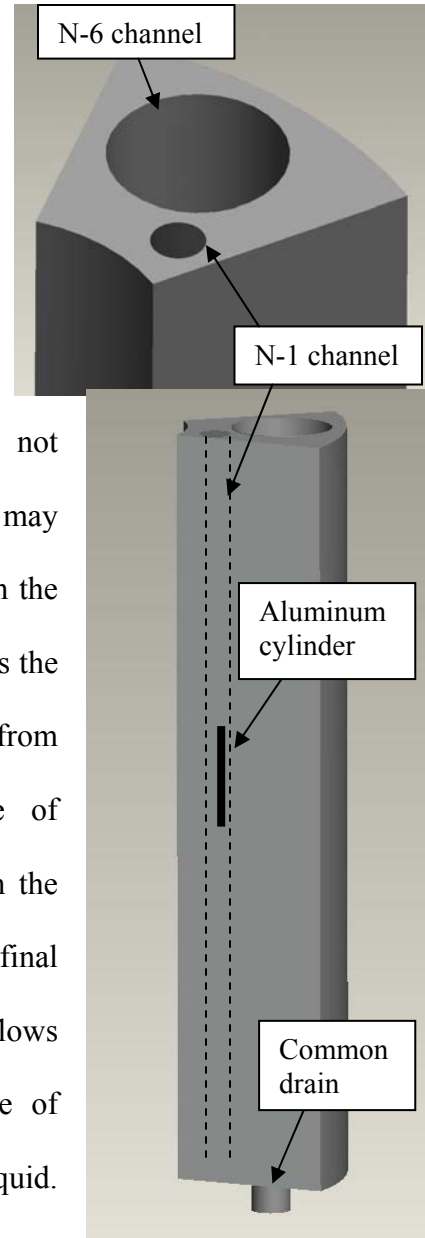


Figure 1.3 Sketch of wedge currently used for testing

While this restriction prevents a large amount of heat transfer that could be taken advantage of during the phase change process, it does allow the heat transfer model to be greatly simplified. Without any vapor formation, the water can simply be modeled as a single-phase heat exchanger, something that will be discussed in greater detail in Chapter 5.

Keeping these constraints in mind, this thesis will describe a process to maximize the total amount of heat that can be dissipated within a single wedge in order to maximize the production of molybdenum-99. The current configuration of a single wedge can be seen in Fig. 1.3. For the optimization process, only the outer geometry of the wedge must remain the same. All other wedge features will be modified. The analysis will use numeric and analytic models calibrated by a previous experiment.

Chapter 2

OBJECTIVES

2.1 Past Research

From neutronics to emergency cooling systems, there has been no shortage of research being done on nuclear reactors since their creation. Much effort has gone into proving that a necessary neutron flux is possible, or towards showing a certain coolant flow can keep the reactor core from overheating, or even producing evidence that the neutron-hardening in the walls is negligible for some number of years. And in order to design a safe and reliable reactor or to keep an already operating reactor running smoothly, portions of this research have been heavily relied upon.

This is also true for the narrow focus of molybdenum-99 production. In the past, dozens of papers have been written on different aspects of this project. Some have dealt with safety features related to the neutron flux (Meftah, Zidi and Bousbia-Salah, 2006, Meftah, Zidi, Zergoug, et al., 2006), while others have focused on overheating issues. The High Flux Australian Reactor (HIFAR) in particular has been the subject of many thermal-based papers (Hari et al., 1999; Tu, 1997; Connolly and Clancy, 1993). A few papers even cover topics similar to those discussed in this report, such as the design of the target (Yeoh and Wassink, 2003) and thermal/hydraulic analyses around the target (Mushtaq et al., 2008).

The reason these papers, and many others on the same topic, differ from the research presented here is because they rely heavily on numeric simulations. While they can solve flow and temperature fields for complex geometries, the drawback of using numeric simulations is that a new drawing and mesh must be created for each new geometry explored. Such a time-intensive process makes numeric tools relatively poor choices for spatial design optimization. Therefore, an analytic model is developed to facilitate design optimization.

A relatively new technique that can be used to simplify the thermal/hydraulic analysis is flow network modeling (FNM). It has been used in the electronics field with some success, but it isn't clear that it has been applied to evaluating flows in irradiation positions of research reactors. In the late 1990s, FNM was developed to effectively model fluid dynamics and heat transfer in cold plates and heat sinks (Yeh et al., 2000, Radmehr et al., 1999, Radmehr and Patankar 2004), cooling manifolds (Verma, 2002), burn-in ovens (Dishong et al., 2000), and electronic enclosures (Kowalski and Radmehr, 2000; Minichiello and May, 2000; Minichiello and Belady, 2002). It has been implemented in these fields and many others largely because of its adaptability, as well as the increasing complexity of those systems. For example, computer and server cases are constantly being designed smaller and smaller with an increasing number of parts, such that the flow for the entire system is noticeably affected by the addition or subtraction of a single component. FNM is utilized in these situations by treating the flow path like that of an electrical circuit. Each location that the flow experiences a pressure drop is represented as an electrical resistor. In this way, the resistances can then be combined in series and parallel to determine the relative effects of the components relative to the entire system.

This methodology works well for the irradiation positions in MURR because, in order to optimize the parallel channels for the maximum possible molybdenum-99 production, and therefore the rate of heat transfer, the close-packed nature of the channels means that the addition or removal of a channel will likely have a noticeable effect on the heat transfer in the other channels. Additionally, FNM can be used to determine if the common drain is restricting the overall flow and to what degree. With FNM, any number of hypothetical situations about the geometry can also be played out by adding in an analytic term for each feature that is being examined, provided that expressions for resistors can be developed for fluid (momentum) and thermal (energy) transport.

2.2 Goals

Within the context of this thesis, there are four primary goals:

- Develop a hydraulic model which uses driving pressure to obtain pressure drops and average velocities for a single channel
- Develop a thermal model that uses the hydraulic model to calculate the heat transfer from a single target in a flow channel
- Modify the hydraulic and thermal models to evaluate multiple targets in multiple channels
- Maximize heat transfer from a single wedge with multiple targets/channels

The process by which these goals are accomplished is displayed at the end of the chapter as a flow chart in Fig. 2.1.

2.2.1 Hydraulic Model for a Single Channel

The coolant flow velocity depends on the geometry of the target in the flow channel and the driving pressure in the reactor pool, labeled in Fig. 2.2. Geometric modeling is relatively straightforward; however, the effective driving pressure in the pool is unknown. This can be found by conducting a flow velocity experiment

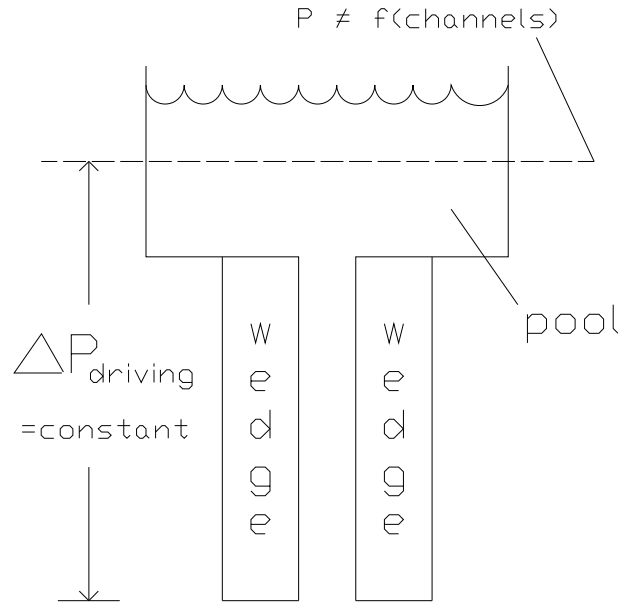


Figure 2.2 Sketch of reactor pool and flow channel of interest.

A numeric simulation of the velocity probe in the flow allows the effective driving pressure to be found. Knowing the driving pressure at a location that is not significantly impacted by geometry modifications, the flow velocity and component pressure drops are evaluated numerically. The numeric models are then used to “calibrate” analytic model constants.

2.2.2 Thermal Model for a Single Channel

The heat transfer from a single target is a function of the hydrodynamic properties already obtained, in conjunction with experimental correlations for the Nusselt number. Geometry allows the analytic model to be derived and treated as a single phase heat

exchanger. The numeric models with a single target are then utilized to confirm the proper Nusselt correlation is used in the analytic model.

2.2.3 Evaluation of Multiple Channels

Expanding the hydraulic and thermal models to accommodate targets in parallel channels requires representing each of the models in the likeness of an electrical system, with a driving force, a flow, and a resistance. The driving forces and flows are straightforward, as they both have direct counterparts. The resistors are defined in terms of loss coefficients and friction factors for the hydraulic model and heat exchanger theory for the thermal model. A numeric model checks to ensure the coefficients for the single channel models are still valid with multiple channels.

2.2.4 Maximizing Heat Transfer

By altering the channel diameter, drain diameter, and number of channels with a brute-force iterative approach, the multiple channel thermal/hydraulic model is able to find the resulting heat transfer rate, from which the maximum value is extrapolated. A thermal/hydraulic entropy generation model is also derived, and the resulting curves are compared to those of the heat transfer against the same variables to determine the compatibility of the two models.

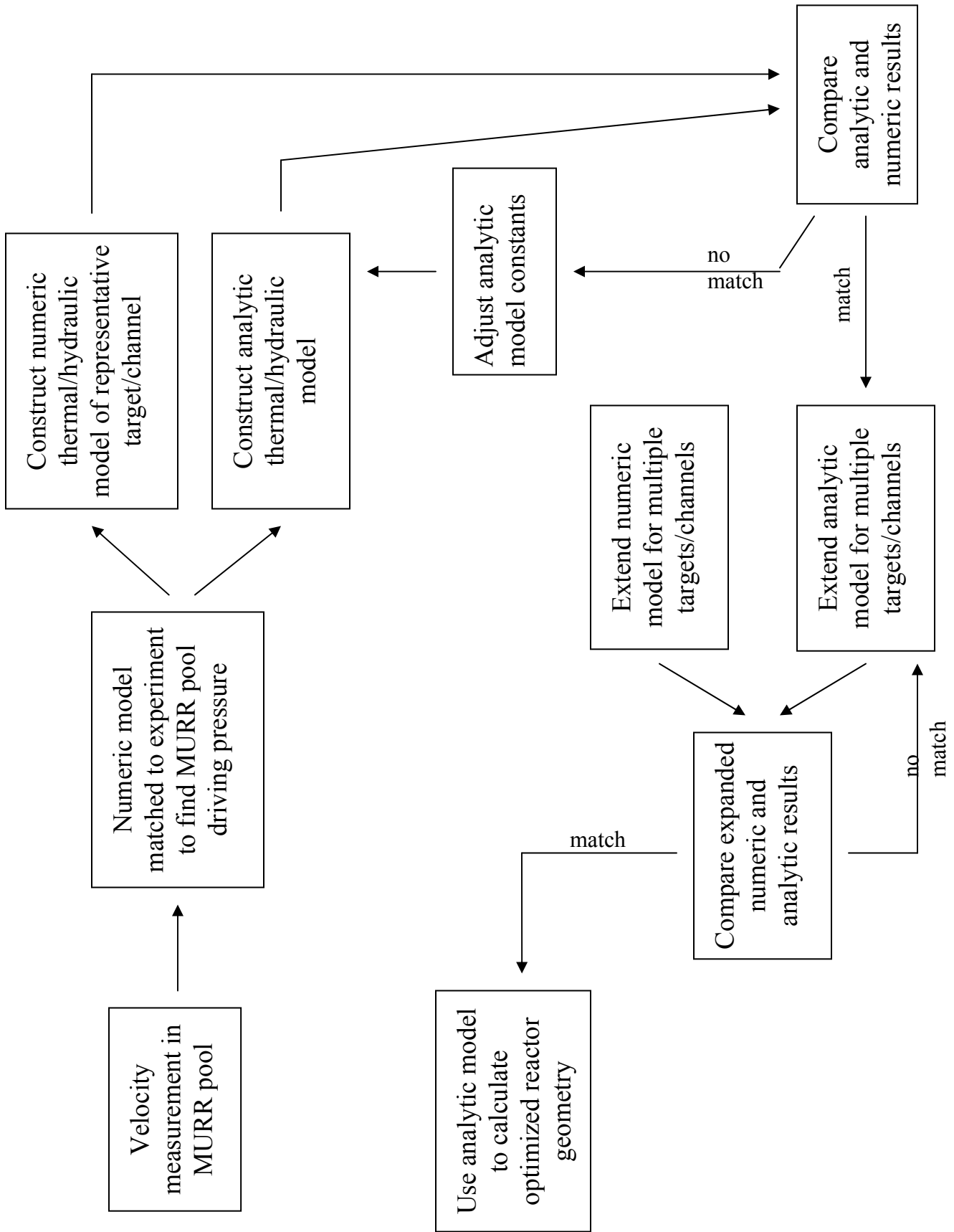


Fig. 2.1 Flow chart of the steps that led to the final model.

Chapter 3 BOUNDARY CONDITIONS

3.1 Hydrodynamic Model - Boundary Conditions

In the reactor, there is a single pump that circulates the flow of the entire pool, as seen in Fig. 3.1. Unfortunately, modeling the full loop is nearly impossible due to the number of features and complexities contained within. As a result, a consolidated model is created. In short, the model essentially consists of the wedge shown in Fig. 1.3 with an imaginary reservoir above. The purpose of the reservoir is to characterize the top of the reactor pool without requiring all pool attributes to be modeled.

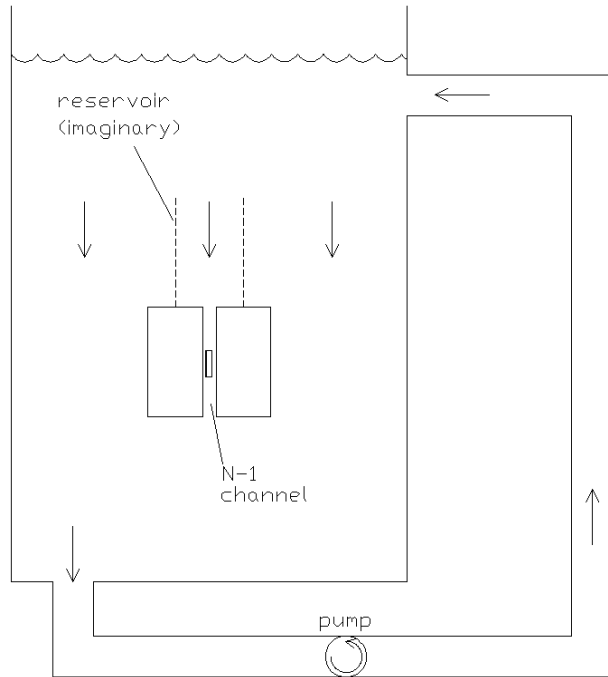


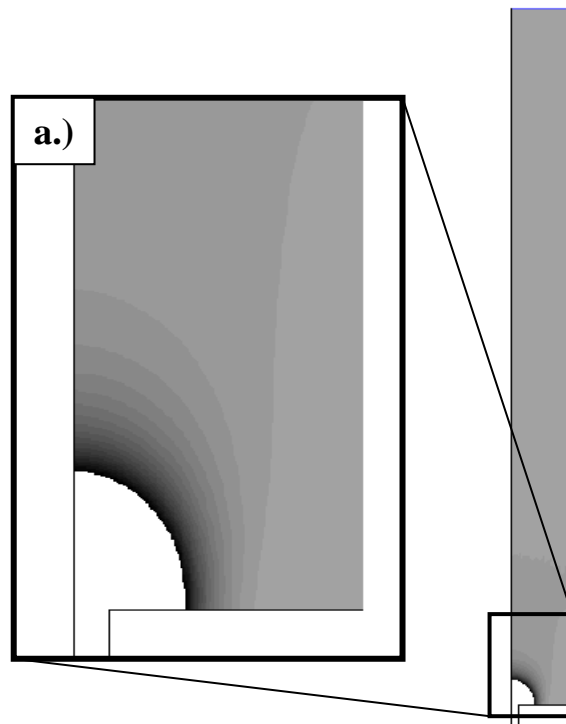
Figure 2.1 Diagram of the reactor flow loop.

The minimum size of the reservoir is quickly determined simply by creating a numeric model of a channel with an oversized reservoir and by running a simulation. The boundary conditions and assumptions of the simulation are listed in Table. 3.1. Figure 3.2 shows a pressure distribution in the reservoir for a pressure drop of 8430 Pa from the top

Table 3.1 Simulation parameters for determining minimum reservoir size.

Property	Notes
Assumptions	Minimum reservoir size is approximately constant regardless of channel geometry. This simulation used an empty channel.
Boundary conditions	8430 Pa total pressure drop
Turbulence	k-ε (k-epsilon) model
Mesh	Map (rectangular) mesh with a high-density tri (triangular) mesh around the sudden contraction, ≈ 50k cells total

of the reservoir to below the N-1 channel. Figure 3.2a demonstrates this through the use of a contour plot in FLUENT, where the range of static pressures displayed was between 8420 Pa and 8430 Pa (0.1-0.0% inlet pressure drop, i.e. no change from inlet pressure). The lighter grays represent higher pressure, with the exception of the white region, which represents an area where the pressure is below 8420 Pa. Figure 3.2b shows the centerline distribution of pressure ranging from the top of the reservoir to the junction with the N-1 channel. These plots clearly demonstrate that there is no appreciable change in the inlet pressure until about 20 centimeters above the N-1 channel. Subsequent single channel simulations were run with the reservoir 50 centimeters above the channel.



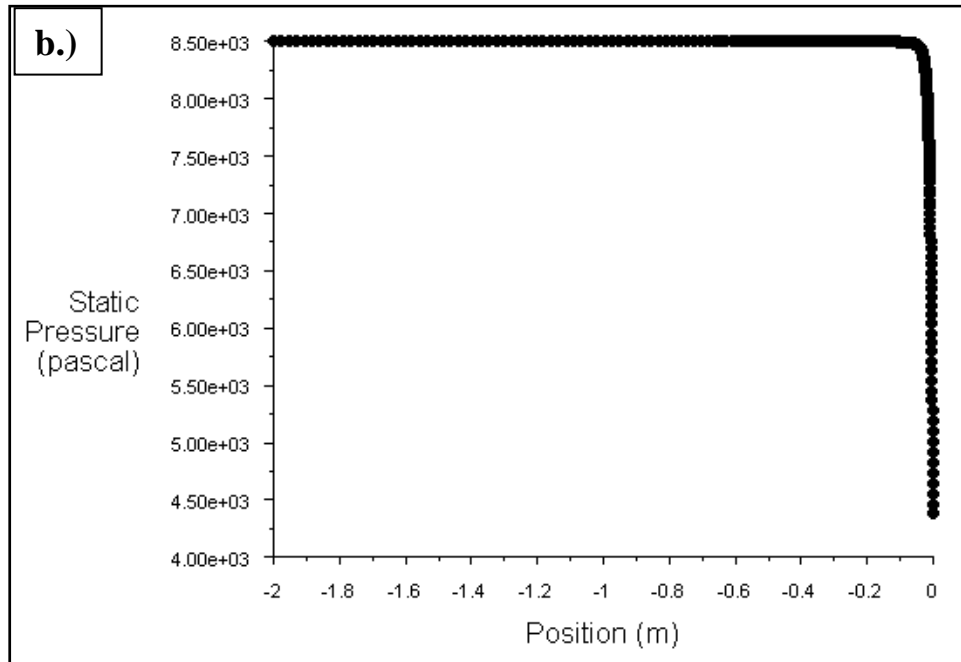


Figure 3.2 Pressure distribution in the reservoir in a.) a contour form b.) a centerline plot

To solve for the flow field in the reduced model, two hydrodynamic boundary conditions are required. FLUENT allows an inlet/outlet pressure boundary condition or a mass flow/outlet pressure boundary condition. However, since the pump drives the flow through many different channels, the mass flow rate is not fixed for the channel being examined and the latter option cannot be used. Because it is the relative difference in pressure that causes a net flow in the system, the pressures can be lumped into a single pressure, defined as

$$P_{\text{driving}} \equiv P_{\text{inlet}} - P_{\text{outlet}} \quad (3.1)$$

as long as the total pressure at the bottom of the model is constantly held to be zero. In order to calculate this driving pressure, some data must first be known about the reactor pool.

A hot wire anemometer was used to take velocity measurements in the reactor pool (Bruun, 1995). Before it was placed in the N-1 channel, the anemometer probe was attached to two interconnected cylinders that provided support and kept the probe aligned with the irradiation channel. A picture of the probe and holder is displayed in Fig. 3.3. After being calibrated inside a controlled laboratory flow loop, the entire configuration was then lowered into and held inside the flow channel in the reactor pool. The measured water velocity inside the N-1 channel at the probe was determined to be 3.4 ± 0.8 m/s (Solbrekken et

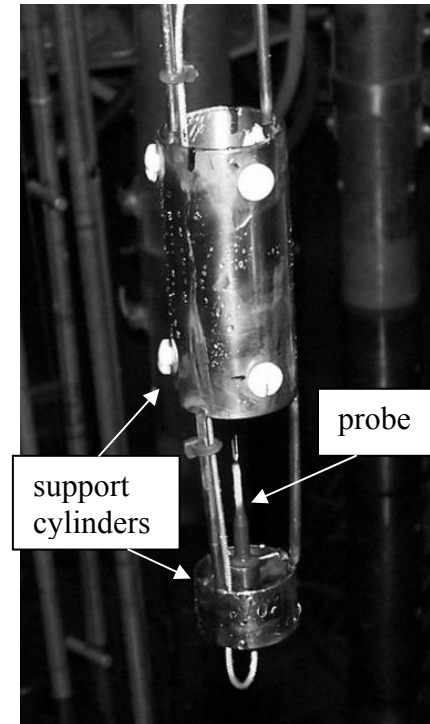


Figure 3.3 Picture of anemometer probe assembly

al., 2008). While this data is specific to MURR, the process described throughout this thesis can be applied to other reactors.

Setting the outlet pressure to be zero and with guesses for values of the driving pressure, numeric simulations of the model are run to find the driving pressure required to achieve a channel velocity at the location of the anemometer. This location is pinpointed in Fig. 3.4. The actual head of the anemometer is not modeled numerically because it has a diameter of $50 \mu\text{m}$. Being only microns thick, the wire, which actually measures the velocity, is figured not to have any real effect on the flow. It is, however,

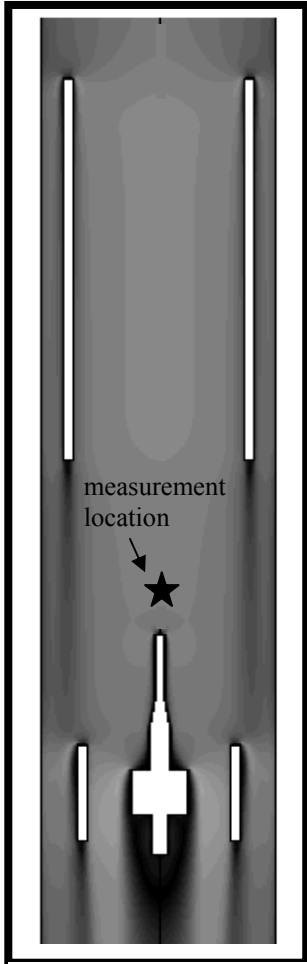


Figure 3.4 Location of velocity measurement on anemometer

known to be located 7.5 mm ahead of the foremost modeled part of the probe and is labeled as the point of velocity measurement. After enough simulations are performed, the single data point taken from each simulation is plotted against the driving pressure to form a smooth curve, as displayed in Fig. 3.5. By interpolating this curve, the true boundary condition that is required for the anemometer probe to measure 3.4 m/s is found to be approximately 8430 Pa. Similarly, 2.6 m/s ($3.4 - 0.8$) corresponds to 4940 Pa, and 4.2 m/s ($3.4 + 0.8$) corresponds to 12,840 Pa.

As the anemometer probe takes up some of the cross-sectional flow area, the flow is slightly choked as it tries to pass around the probe. Therefore, while the anemometer measures a velocity of 3.4 ± 0.8 m/s in the N-1 channel, when it is removed from that channel, the flow rate in that same channel is

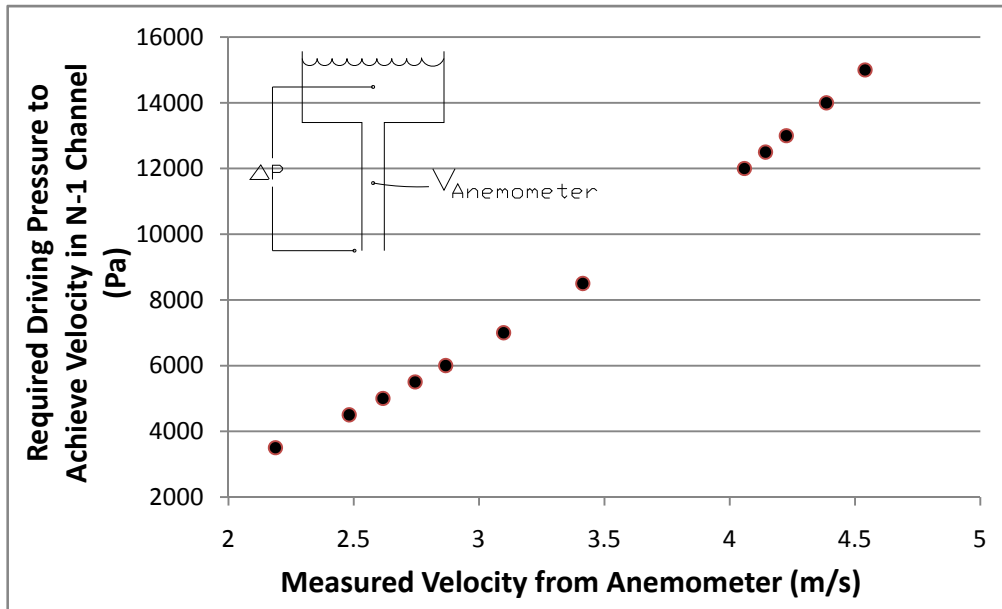


Figure 3.5 Driving pressure vs. measured velocity at anemometer

expected to increase. Numeric simulations are performed to determine the exact effect of the probe, though a few different geometries are required to complete this task. Already discussed, the first case is the N-1 channel, which contains the anemometer probe. The second case uses an empty N-1 channel. The last case looks toward the direction of the final goal, determining the maximum heat transfer from a wedge, by describing a channel containing an annular cylinder target. A sketch of each of the geometries is presented in Fig. 3.6 in a 2-D axisymmetric representation. To obtain the 3-D model from the picture, simply rotate each of the models about their axis of rotation (dashed line).

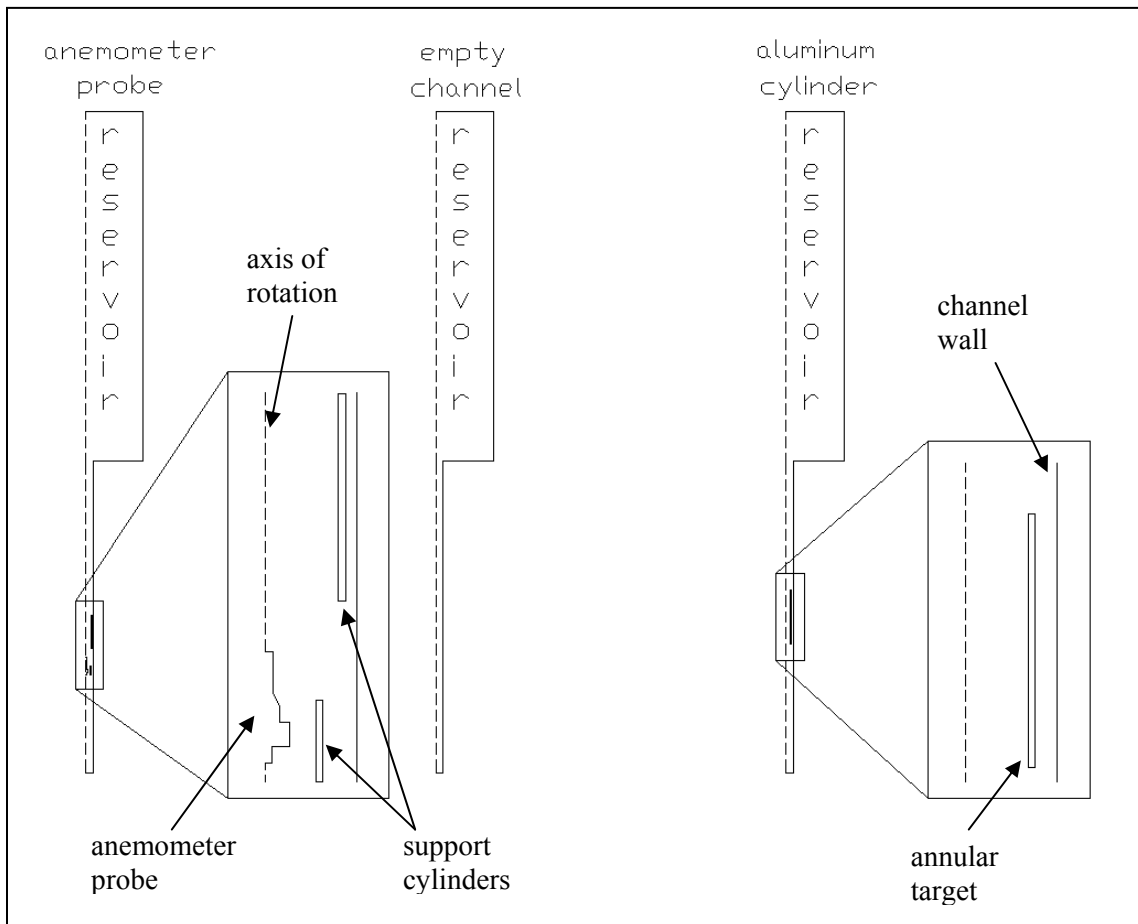


Figure 3.6 The three 2-D geometries examined in FLUENT

Since the driving pressure calculated above is for the anemometer model, this information does very little unless a relationship can be established between that model and the other two models displayed in Fig. 3.6. Fortunately, this relationship can be approximated in the boundary conditions. As stated before, the total pressure at the outlet was defined to be 0 Pa so that the pressure at the inlet became the driving pressure across the model. As long as the reservoir of the model is made large enough, the driving pressure remains fairly constant between the three geometries in Fig. 3.6. The reasoning for this is simply because the N-1 channel is only a small part of the reactor pool. Therefore, even large geometry changes inside the N-1 channel will still have only a small impact on the rest of the overall reactor flow. Along the same lines, if the reservoir approximates the top of the reactor pool and is adequately large, the geometry inside the N-1 channel will not have an effect far upstream. Consequently, the driving pressure will be the same for each of the models.

After the boundary conditions for the other two models are established, 2-dimensional axisymmetric simulations of those models are run. Three trials are conducted for each case. These three trials correspond to the average velocity value and limits of 3.4 ± 0.8 m/s set up by the experimental anemometer probe. From Fig. 3.5, this velocity corresponds to a static pressure of 8430 Pa, with lower and upper range limits of 4940 and 12840 Pa, respectively. The three trials to be run for each model use these pressures as the inlet boundary conditions (driving pressures). All trials still use an outlet boundary condition of 0 Pa. Fig. 3.7 displays the mass flow rates plotted against the boundary conditions for the empty channel and the channel with the annular cylinder target, as well as for the already completed simulations with the anemometer probe. As suspected, the

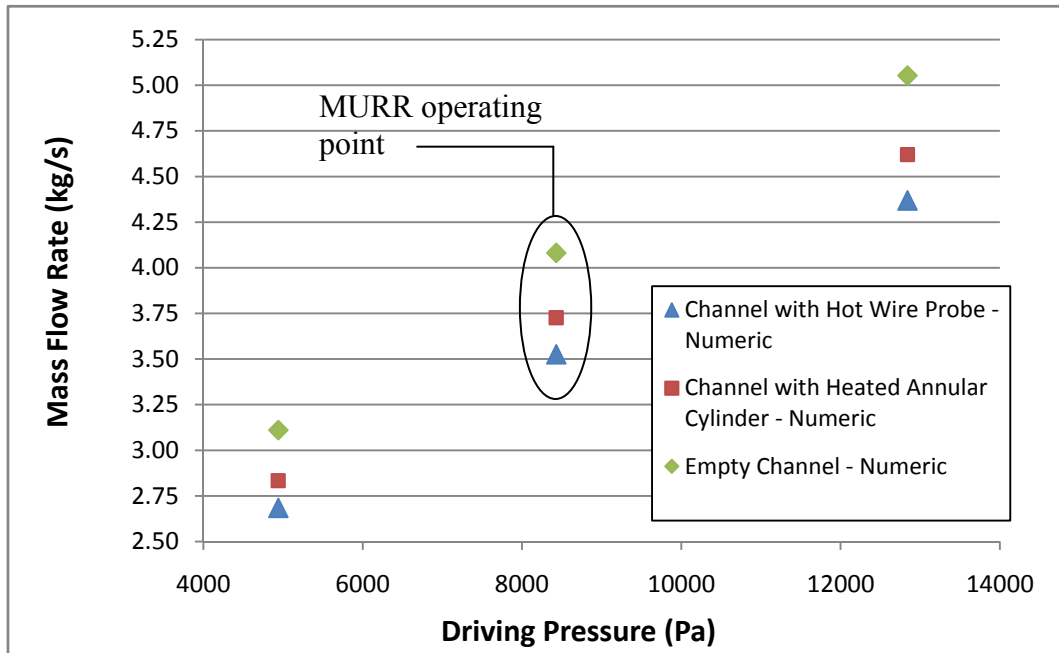


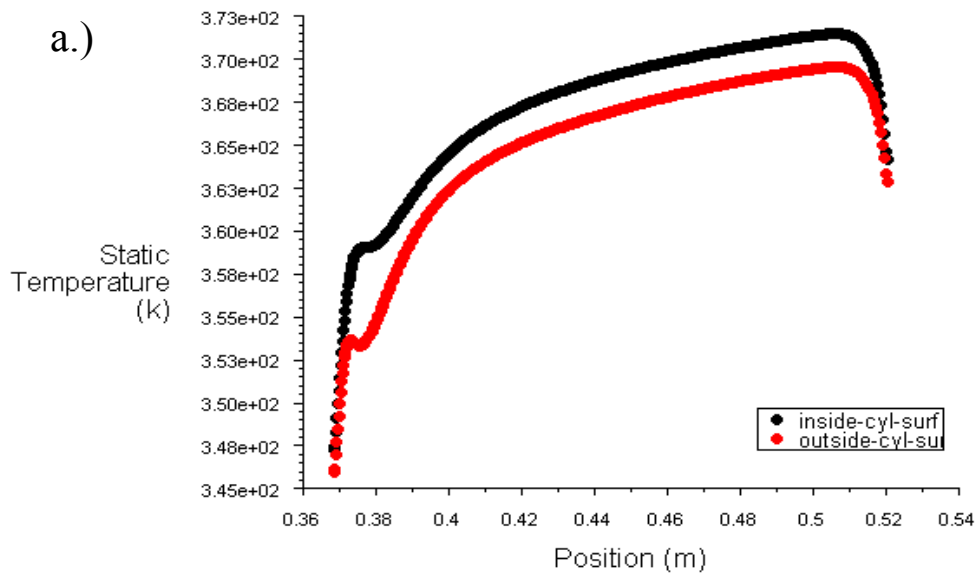
Figure 3.7 Mass flow rate vs. driving pressure across the N-1 channel for 3 cases

geometry affects the in-channel mass flow to a degree that cannot be ignored. As the anemometer probe takes up the most cross-sectional area, the resulting mass flow rate through the system is the least of the three models. Similarly, the empty channel has no constrictions in the channel, which is why it has the highest mass flow rate. These results will later be compared to the results from the analytic hydraulic model.

3.2 Thermal Model - Boundary Conditions

As stated in Chapter 1, safety regulations permit none of the cooling water to boil. The aim of this project is to establish a hard limit for the maximum heat transfer rate from the wedge. This is achieved by keeping the target walls that make direct contact with the water at a constant temperature of 373 K, the boiling temperature of water at atmospheric pressure.

The alternate to a constant wall temperature in the target is a constant heat flux at the uranium foil. The constant heat flux is a more realistic representation of the heat as it is generated and dispersed, but the constant temperature boundary condition provides an absolute upper limit for the heat transfer from the target. To show this, a numeric simulation is run for both cases. In the case of the constant heat flux boundary condition, different heat fluxes are tried for the foil until the highest surface temperature reaches 373 K, shown in Fig. 3.8a. The corresponding heat flux seen at the coolant-target interface is displayed in Fig. 3.8b. The higher heat flux and temperature at the inner surface is not



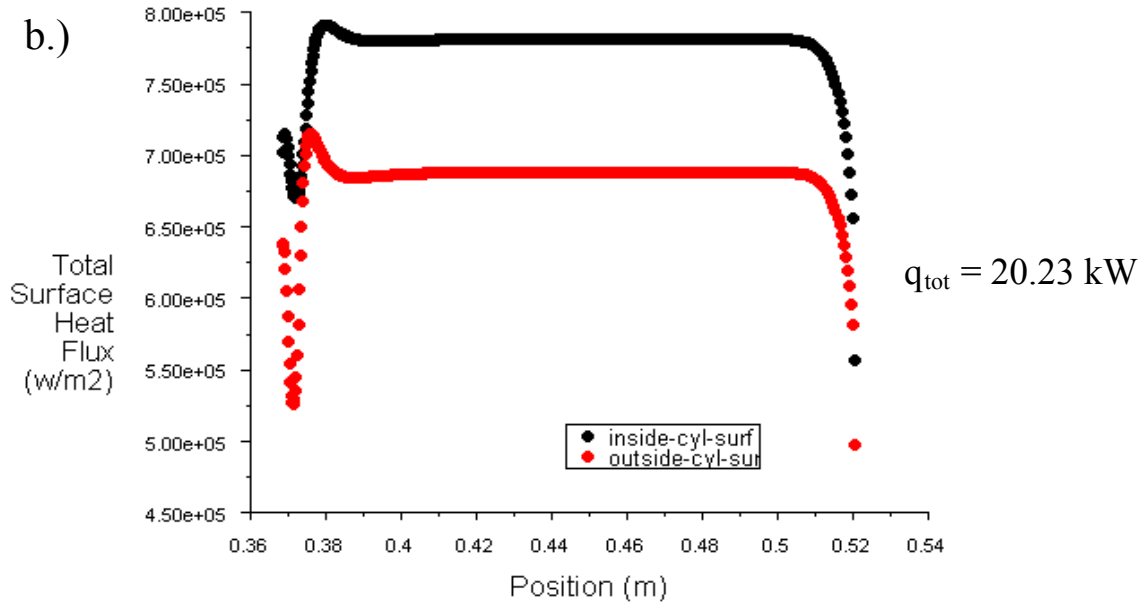
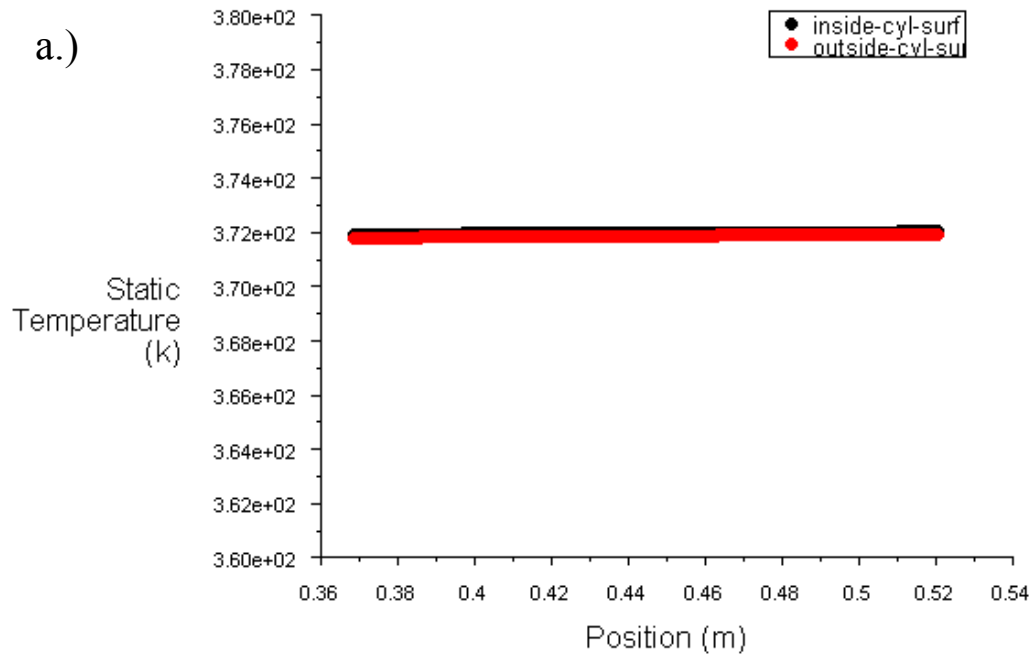


Figure 3.8 Thermal properties of a target for a constant heat flux at the LEU foil. a.) Temperature at the surface. b.) Heat flux at the surface.

surprising, as there is less area at the inner surface there. The second simulation is performed with a constant target wall temperature of 373 K. The temperature and heat flux at the surface of the target/coolant interface are shown in Fig. 3.9.



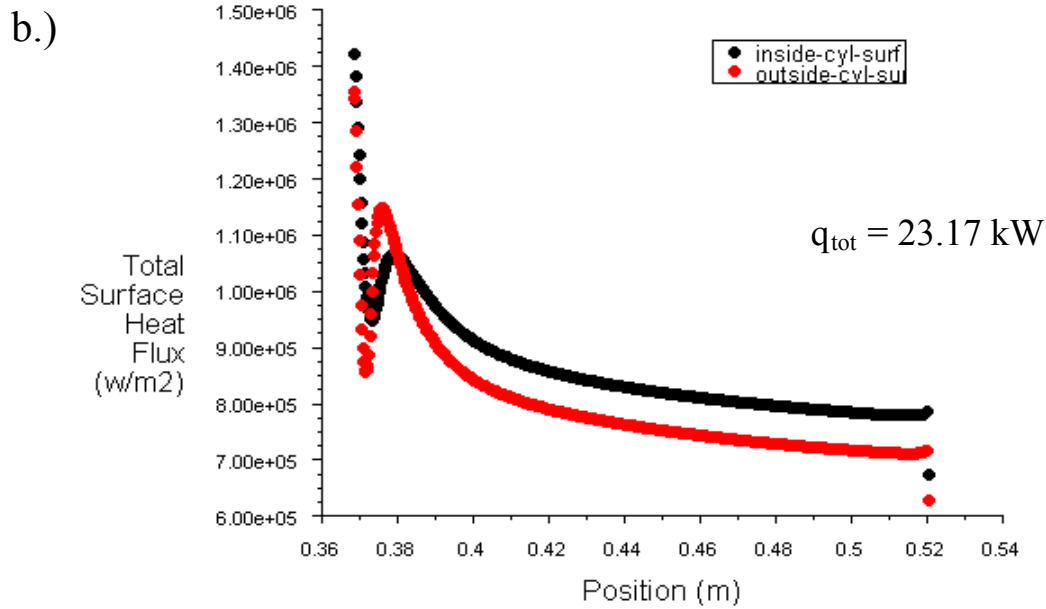


Figure 3.9 Thermal properties of a target for a constant wall temperature. a.) Temperature at the surface. b.) Heat flux from the surface.

The surface temperature in Fig. 3.8a is less than that in Fig. 3.9a at all locations except for one. As the temperature difference between the surface of the target and the water is the driving potential for heat transfer, it is expected that the heat flux is higher for the constant surface temperature case than for the constant heat flux case. This is confirmed when Fig. 3.8b is compared against Fig. 3.9b. The heat fluxes match only at the point where the surface temperatures are equal. Otherwise, the values in Fig. 3.9b are greater for all points. From these heat fluxes, the total rates of heat transfer are calculated in FLUENT, and the resulting values are 23.17 kW for constant surface temperature and 20.23 kW for constant heat flux.

In the reactor pool, where the target is under almost 10 meters of water, the saturated temperature of water is about 13 K higher than 373 K, but the difference is taken to be a factor of safety. Still, for thoroughness, the effect of the upper temperature limit on heat transfer is discussed in a comparative study in Chapter 7.

Chapter 4

HYDRODYNAMICS - RESISTANCE NETWORK

4.1 Background

In a single channel model with a fixed geometry, the 2-D axisymmetric solver in FLUENT did an excellent job obtaining the flow and thermal fields. If more than one channel is incorporated into the model, a 3-D model must be created, but FLUENT can still solve it quite effectively. However, if the geometry begins to change, using FLUENT becomes very labor intensive. Every time the geometry is changed, even if it is only a tiny change, a new geometry and mesh have to be recreated. And since each parameter varied requires at least three models to provide a trend, to effectively optimize a geometry numerically would take dozens of models and hundreds of hours. Instead, a different approach must be used. An analytic modeling approach based on Flow Network Modeling (FNM) allows geometry modification to be easily evaluated and will be developed here. Numeric simulations are used to “calibrate” the analytic model at various design points. FNM is a computation framework that is oriented toward evaluating the thermal/hydraulic performance of an array of flow channels. The pressure/flow and heat flux/temperature relations are converted into resistance elements. The resistance network is then solved similar to an electric circuit.

4.2 Hydraulic Model for a Single Channel

For an incompressible flow in one dimension applied to the 2 points identified in Fig. 4.1, Bernoulli's principle states

$$\left(\frac{P}{\rho g} + \frac{\delta}{2g} V^2 + z\right)_1 = \left(\frac{P}{\rho g} + \frac{\delta}{2g} V^2 + z\right)_2 + \Delta P_{pump} + \zeta_{friction} + \Sigma \zeta_{minor}. \quad (4.1)$$

where ζ denotes losses. For turbulent flow, the kinetic energy correction factor, δ , is very close to unity and can be approximated as such without any real loss of accuracy. Equation (4.1) is then rearranged to form

$$P_1 - P_2 = \frac{\rho}{2} (V_2^2 - V_1^2) + \rho g (z_2 - z_1) + \zeta_{friction} + \zeta_{minor}. \quad (4.2)$$

Since the pump provides the flow with the energy to overcome the height change that brings it to the top of the pool, as well as any losses that occur in the loop, the pressure that it must put into the flow is

$$\Delta P_{pump} = \rho g \Delta z + \zeta_{friction} + \zeta_{minor}. \quad (4.3)$$

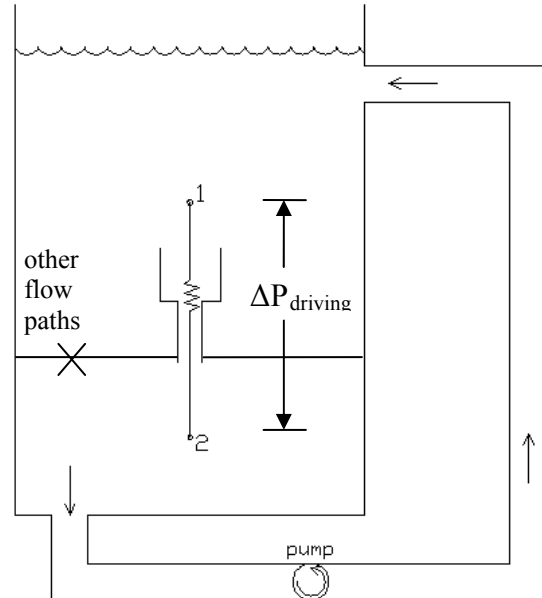


Figure 4.1 Simplified reactor flow loop

However, because the coolant flow forms a closed loop, the pump regulates the flow, as compared to gravity. Therefore, potential energy terms based off gravity can be ignored.

To demonstrate this with a specific case, a 2-D numeric model of Fig. 4.1 is created and then tested in FLUENT. Two cases are run, one with gravity and one without. Other than this difference, the two simulations are identical. Both use an inlet pressure of 20 kPa, arbitrarily chosen, and an outlet pressure of 0 kPa. The resulting static pressure distributions for the cases are identical and are depicted in Fig. 4.2. Also, the mass flow rates for both cases are found in FLUENT to be 2331 kg/s, confirming that gravity can be ignored.

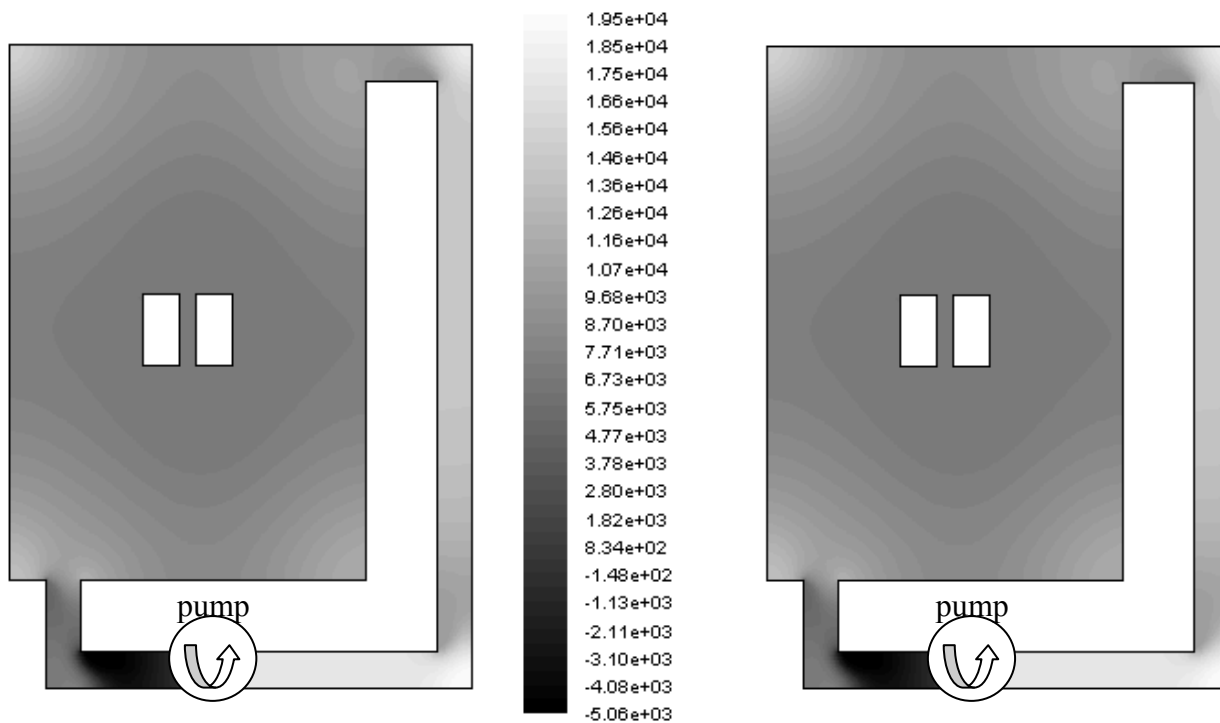


Figure 4.2 Comparison of pressure in FLUENT simulations with and without gravity.

Total pressure is a relative measure of energy in a fluid and is defined as the sum of the static, dynamic, and hydrostatic pressures:

$$P_t \equiv P_s + P_d + P_{hydro} = P_s + \frac{\rho V^2}{2} + \rho g z. \quad (4.4)$$

Through this identity, Eq. (4.2) can be reduced to

$$P_{t,1} - P_{t,2} = \Delta P_t = \zeta_{friction} + \zeta_{minor} = f(\dot{m}) \quad (4.5)$$

The pressure drop for frictional losses in a straight tube is

$$\Delta P_{friction} = f \frac{L}{D} \frac{\rho V^2}{2} \quad (4.6)$$

where f is the friction factor. Before a friction factor correlation, the Reynolds number,

$$Re \equiv \frac{VD}{\nu}. \quad (4.7)$$

is approximated to determine turbulence. Since the kinematic viscosity is $\mathcal{O}(1 \times 10^{-6} \text{ m}^2/\text{s})$ for water, diameters are $\mathcal{O}(0.01 \text{ m})$, and velocities are $\mathcal{O}(1 \text{ m/s})$, the Reynolds number is $\mathcal{O}(1 \times 10^4)$. Being greater than 4000, the flows are fully turbulent for all but the extreme values of diameters and velocities being examined. Therefore, to identify if the flow is fully developed, the appropriate entrance length ratio correlation is chosen as (White, 2003)

$$\frac{L_e}{D} \approx 4.4Re_d^{1/6}. \quad (4.8)$$

Even under conservative values for the Reynolds number and cross-sectional diameter, the approximated entrance length is still longer than the channel length, making the flow developing everywhere. As developing flow friction factors could not be found, developed flow ones were used instead. They are dependent on the Reynolds number according to the piecewise function (White, 2003),

$$f = \begin{cases} \left(1.8 \log_{10} \left[\frac{Re}{6.9}\right]\right)^{-2} & Re > 10^5 \\ 0.316(Re)^{-1/4} & 2300 < Re < 10^5 \\ \frac{Re}{64} & Re < 2300 \end{cases} \quad (4.9)$$

Minor losses due to expansions, contractions, and bends are generally defined as (Kelkar, 1999)

$$\Delta P_{minor} = K \frac{1}{2} \rho \left(\frac{Q}{A}\right)^C + \frac{B}{Re} \quad (4.10)$$

where Q is the volumetric flow rate, Re is the Reynolds number, and B is a constant. Since the fluid used for coolant is water, the Reynolds number is large enough that the second term can be ignored. Also, at large Reynolds numbers, the flow will be turbulent, so C will be 2. The volumetric flow rate equals the product of the average flow velocity and the cross-sectional flow area, so Eq. (4.10) simplifies to

$$\Delta P_{minor} = K \frac{1}{2} \rho V^2 \quad (4.11)$$

The loss coefficient, K , is dependent on the geometry of the individual piece, and the value is experimentally determined for many different shapes. For a sharp contraction from a reservoir to a channel, the inlet loss coefficient can be found from (White, 2003 and Streeter, 1961)

$$K_{contraction} = 0.42 \left(1 - \left(\frac{A_{small}}{A_{large}} \right) \right) \quad (4.12)$$

The expression for the coefficient has been thoroughly studied in an attempt to describe the negative pressure buildup just inside the smaller diameter channel, a phenomenon referred to as a vena contracta (Orselli et al., 2005, Ozlap et al., 2007, Sisavath et al., 2002). Similarly, for an expansion from a channel to a reservoir, the outlet loss coefficient is given as (White, 2003)

$$K_{expansion} = \left(1 - \left(\frac{A_{small}}{A_{large}} \right) \right)^2 \quad (4.13)$$

From mass conservation, the mass flow rate for a constant cross-sectional area is

$$\dot{m} \equiv \rho V A = \rho V \left(\frac{\pi}{4} \right) D^2. \quad (4.14)$$

As with any transport equation, there are three features: a gradient that drives the flow, the flow itself, and a resistance to that flow. In Ohm's law these features are voltage, current, and resistance, respectively. In the same way that the voltage pushes the charges and induces the current, the water pressure pushes the fluid and induces a mass flow. The resistance is any place in the flow that contains an irreversible loss. In electrical terms, the resistor heats up when it absorbs some potential electrical energy from the electrical current, thus causing a decrease in voltage. Similarly, the hydraulic resistor saps some of the potential energy from the flow, thus causing a decrease in water pressure, mathematically described as

$$\Delta P_t = \dot{m}R_{flow}. \quad (4.15)$$

Of the hydraulic resistors, frictional losses and "minor" losses form the two main categories. For these, Eq. (4.15) can be written as

$$\Delta P_{friction} = f \frac{L}{D} \frac{\dot{m}V}{2A} \quad (4.16)$$

$$\Delta P_{minor} = K_{c/e} \frac{\dot{m}V}{A} \quad (4.17)$$

for frictional resistances and contraction/expansion resistances, respectively. To reiterate the parallel between hydraulic and electrical circuits, the corresponding variables are listed in Table 4.1.

Table 4.1 Element-by-element comparison of Ohm's Law for electrical and hydraulic systems

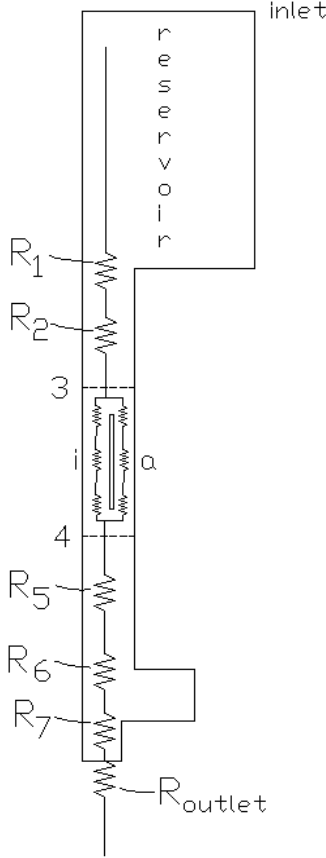
Property	Electrical	Hydraulic
Driving force	ΔV	ΔP
Flow	I	\dot{m}
Resistance to flow	R	$R_{\text{contraction}} = K_c \frac{2V}{\pi D^2}$ $R_{\text{friction}} = f \frac{2LV}{\pi D^3}$ $R_{\text{expansion}} = K_e \frac{2V}{\pi D^2}$

A flow resistance network can be constructed for the flow geometry of interest, similar to how an electric resistance network is created for a circuit. For elements where there is a series of pressure drops and the flow is constant, resistors are placed in series. For elements where the flow can split into two paths, resistors are placed in parallel. Like their electrical counterparts, resistors in series add and resistors in parallel have their reciprocals added, as shown in Eq. (4.18).

$$R_{\text{combined}} = \left[\sum_i \frac{1}{R_i} \right]^{-1} \quad (4.18)$$

Using the sketch of a single channel shown in Fig. 4.3, a resistance network can be created:

$$\frac{\Delta P_t}{m} = R_1 + R_2 + R_{34} + R_5 + R_6 + R_7 + R_{outlet}, \quad (4.19)$$



where the resistances are

$$R_1 = R_{contraction} = K_{1,c} \frac{2V_2}{\pi D_2^2} \quad (4.20)$$

$$R_2 = R_{friction} = f_2 \frac{2L_{13}V_2}{D_2^3} \quad (4.21)$$

From Eq. (4.18), R_{34} is

$$R_{34} = \left(\frac{1}{R_a} + \frac{1}{R_i} \right)^{-1}, \quad (4.22)$$

Figure 4.3 Single channel system with resistors.

as it consists of two flow paths in parallel. Each of these paths is made up of an inlet resistor, a frictional resistor, and an outlet resistor, shown in Fig. 4.3.

$$R_a = R_{contraction} + R_{friction} + R_{expansion} = \left(K_{a,c} + f_a \frac{L_c}{D_a} + K_{a,e} \right) \frac{2V_a}{\pi D_a^2} \quad (4.23)$$

$$R_i = R_{contraction} + R_{friction} + R_{expansion} = \left(K_{i,c} + f_i \frac{L_c}{D_i} + K_{i,e} \right) \frac{2V_i}{\pi D_i^2} \quad (4.24)$$

$$R_5 = R_{friction} = f_5 \frac{2L_{46}V_5}{D_5^3} \quad (4.25)$$

$$R_6 = R_{expansion} = K_{6,e} \frac{2V_5}{\pi D_5^2} \quad (4.26)$$

$$R_7 = R_{contraction} = K_{7,c} \frac{2V_{drain}}{\pi D_{drain}^2} \quad (4.27)$$

$$R_{outlet} = R_{expansion} = K_{outlet,e} \frac{2V_{drain}}{\pi D_{drain}^2} \quad (4.28)$$

For simplicity, the thickness of the cylinder is split in two and extended backwards. This is the short dotted line in Fig. 4.4. Then, half of the thickness of the target is attributed to the annular flow and the other half is attributed to the inner flow. Therefore, before the flow reaches the cylinder, it can be represented by two separate flows with different cross-sectional areas and different velocities. In Fig. 4.4, these areas are distinguished by their radii, R_{3a} and R_{3i} . The ratios of area needed for the contraction coefficients are then equal

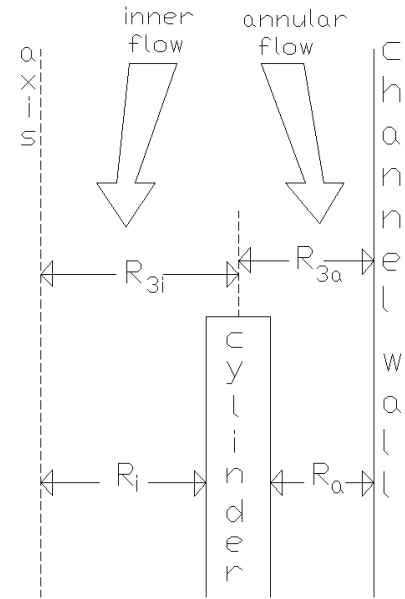


Figure 4.4 Diagram of the flow around the target.

to the squares of the ratios of radii, R_a divided by R_{3a} and R_i divided by R_{3i} . This same logic is applied to the rear of the target to obtain the expansion coefficients. It should also be noted that the hydraulic diameter is defined as

$$D_h = \frac{4A}{\mathcal{P}}. \quad (4.29)$$

For an annulus, this reduces to the difference between the outer and inner diameters.

Combining Eqs. (4.15) and (4.28), the total pressure drop across the outlet resistor is

$$\Delta P_t = K_e \frac{2V_{drain}}{\pi D_{drain}} \dot{m}. \quad (4.30)$$

Using the conservation of mass in Eq. (4.14), this reduces to

$$\Delta P_t = K_e \frac{\rho V_{drain}^2}{2}. \quad (4.31)$$

The drain expands into a semi-infinite reservoir, so the expansion coefficient is approximately 1 by Eq. (4.13). Also, since the total outlet pressure is defined to be 0, the total pressure inside the drain is

$$P_{t,drain} = \frac{\rho V_{drain}^2}{2} \quad (4.32)$$

In Eq. (4.4), the total pressure is stated as the sum of the static and dynamic pressures (hydrostatic neglected),

$$P_{t,drain} = P_s + P_d = P_s + \frac{\rho V_{drain}^2}{2}, \quad (4.33)$$

meaning that the static pressure in the drain is 0. Therefore, the total pressure drop across the model in Eq. (4.19) can reduce to

$$\Delta P_{total,inlet-outlet} = \Delta P_{static,inlet-drain} = \Delta P_{driving}. \quad (4.34)$$

The total and static pressures in the reservoir are equal because the velocity in the reservoir is small enough to be neglected.

Substituting Eq. (4.34) and the resistor definitions into Eq. (4.19) and rearranging, the ensuing equation becomes

$$\begin{aligned} \Delta P_{driving} = & K_{1,c} \frac{\rho V_2^2}{2} + f_2 \frac{L_{13}}{D_2} \frac{\rho V_2^2}{2} + \left(K_{a,c} + f_a \frac{L_c}{D_a} + K_{a,e} \right) \frac{\rho V_a^2}{2} + \\ & \left(f_5 \frac{L_{46}}{D_5} + K_{6,e} \right) \frac{\rho V_5^2}{2} + (1 + K_{7,c}) \frac{\rho V_{drain}^2}{2}. \end{aligned} \quad (4.35)$$

Since the flow diameters in the channel are identical above and below the target, V_2 and V_5 are identical under mass conservation. Similarly, a relationship can be established between the velocities in the channel and the drain via Eq. (4.14) as

$$V_{drain} = \left(\frac{A_5}{A_{drain}} \right) V_5. \quad (4.36)$$

Recalling that the pressure drops across parallel entities are equal, Eq. (4.15) is applied directly to the flows around the target to obtain a relationship between velocities V_2 and V_a .

$$\Delta P_{t,34} = R_a \dot{m}_a = R_i \dot{m}_i = \left(K_{a,c} + f_a \frac{L_c}{D_a} + K_{a,e} \right) \frac{\rho V_a^2}{2} = \left(K_{i,c} + f_i \frac{L_c}{D_i} + K_{i,e} \right) \frac{\rho V_i^2}{2} \quad (4.37)$$

The velocity through the inner section of the target, V_i , is then eliminated through the use of a mass balance. As the mass flow rates add in parallel, the mass flow rate at point 2 is known to equal the sum of the mass flows in the annular and inner flow. Substituting in Eq. (4.14) and rearranging to solve for V_i , the result looks like

$$V_i = \frac{A_2}{A_i} V_2 - \frac{A_a}{A_i} V_a. \quad (4.38)$$

Substituting Eq. (4.38) and canceling the factors of density, Eq. (4.37) becomes

$$\left(K_{a,c} + f_a \frac{L_c}{D_a} + K_{a,e} \right) V_a^2 - \left(K_{i,c} + f_i \frac{L_c}{D_i} + K_{i,e} \right) \left(\frac{A_2}{A_i} V_2 - \frac{A_a}{A_i} V_a \right)^2 = 0. \quad (4.39)$$

Keep in mind that the friction factor for the inner flow, f_i , is also a function of the inner velocity, V_i , so Eq. (4.39) cannot easily be rearranged to solve for V_2 purely as a function of V_a .

As the friction factors contain nonlinearities with respect to the velocities, the model is difficult to be solved directly. Rather, it is much easier to find the roots of the system of equations using the Newton-Raphson method. To use the Newton-Raphson method, two things are required: the function matrix and the Jacobian matrix. The function matrix is a 2-by-1 matrix consisting of Eqs. (4.35) and (4.39).

$$\mathbf{f} = \begin{Bmatrix} f_1(V_2, V_a) \\ f_2(V_2, V_a) \end{Bmatrix} = \begin{Bmatrix} \text{Eq. (4.35)} \\ \text{Eq. (4.39)} \end{Bmatrix} = \mathbf{0} \quad (4.40)$$

The Jacobian matrix is a 2-by-2 matrix which is constructed from partial derivatives of each of the functions in the function matrix.

$$J = \begin{bmatrix} \frac{\partial f_1}{\partial V_2} & \frac{\partial f_1}{\partial V_a} \\ \frac{\partial f_2}{\partial V_2} & \frac{\partial f_2}{\partial V_a} \end{bmatrix} \quad (4.41)$$

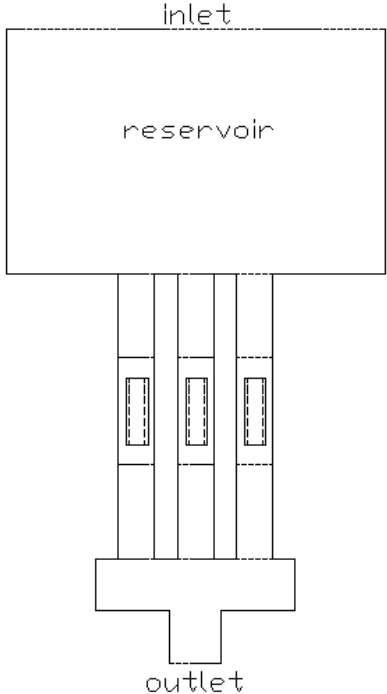
In the Newton-Raphson method, the Jacobian matrix is used to determine the way in which the unknown variables in the function matrix are changing the functions themselves. Its inverse is then applied to the function matrix along with a guess matrix, x^i , to get an updated guess, x^{i+1} .

$$x^{i+1} = x^i - J^{-1}f(x^i) \quad (4.42)$$

Equation (4.42) is repeated until the iterations have converged on a solution. Pressure drops and mass flow rates are then found by substituting values for V_2 and V_a into previously established equations.

4.3 Hydraulic Model for Multiple Channels

As stated before, a particularly attractive feature of the FNM is the ease with which geometries can be altered. Expanding the model to accommodate multiple flow channels is no exception. To find the total hydraulic resistance of all the channels together, Eq. (4.18) is used:



$$\begin{aligned} R_{channels} &= \left(\sum_{i=1}^n \frac{1}{R_{channel,i}} \right)^{-1} \\ &= \left(\frac{n}{R_{channel}} \right)^{-1} = \frac{R_{channel}}{n} \end{aligned} \quad (4.43)$$

where n is the number of parallel flow channels and $R_{channel}$ is the total resistance of a single channel. All flow channels are assumed to be identical. From Figs. 4.5 and 4.6, this includes resistances in Eq. (4.20) – (4.26), meaning

Figure 4.5 Diagram of a 3-channel system.

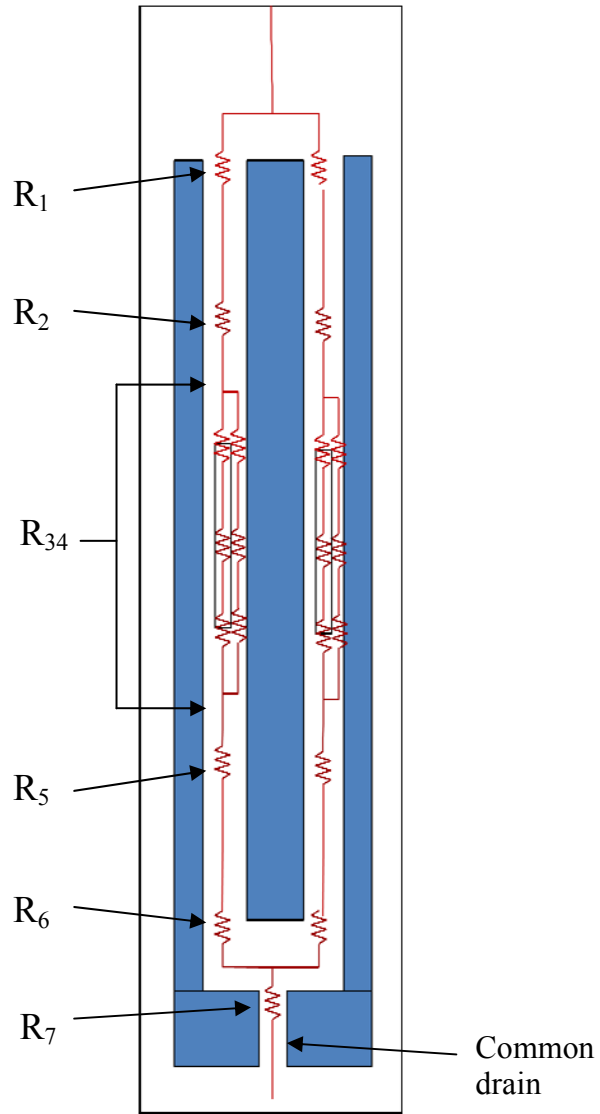


Figure 4.6 Hydraulic resistance network for a 2-channel system

$$, \tag{4.44}$$

where R_{34} is still the same as in Eq. (4.22). Combining this with the other resistors in the system and substituting, Eq. (4.15) becomes

$$\frac{\Delta P_s}{\dot{m}} = \frac{R_1 + R_2 + R_{34} + R_5 + R_6}{n} + R_7, \quad (4.45)$$

where \dot{m} here is the total mass flow through the system. The static pressure drop remains the same as Eq. (4.34), so Eq. (4.45) is then

$$\Delta P_{driving} = \left(\frac{(R_1 + R_2 + R_{34} + R_5 + R_6)}{n} + R_7 \right) \dot{m}_{tot} \quad (4.46)$$

Distributing the mass flow rate and inserting the resistor definitions, this becomes

$$\begin{aligned} \Delta P_{driving} = & \left(K_{1,c} + f_2 \frac{L_{13}}{D_2} \right) \frac{\rho V_2^2}{2} + \left(K_{a,c} + f_a \frac{L_c}{D_a} + K_{a,e} \right) \frac{\rho V_a^2}{2} + \\ & \left(K_{6,e} + f_5 \frac{L_{46}}{D_5} \right) \frac{\rho V_5^2}{2} + (K_{7,c} + 1) \frac{\rho V_{drain}^2}{2} \end{aligned} \quad (4.47).$$

In the same way as in the single channel, Eq. (4.47) is reduced down to a function of just V_2 and V_a . In this process, V_{drain} is slightly different than in Eq. (4.36):

$$V_{drain} = n \left(\frac{A_5}{A_{drain}} \right) V_5. \quad (4.48)$$

The final form this equation takes is

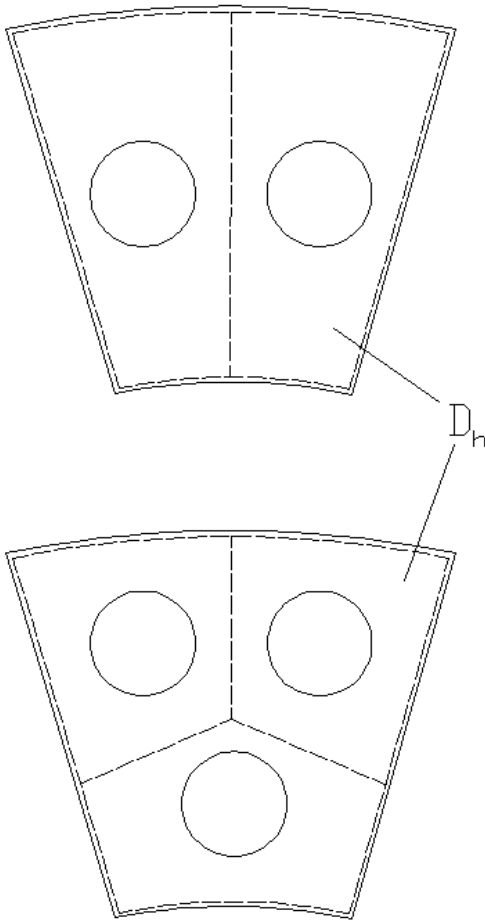
$$\Delta P_{driving} = \left(K_{1,c} + f_2 \frac{L_{13}}{D_2} + f_5 \frac{L_{46}}{D_5} + K_{6,e} + (1 + K_{7,c}) \left[n \left(\frac{A_5}{A_{drain}} \right) \right]^2 \right) \frac{\rho V_2^2}{2} + \left(K_{a,c} + f_a \frac{L_c}{D_a} + K_{a,e} \right) \frac{\rho V_a^2}{2} \quad (4.49)$$

From Eq. (4.37) onward, the solution process follows verbatim from the single channel model.

A separate item of significance for the multiple channel models is the way the inlet and outlet coefficients are defined. In Eq. (4.12) the contraction coefficient was stated to be

$$K_c = 0.42 \left[1 - \left(\frac{D_{small}}{D_{large}} \right)^2 \right]. \quad (4.12)$$

Now that the reservoir is flowing into more than one channel, the effective cross-sectional area that is feeding each channel decreases. For example, when there was one channel, the entire reservoir flowed into that channel. But, if there are two channels in parallel, half of the cross-sectional area of the reservoir is dedicated to one channel and the other half to the second channel. As such, multiple smaller diameters, dubbed D_h for hydraulic diameter, replace D_{large} in Eq. (4.12). These hydraulic diameters are representative of the piece of the reservoir each channel “sees” and are displayed in Fig. 4.7. The diameters are calculated from Eq. (4.29) and are based off the area and perimeter mapped out by the dashed lines in Fig. 4.7. Updated, Eq. (4.12) becomes



$$K_c = 0.42 \left[1 - \left(\frac{D_{channel}}{D_h} \right)^2 \right]. \quad (4.50)$$

The same logic is applied Eq. (4.13) to obtain the expansion coefficient specifically for the transition from the flow channel to the common area just before the drain.

$$K_e = \left(1 - n \frac{A_{channel}}{A_{wedge}} \right)^2. \quad (4.51)$$

Figure 4.7 Hydraulic diameters for 2 and 3 parallel channels

Chapter 5 HEAT TRANSFER – RESISTANCE NETWORK

5.1 Background

In its full form, solving for the heat transfer from the target to the coolant flow is a 3-dimensional problem. Like with the hydraulic model, it is possible to be solved numerically with a high degree of accuracy. Again, though, the numeric approach becomes time- and labor-intensive as the model geometry changes. Fortunately, the heat transfer can be reduced to quasi 1-dimension and FNM can be used again. This simplification is a result of assuming angular symmetry for the annular cylinder target. This dimension along the flow is described by the variable “ z ” in the axisymmetric representation of the model in Fig. 5.1. Once the heat transfer for the quasi 1-dimensional model is derived, the FNM components are identified, and a resistance network is formed.

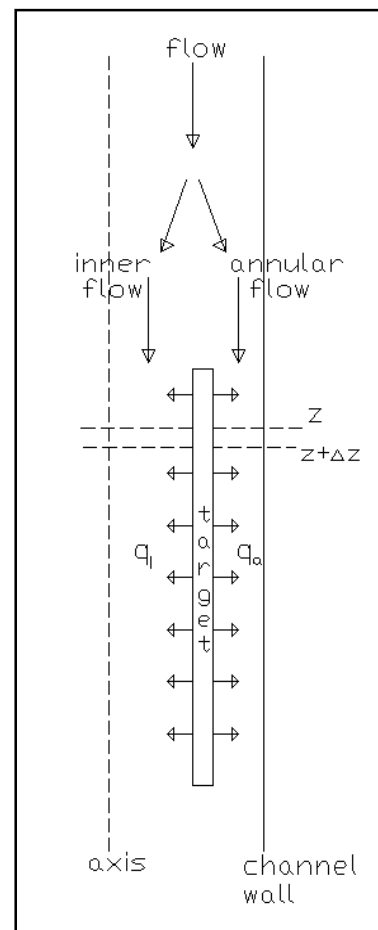


Figure 5.1 Axisymmetric representation of heat flow

5.2 Single Channel Heat Transfer

The total heat transfer in the interval z to $z + \Delta z$ from the target in Fig. 5.1 is found from the energy balance (Incropera, 2002)

$$\mathcal{P}h(T_w - \bar{T}_f)\Delta z + \dot{m}c\bar{T}_{f,z} - \dot{m}c\bar{T}_{f,z+\Delta z} = 0, \quad (5.1)$$

where the specific heat, c , does not need to be defined as a constant pressure or volume, as they are identical for an incompressible fluid. The perimeter and heat transfer coefficient are defined by

$$\mathcal{P}_i = \pi D_i \quad (5.2a)$$

$$\mathcal{P}_a = \pi D_a \quad (5.2b)$$

and

$$h = \frac{k}{D} Nu, \quad (5.3)$$

respectively. Because the geometry being examined is a smooth cylinder and turbulent flow, the Nusselt number can be found from the Dittus-Boelter correlation (Incropera, 2002)

$$Nu_{fd} = 0.023 Re^{0.8} Pr^{0.4}. \quad (5.4)$$

The Prandtl number is a fluid property, which is the ratio of viscous to thermal diffusion rates, defined as

$$Pr = \frac{\nu}{\alpha} = \frac{\nu\rho c}{k}. \quad (5.5)$$

Although it is intended for fully developed circular channel flow, Eq. (5.4) can also be applied to the annular flow, as “a tube annulus can be treated as a noncircular duct with a hydraulic diameter” under fully developed turbulent conditions (Cengel, 2003). However, as explained in Chapter 4, the coolant flowing past the target is developing for the entire length. As a result, the fully developed Nusselt number requires a correction factor, described by Gnielinski (1976) (originally from Hausen (1959))

$$\frac{Nu}{Nu_{fd}} = 1 + \left(\frac{L}{D}\right)^{\frac{2}{3}}. \quad (5.6)$$

With a developing flow Nusselt number in place, computation of the heat transfer coefficient is straightforward from Eq. (5.3).

To find the mean flow temperature as it heats up along the annular cylinder, Eq. (5.1) is divided by Δz , and the limit as $\Delta z \rightarrow 0$ is taken:

$$\dot{m}c \frac{d\bar{T}_f}{dz} - Ph(T_w - \bar{T}_f) = 0 \quad (5.7)$$

From Chapter 3, the target wall temperature, T_w , is taken to be a constant. To simplify the analysis, the temperature difference θ is defined as:

$$\theta = \bar{T}_f - T_w \quad (5.8)$$

Since the wall temperature is constant,

$$\frac{d\theta}{dz} = \frac{d\bar{T}_f}{dz}. \quad (5.9)$$

Substituting these two relationships into Eq. (5.7), the resulting equation transforms into the easily solvable first order differential equation when the heat transfer coefficient, h , is taken as an average over the surface:

$$\frac{\dot{m}c}{Ph} \frac{d\theta}{dz} + \theta = 0. \quad (5.10)$$

Integrating from the leading edge of the cylinder,

$$\theta = C e^{-\frac{Ph}{\dot{m}c}z}. \quad (5.11)$$

The constant of integration is found by applying the necessary boundary condition at the front of the cylinder ($z = 0$).

$$@z = 0 \quad \theta = T_w - T_{f,initial} \quad (5.12)$$

Applying the boundary condition and rewriting in terms of temperatures,

$$T_w - \bar{T}_f = (T_w - T_{f,initial})e^{-\frac{Ph}{\dot{m}c}z}. \quad (5.13)$$

Rearranging Eq. (5.13):

$$\bar{T}_f(z) = T_{f,initial} + (T_w - T_{f,initial}) \left[1 - e^{-\frac{Ph}{\dot{m}c}z} \right]. \quad (5.14)$$

Finally, combining Eq. (5.14) applied to the entire length of the target (i.e., $z = L$) and an energy balance over the water around the target yields

$$q = \dot{m}c(T_{f,final} - T_{f,initial}) = \dot{m}c(T_w - T_{f,initial})[1 - e^{-NTU}]. \quad (5.15)$$

where the number of transfer units, or NTUs, is commonly defined in heat exchanger theory to be (Incropera, 2002)

$$NTU = \frac{hPL}{\dot{m}c}. \quad (5.16)$$

Physically, this property represents the ratio of convection to the flow heat capacity.

The bracketed term in Eq. (5.15) is a decaying exponential, ranging from 0 to 1. Consequently, the maximum heat transfer occurs when this approaches a value of 1,

$$q_{max} = \dot{m}c(T_w - T_{f,initial}). \quad (5.17)$$

This means the bracketed term is also a measure of the effectiveness of the heat exchanger, defined as (Incropera, 2002)

$$\varepsilon \equiv \frac{q}{q_{max}} = 1 - e^{-NTU}. \quad (5.18)$$

Through substitution and rearranging into the form of Ohm's law, Eq. (5.15) becomes

$$\Delta T = \frac{q}{\dot{m}c\varepsilon}, \quad (5.19)$$

and the FNM terms appear. Here, the resistance is defined as

$$R = \frac{1}{\dot{m}c\varepsilon} = (\dot{m}c[1 - e^{-NTU}])^{-1} \quad (5.20)$$

and can be applied to either the inner or annular flow. The driving force and flow elements are listed with the resistance in Table 5.1.

Table 5.1 Element-by-element comparison of electrical and thermal systems.

Property	Electrical	Thermal
Driving force	ΔV	ΔT
Flow	I	q
Resistance to flow	R	$(\dot{m}c[1 - e^{-NTU}])^{-1}$

Finally, to get the total heat transfer from a single target in a single channel, the resistances must be combined. Since the inner and annular surfaces of the target are in parallel with each other, the total thermal resistance is

$$R_{tot} = \left(\frac{1}{R_a} + \frac{1}{R_i} \right)^{-1}. \quad (5.21)$$

Knowing that the temperature differences in parallel are the same, the total heat transfer from a single target is

$$q_{tot} = \Delta T(\dot{m}_a c \varepsilon_a + \dot{m}_i c \varepsilon_i). \quad (5.22)$$

5.3 Multiple Channel Heat Transfer

When expanding the thermal resistance network from a single channel to multiple channel system, Eq. (5.21) must be expanded to account for the added resistors. Since every thermal resistor is in parallel with the others, seen in Fig. 5.3, the total thermal resistance is defined as:

$$R_{tot} = \left[\sum_1^n \left(\frac{1}{R_a} + \frac{1}{R_i} \right) \right]^{-1}. \quad (5.23)$$

In the context of this thesis, all of the channels in the multiple channel model are identical, and consequently so are their resistances, meaning that Eq. (5.23) reduces to

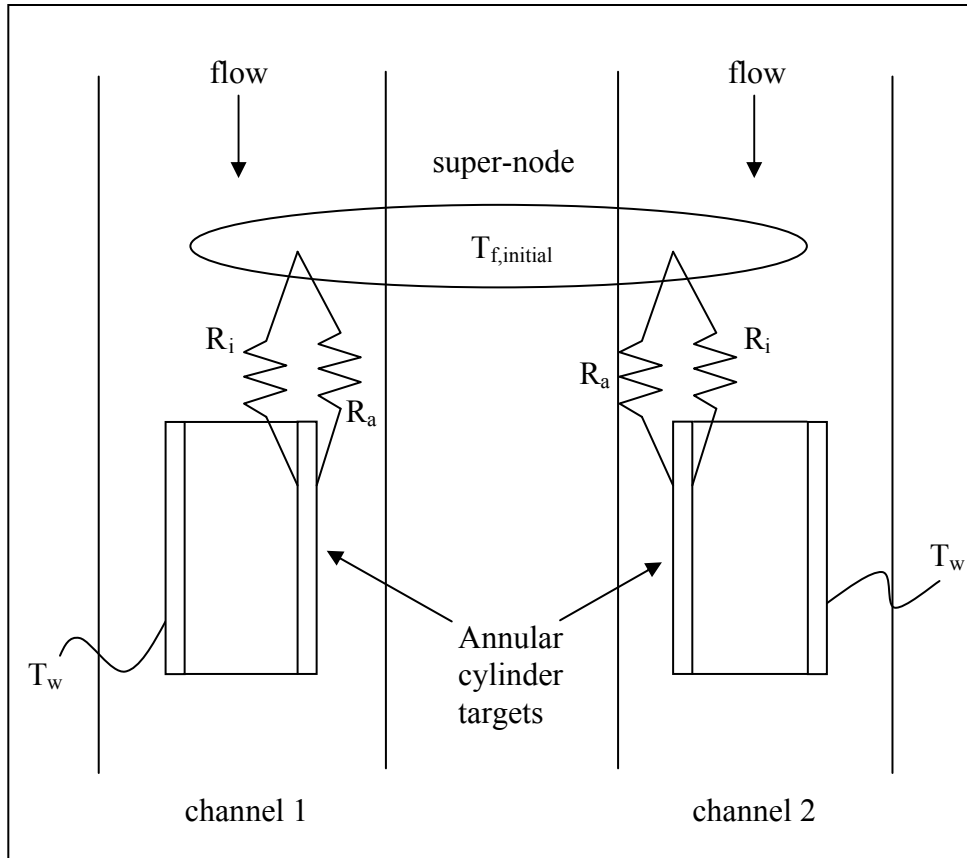


Figure 5.2 Thermal resistance network for a two channel system

$$R_{tot} = \left[n \left(\frac{1}{R_a} + \frac{1}{R_i} \right) \right]^{-1}. \quad (5.24)$$

Applied to the thermal version of Ohm's law, the total heat transfer for a multiple channel system is

$$q_{tot} = n\Delta T(\dot{m}_a c \varepsilon_a + \dot{m}_i c \varepsilon_i). \quad (5.25)$$

Unfortunately, the concept of thermal resistance does not parallel the Ohm's law analogy perfectly. In both electrical and hydraulic resistance systems, the flow physically

points in the direction of the driving potential. In the thermal resistor analogy, this is no longer the case. The resistors in Fig. 5.2 infer that the heat should flow upstream, as this is the direction of the thermal potential; however, the heat actually flows downstream, as the water is the physical carrier of the thermal energy. Regardless, the mathematics of the thermal resistor analogy work out too conveniently to ignore.

Chapter 6

ENTROPY GENERATION

6.1 Background

The previous chapters have provided sufficient system models to analyze a multiple channel system; however, FNM is not the only modeling approach. A preliminary entropy generation model of a multi-channel system is developed here.

In the hydrodynamic model, the irreversible resistors are examined to determine relative effects of individual elements. As the resistor increases in value, it increasingly controls and limits the flow. In the entropy generation model, the driving pressure is thought of as a “bank” of useful energy. As the driving pressure is expended on each resistor, there is less to be applied to the others. The entropy generation model attempts to find the best use of this energy. As the dispersion of this energy is experienced in part through friction in the flow, the general idea is to increase the amount of this energy that is expended over the target. This will increase the coolant mixing around the target, leading to a more efficient transfer of heat from the target.

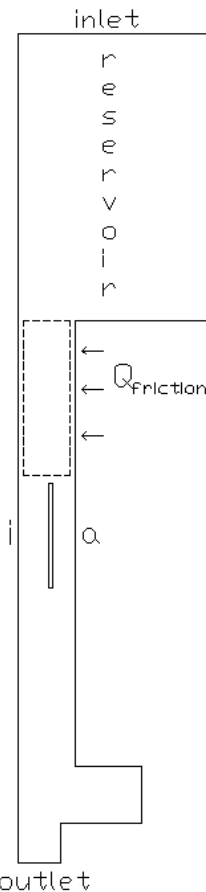
6.2 Hydrodynamic Entropy Generation

Hydrodynamic entropy generation is a result of irreversibility in the flow. As discussed in Chapter 4, there are two primary causes of hydraulic irreversibility: friction and minor losses.

6.2.1 Entropy from Friction

The first law of thermodynamics for an open system is

$$\frac{dE}{dt} = \sum_i \dot{Q}_i - \sum_i \dot{W}_i + \sum_{in} \dot{m} \left(h + \frac{v^2}{2} + gz \right) - \sum_{out} \dot{m} \left(h + \frac{v^2}{2} + gz \right). \quad (6.1)$$



Examining the energy boundary around the steady-state system in Fig. 6.1, Eq. (6.1) reduces to

$$\dot{Q}_{friction} = \dot{m}(h_{out} - h_{in}) \quad (6.2)$$

where the enthalpy is defined as

$$h = u + Pv. \quad (6.3)$$

Since the difference in specific internal energy is represented as

$$u_{out} - u_{in} = c(T_{out} - T_{in}), \quad (6.4)$$

Figure 6.1 Energy boundary along a section of channel for friction.

and the specific volume is a constant for an incompressible fluid, Eq. (6.2) is

$$\dot{Q}_{friction} = \dot{m}c(T_{out} - T_{in}) - \dot{m}v(P_{in} - P_{out})_{irrev}. \quad (6.5)$$

Since the energy boundary in Fig. 6.1 is applied over a constant cross-sectional area, there is no reversible pressure drop.

The second law of thermodynamics for an open system is

$$\dot{S}_{gen} = \frac{dS}{dt} - \sum_i \frac{\dot{Q}_i}{T_i} + \sum_{out} \dot{m}S - \sum_{in} \dot{m}S. \quad (6.6)$$

Again, the system displayed in Fig. 6.1 reduces this:

$$\dot{S}_{gen} = -\frac{\dot{Q}_i}{T_i} + \dot{m}S_{out} - \dot{m}S_{in}. \quad (6.7)$$

For an incompressible fluid, the difference in specific entropies is

$$S_{out} - S_{in} = c \ln \left(\frac{T_{out}}{T_{in}} \right). \quad (6.8)$$

Substituting Eqs. (6.5) and (6.8), Eq. (6.7) becomes

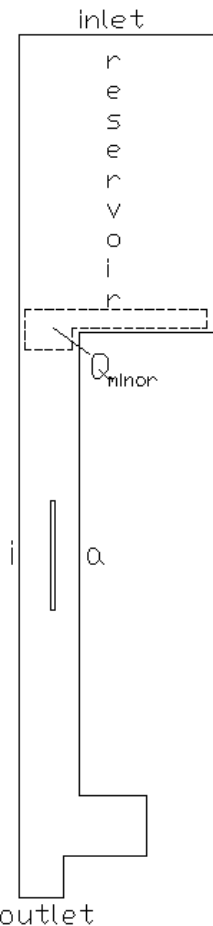
$$\dot{S}_{gen} = \frac{\dot{m}v}{T_{in}} (P_{in} - P_{out})_{irrev} - \dot{m}c \frac{(T_{out} - T_{in})}{T_{in}} + \dot{m}c \ln \left(\frac{T_{out}}{T_{in}} \right). \quad (6.9)$$

T_{in} and T_{out} are approximately equal, so the natural logarithm can be simplified with a first-order Taylor expansion:

$$\ln\left(\frac{T_{out}}{T_{in}}\right) \approx \frac{T_{out}}{T_{in}} - 1 = \frac{T_{out}-T_{in}}{T_{in}}. \quad (6.10)$$

Canceling terms, Eq. (6.9) reduces to

$$\dot{S}_{gen,friction} = \frac{\dot{m}v}{T_{in}} \Delta P_{irrev}. \quad (6.11)$$



6.2.2 Entropy from Minor Losses

Similar to the reduction from Eq. (6.1) to Eq. (6.2), the energy boundary in Fig. 6.2 simplifies the general first law for a contraction/expansion to

$$\dot{Q}_{minor} = \dot{m}(h_{out} - h_{in}) + \dot{m}\left(\frac{V_{out}^2}{2} - \frac{V_{in}^2}{2}\right). \quad (6.12)$$

where \dot{Q}_{minor} is the representative heat generated from the irreversible losses in the contraction/expansion. Substituting in the definition of enthalpy in Eq. (6.3):

Figure 6.2 Energy boundary for a minor loss.

$$\dot{Q}_{minor} = \dot{m} \left[c(T_{out} - T_{in}) + v(P_{out} - P_{in}) + \left(\frac{V_{out}^2}{2} - \frac{V_{in}^2}{2} \right) \right]. \quad (6.13)$$

Removing the reversible terms which yield no heat generation, Eq. (6.13) reduces to

$$\dot{Q}_{minor} = \dot{m} [c(T_{out} - T_{in}) - v(P_{in} - P_{out})_{irrev}]. \quad (6.14)$$

As this is the same result as Eq. (6.5), the second law is then applied identically as in Eqs. (6.6) – (6.9). After the first-order Taylor expansion is performed, the entropy generation rate for minor losses is seen to be the same form as that for frictional losses:

$$\dot{S}_{gen,minor} = \frac{\dot{m}v}{T_{in}} \Delta P_{irrev}. \quad (6.15)$$

6.3 Thermal Entropy Generation

To determine if maximization of the hydrodynamic entropy generation rate around the target optimizes heat transfer, the thermal entropy generation rate is calculated. Although the hydrodynamic entropy generation rate can be compared directly against the heat transfer to determine optimized geometry, keeping both the thermal and hydraulic energy transfers in terms of entropy generation allows for a clearer understanding of the trade-offs between the two.

As stated in Eq. (6.6), the second law of thermodynamics for open systems is

$$\dot{S}_{gen} = \frac{dS}{dt} - \sum_i \frac{\dot{Q}_i}{T_i} + \sum_{out} \dot{m}s - \sum_{in} \dot{m}s. \quad (6.6)$$

For a steady-state system with one mass flow inlet, one mass flow outlet, and one energy inlet, Eq. (6.6) reduces to Eq. (6.7):

$$\dot{S}_{gen} = -\frac{\dot{Q}_i}{T_i} + \dot{m}s_{out} - \dot{m}s_{in}, \quad (6.7)$$

where T_i is the constant surface temperature of the target T_w . For an incompressible fluid, the difference in specific entropies is

$$s_{out} - s_{in} = c \ln\left(\frac{T_{out}}{T_{in}}\right). \quad (6.8)$$

Substituting Eq. (6.8) and the rate of heat transfer calculated in Chapter 5, Eq. (6.7) is

$$\dot{S}_{gen} = \dot{m}c \ln\left(\frac{T_{out}}{T_{in}}\right) - \dot{m}c \frac{T_w - T_{f,i}}{T_w} [1 - e^{-NTU}]. \quad (6.16)$$

As T_{out} and T_{in} are similar in value, the natural log is expanded in a first-order Taylor expansion as in Eq. (6.10):

$$\ln\left(\frac{T_{out}}{T_{in}}\right) \approx -1 + \frac{T_{out}}{T_{in}} \quad (6.10)$$

By conservation of energy,

$$\dot{Q} = \dot{m}c(T_{out} - T_{in}). \quad (6.17)$$

Rearranging, Eq. (6.17) becomes

$$\frac{T_{out}}{T_{in}} = 1 + \frac{\dot{Q}}{\dot{m}cT_i}. \quad (6.18)$$

Substituting Eqs. (6.10) and (6.18) into Eq. (6.16):

$$\dot{S}_{gen} = \dot{m}c \frac{T_w - T_{f,i}}{T_{f,i}} [1 - e^{-NTU}] - \dot{m}c \frac{T_w - T_{f,i}}{T_w} [1 - e^{-NTU}]. \quad (6.19)$$

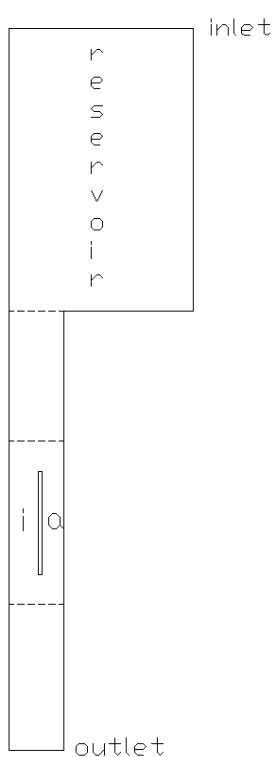
Combining terms, the final form of the thermal entropy generation rate is

$$\dot{S}_{gen} = \dot{m}c \frac{(T_w - T_{f,i})^2}{T_w T_{f,i}} [1 - e^{-NTU}]. \quad (6.20)$$

Currently, optimization results using the entropy generation rates are preliminary and are not included in Chapter 7.

Chapter 7 RESULTS & DISCUSSION

The hydrodynamic and thermal models developed in the previous chapters are general models that can be applied to any number of different geometries in other reactors. To illustrate how to use the models for a specified geometry, they are demonstrated in this chapter for the configuration at MURR.



7.1 Single Channel Results

Although the maximum wedge heat transfer does not come from a single channel model, it is the basis for multi-channel heat transfer. Parametric studies of a single channel model provide a simplified method of observing general trends which can then be used to enhance understanding of the multiple channel models. Before this can happen, though, the single channel analytic model is shown to match its numeric counterpart.

7.1.1. Analytic Model Validation

As shown in Chapter 5, the heat transfer depends on hydraulic properties. Therefore, when comparing the results of the single channel cases for the numeric and analytic models, the

Figure 7.1 Single channel model used to compare analytic and numeric results.

hydraulic properties must first be checked to match before proceeding to the thermal properties. With this in mind, the mass flow rates have been found for the three driving pressures determined in Section 3.1. Figure 7.1 displays the single channel model used for comparison, though the other two models in Fig. 3.6 are also examined to gain a relative perspective. The results are listed in Table 7.1 and plotted in Fig. 7.2.

Table 7.1 Resultant mass flow rates from specified static pressure drops for single channel

Driving pressure (Pa)	Mass flow rates (kg/s)			
	anemometer	annular cylinder	empty N-1	analytic
4940	2.684	2.833	3.110	2.864
8430	3.525	3.726	4.081	3.785
12840	4.368	4.620	5.053	4.676

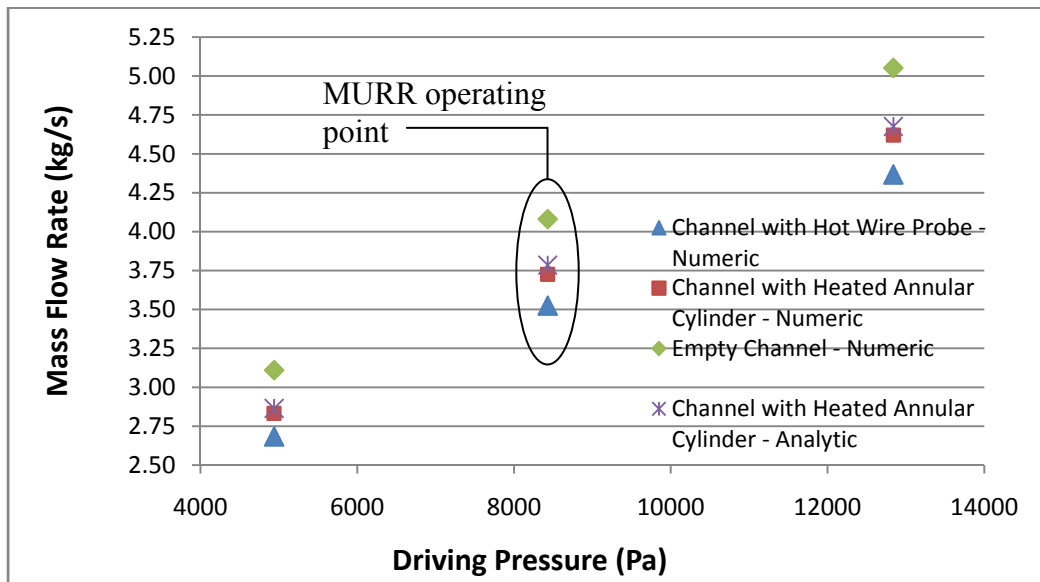


Figure 7.2 Comparison of analytic and numeric mass flow rates for single channel

Clearly, the values for the analytic model fall close to the values for the numeric model. Specifically, all three values of the analytic model differ from the values of the numeric model by less than 2%, well within an acceptable margin.

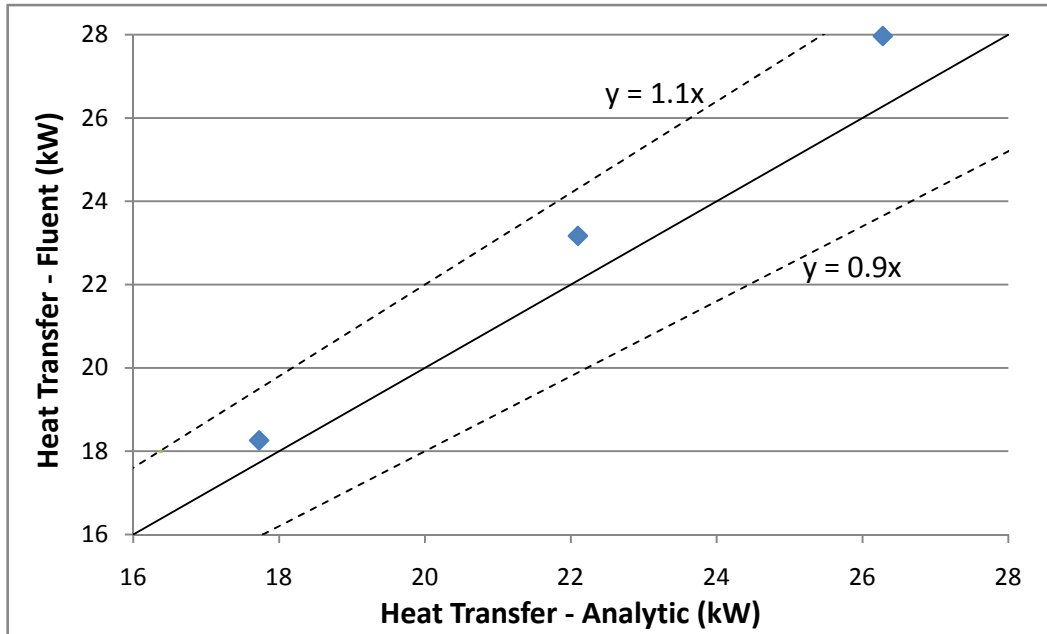


Figure 7.3 Comparison of analytic and numeric heat transfer rates for single channel.

Once the similarity is confirmed for the hydraulic models, the heat transfer equations of Chapter 5 are then used to compute the rates of heat transfer for the analytic model. These values are then plotted in Fig. 7.3 against the values acquired in FLUENT. The two sets do not match up exactly, but to show they are close, $\pm 10\%$ error bars have been added to Fig. 7.3. The data points fall within these bars, with the analytic model under-predicting the numeric by about 5%.

7.1.2 Optimization

Four geometric parameters are studied here: channel diameter, drain diameter, target diameter, and target length. In addition, the effect of the true saturation temperature

of the pool water on heat transfer is examined. Unless otherwise specified, the dimensions used are the ones currently used in the reactor, as listed in Table 7.2.

Table 7.2 Dimensions currently used at MURR.

Channel diameter (m)	0.041275
Drain diameter (m)	0.04445
Target diameter (m)	0.0265 inner, 0.03 outer
Target length (m)	0.152

The drain diameter is an important design parameter as it regulates the flow through the system. If it is too small, it chokes the flow and decreases heat transfer. This is demonstrated in Fig. 7.4. As the drain is expanded, the heat transfer increases without

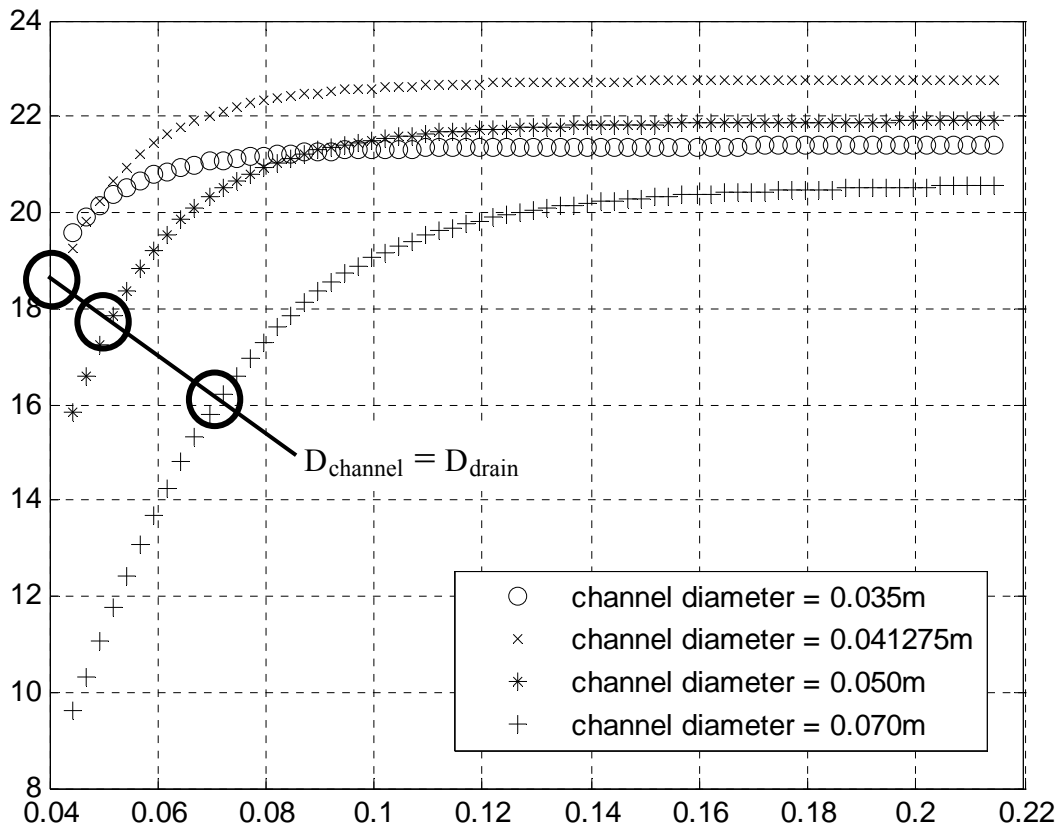


Figure 7.4 Heat transfer from a single channel for a variable drain diameter.

exception. For small drain diameters, this increase in heat transfer is initially linear and then asymptotes at larger drain sizes. The drain diameter at which the total heat transfer begins to asymptote depends on the relative sizes of the drain and channel. The transition occurs about when the drain diameter matches the channel diameter. In Fig. 7.4, these points of equal diameters are circled, and a general trend line is included.

Figure 7.4 implies that there is an optimum channel diameter size. This is clearly confirmed when the heat transfer is against the channel diameter, in Fig. 7.5. As predicted by Fig. 7.4, the maximum heat transfer increases as the drain diameter increases, though the returns are diminished at the optimum channel diameter. The final thing to note in

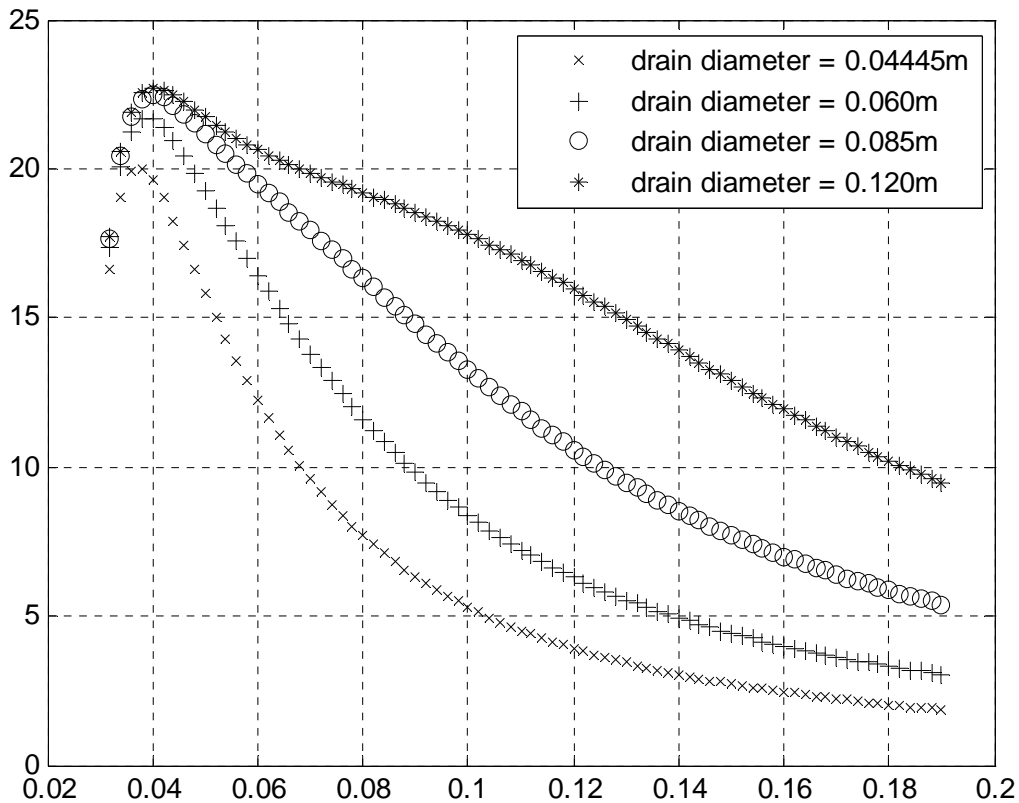


Figure 7.5 Heat transfer from a single channel for a variable channel diameter.

Fig. 7.5 is the “lump” that occurs in the curve for a drain diameter of 0.120m. This is a result of the friction factor in the inner target area transitioning into a low turbulence

regime. As the channel diameter continues to increase, the hydraulic resistance in the annular section decreases. Above a certain diameter, enough of the overall flow is funneled through the annular section that the flow through the inner target area becomes laminar. As a result of the decreased Nusselt number associated with laminar flow heat transfer, the curve becomes discontinuous and the rate of heat transfer falls dramatically, as shown in Fig. 7.6. As there was no study confirming the reason behind the switch to laminar flow, the accuracy of the model in this transitional area is still in question. However, this does not change the results, as the optimum is unaffected.

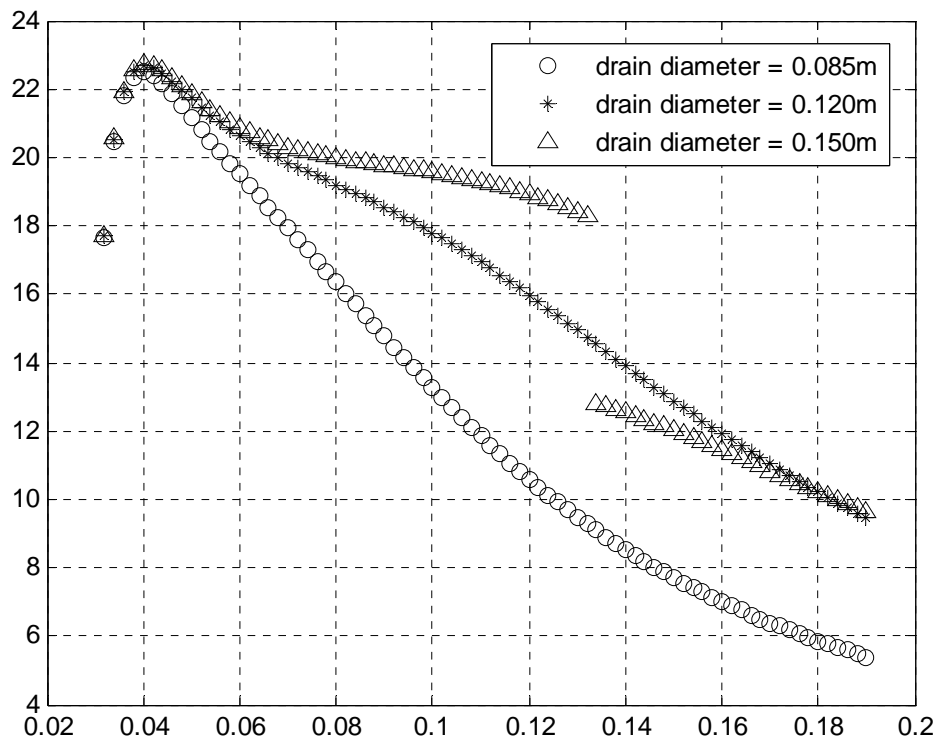


Figure 7.6 Transition to laminar flow in the single channel model.

From Figs. 7.5 and 7.6, it is determined that, under the current reactor configuration, the coolant can remove heat at a rate of approximately 19 kW, while an

optimized geometry increases this to about 23 kW. The geometric parameters and corresponding heat transfer rates for the models are listed in Table. 7.3. Referring back to

Table 7.3 Comparison of geometry and heat transfer rate for current and optimized single channel configurations.

	Channel diameter (m)	Drain diameter (m)	Heat transfer rate (kW)
Current configuration	0.041275	0.04445	19.18
Optimized configuration	0.0405	0.215	22.77

the thermal-neutronics section in Chapter 1, it was found that a 20-gram LEU target (4 grams of uranium-235) generates heat at a rate of 2 kW. As this is significantly less than 19 kW, the current reactor configuration will likely be able to support the irradiation of a single 20-gram LEU target.

7.1.3 Resistor Ratios

The flow resistances serve as a fast way to compare the impact of pressure drop losses. If the resistance of a certain loss is large, this means it has a larger impact on the rest of the flow than a loss with a small resistance and is a good candidate to improve. Earlier, in Fig. 7.4, it was postulated that the drain was choking the flow through the channels. The validity of this is demonstrated in Figs.7.7 and 7.8 which examine the ratio of exit resistance to the total resistance. A value near one implies that most of the flow resistance takes place at the drain, meaning the drain geometry limits the overall flow. The heat transfer responds by decreasing, as shown in Fig. 7.5. On the other hand, if the resistor ratio is near zero, then most of the resistance comes from inside the channel.

When this happens, expanding the drain further will result in a minimal increase in heat transfer, as shown by Figs. 7.8 and 7.4. Also, as the channel diameter increases, the resistor ratio takes longer to approach zero with respect to increasing drain diameter. This effect is seen in Fig. 7.4 as a slower response for the heat transfer to level off towards its maximum.

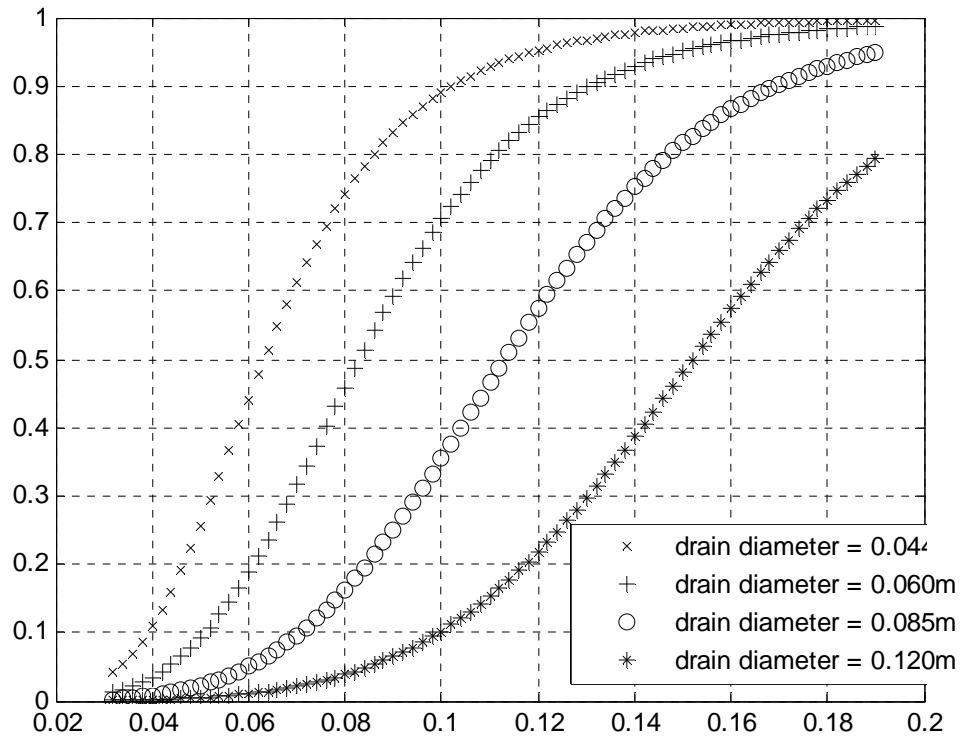


Figure 7.7 Hydraulic resistor ratio for a variable channel diameter.

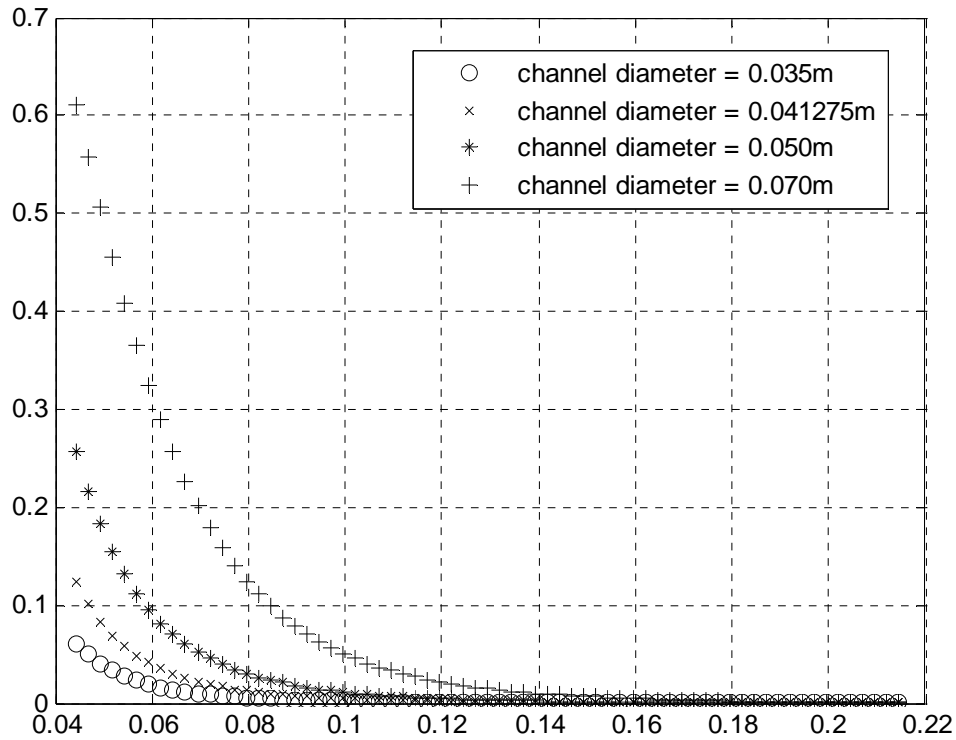


Figure 7.8 Hydraulic resistor ratio for a variable drain diameter.

7.1.4 Target Geometry

Although many of the factors that influence the design of the target are outside the scope of this thesis, it is still useful to understand how the geometry of the target affects the rate of heat transfer to the coolant. As an annular cylinder, there are two main parameters of interest: the length of the target and the diameter. For all cases discussed, the thickness of the target walls is held as a constant 0.0035m.

To show the effect of the target length on the heat transfer, three different lengths are examined for variable channel and drain diameters, as shown in Figs. 7.9 and 7.10. Regardless of the length, the trends for each of the graphs are identical to the heat transfer curve for the standard target length. The values for the maximum heat transfer rates from

Fig. 7.10 are listed in Table 7.4. The fact that the increases in heat transfer are not directly proportional to the increases in target length is not surprising, as the heat transfer is a decaying exponential with respect to the target length. This means that for larger and larger target lengths, the additional heat transfer area becomes less and less effective.

Table 7.4 Effect of target length on maximum rate of heat transfer

Target length (m)	Maximum rate of heat transfer (kW)	Difference from standard target length
0.152 (standard)	19.99	0.0 %
1.5x standard	27.59	+ 38.0 %
2.0x standard	35.00	+ 75.1 %

The effect of the target length on the hydrodynamics is minimal, as the target physically takes up only a small part of the channel. Still, the difference can be seen in Fig. 7.11 as a decrease in the resistor ratio. This is expected because the longer targets generate more friction than the standard target, thus slightly raising the total resistance.

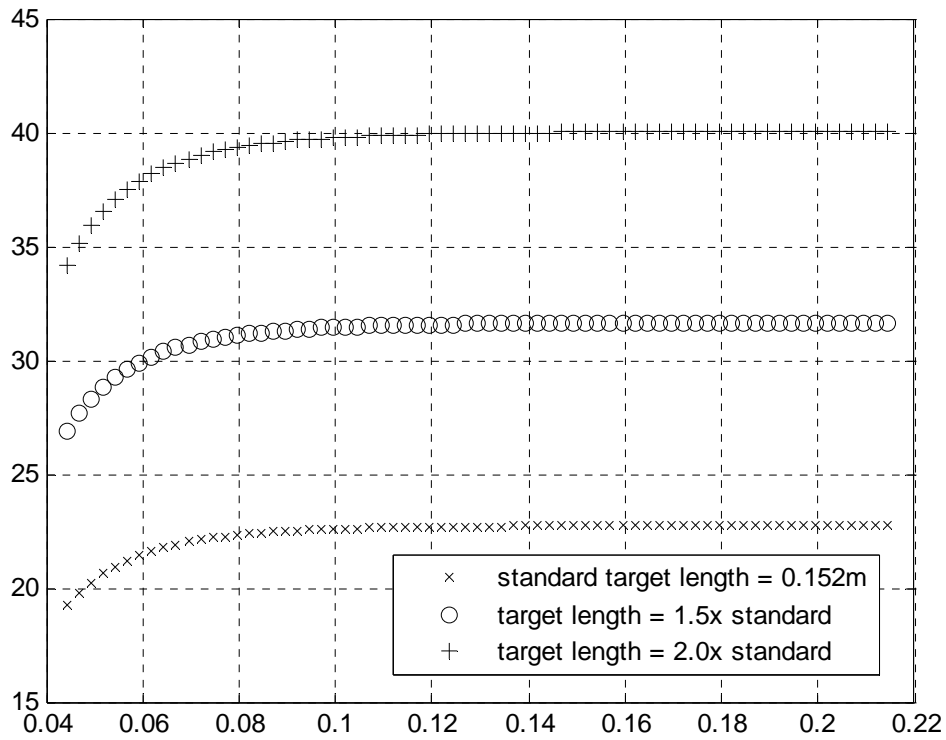


Figure 7.9 Effect of target length on the rate of heat transfer with varying drain diameter.

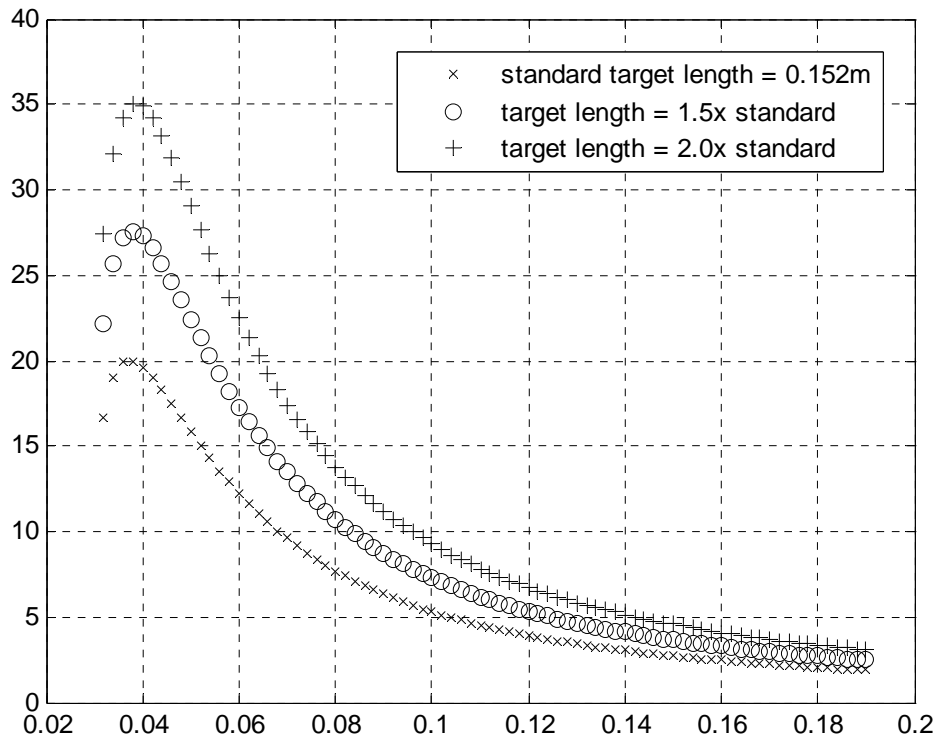


Figure 7.10 Effect of target length on the rate of heat transfer with varying channel diameter.

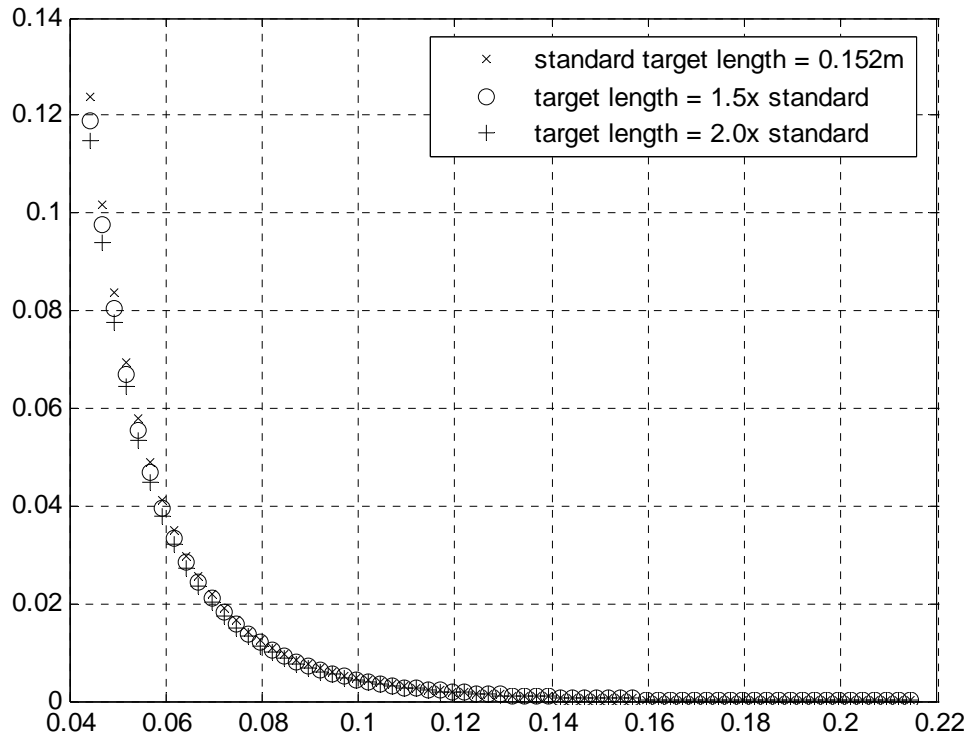


Figure 7.11 Effect of target length on the hydrodynamic resistor ratio.

While an increased target length will always increase the heat transfer, a similar effect is not seen with variations of the target diameter. Figures 7.12 and 7.13 display the heat transfer rates for multiple outer diameters of the target. Figure 7.12 uses the drain diameter currently used in the reactor, while Fig. 7.13 looks at an arbitrarily chosen larger drain diameter. The general shape of the heat transfer curves is similar for all target diameters, but the larger target diameters require a higher channel diameter to reach their peaks. Additionally, the maximum heat transfer rates differ as the drain diameter changes. The reason for this is because the drain diameter is choking the flow. As the drain opens up, more flow is allowed to pass through the system, and the heat transfer rates universally increase.

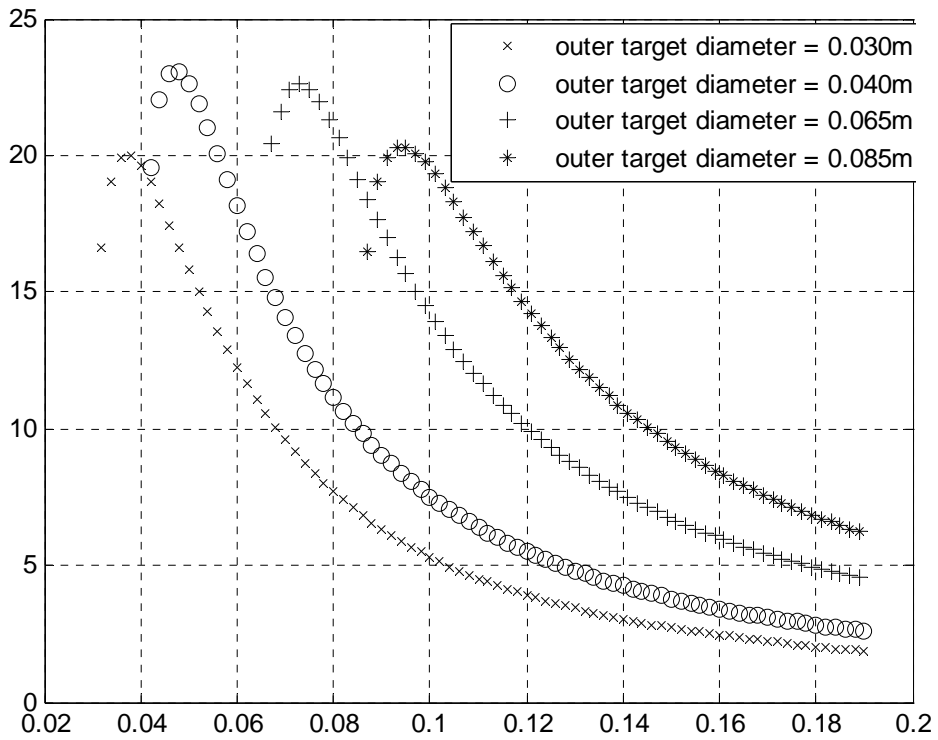


Figure 7.12 Total heat transfer vs. channel diameter for multiple outer diameters of the target. Drain = 0.04445m.

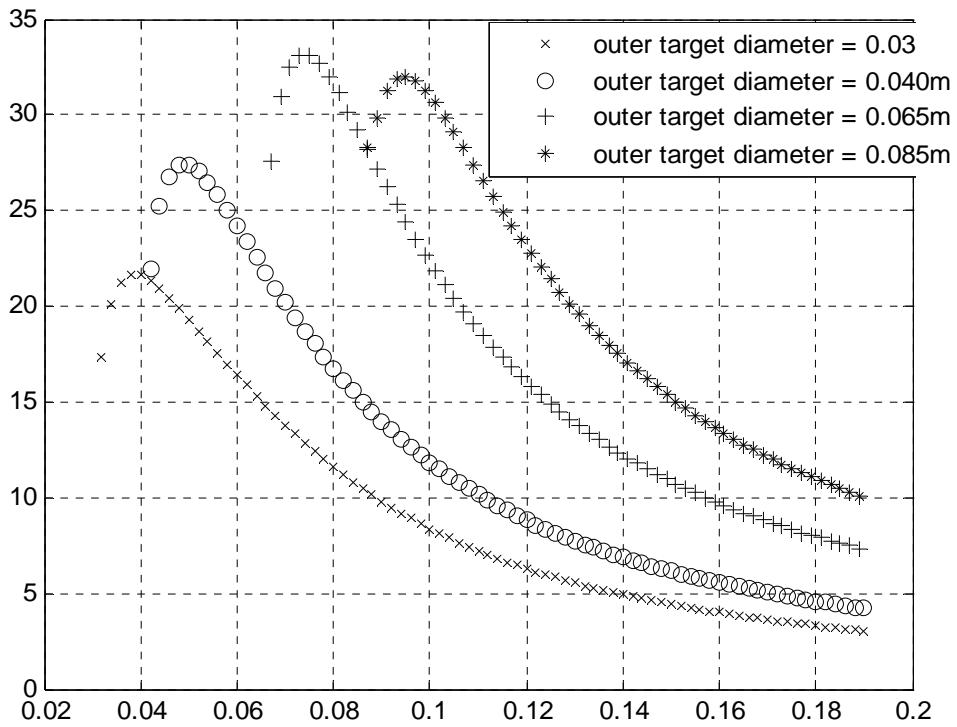


Figure 7.13 Total heat transfer vs. channel diameter for multiple outer diameters of the target. Drain = 0.060m.

7.1.5 Saturation Temperature

Throughout this thesis, the maximum temperature allowed by the safety regulations was treated to be 373 K, the saturation temperature of water at atmospheric pressure. As the target is under many meters of water, the actual pressure is much higher than atmospheric, making the saturation temperature about 13 K higher. While this was intentionally left as a factor of safety, it is useful to examine the difference this can make in the heat transfer.

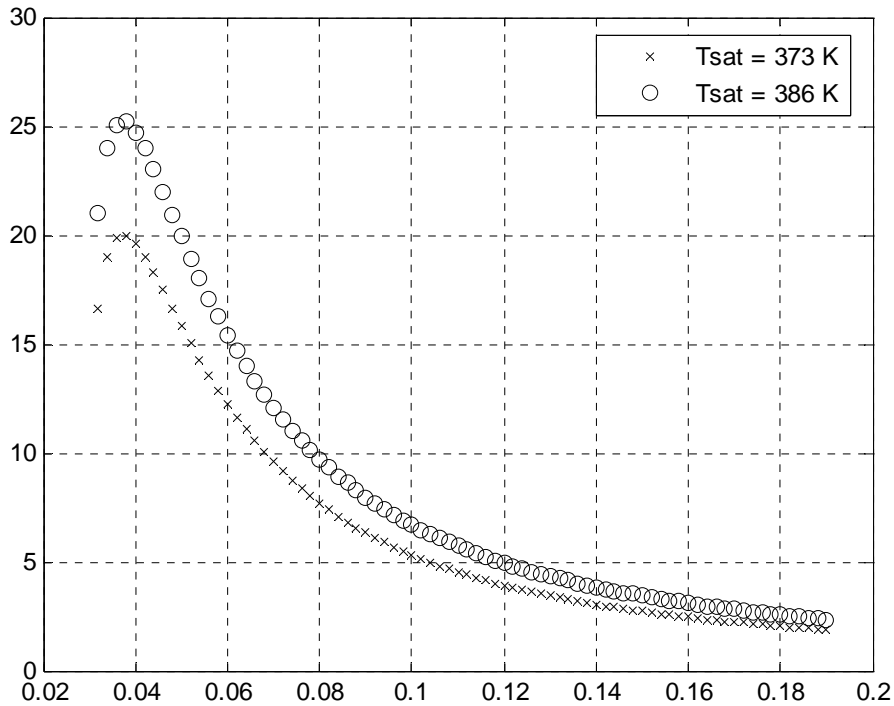


Figure 7.14 Effect of saturation temperature on the heat transfer with varying channel diameter.

As the driving force in the thermal model is defined as the difference between the saturation temperature and the initial water temperature, an increased saturation temperature would infer a larger thermal flow, or heat transfer. Figures 7.14 and 7.15 affirm this. The heat transfer curves for the increased saturation temperature share

identical trends to those of the 373 K saturation temperature, with the values being elevated by roughly 25%.

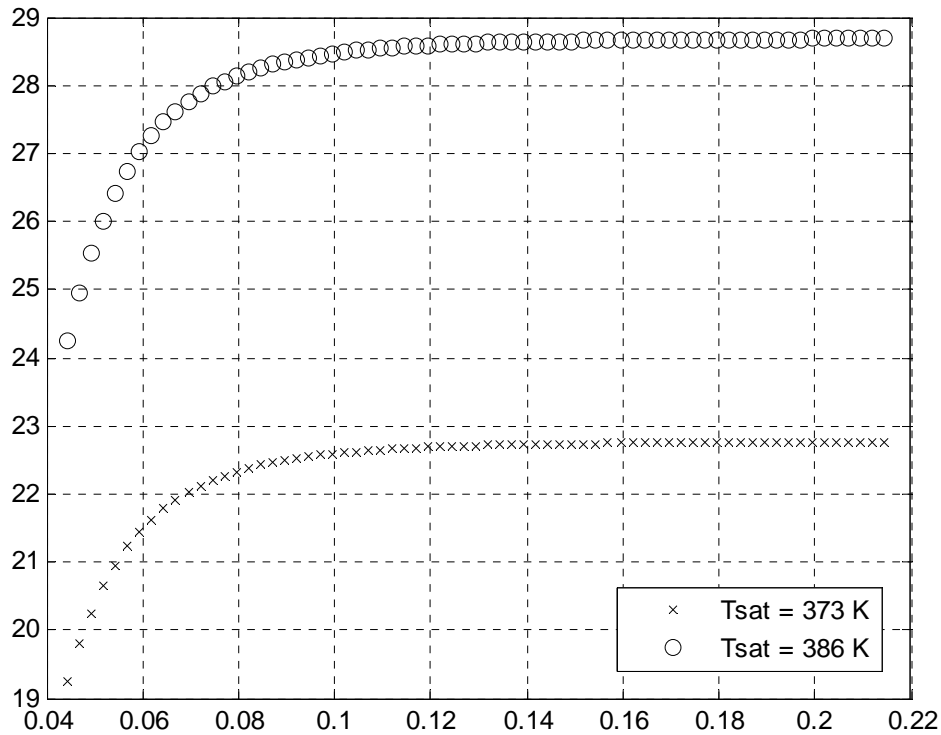


Figure 7.15 Effect of saturation temperature on the heat transfer with varying drain diameter.

7.2 Multiple Channel Results

While the heat transfer for a single channel has been maximized, this solution only uses a small amount of the wedge that can be used for high volume production. In addition to the parameters examined in the single channel analysis, a full optimization here also looks to use many parallel flow channels to maximize the heat transfer from the wedge.

7.2.1 Analytic Model Validation

Like the single channel model, before any data can be extracted from the analytic model, it is first compared to a numeric equivalent. Unfortunately, the numeric model for the multiple channel system is significantly more complicated than that of the single channel. Where the single channel model was able to be created as a 2-dimensional

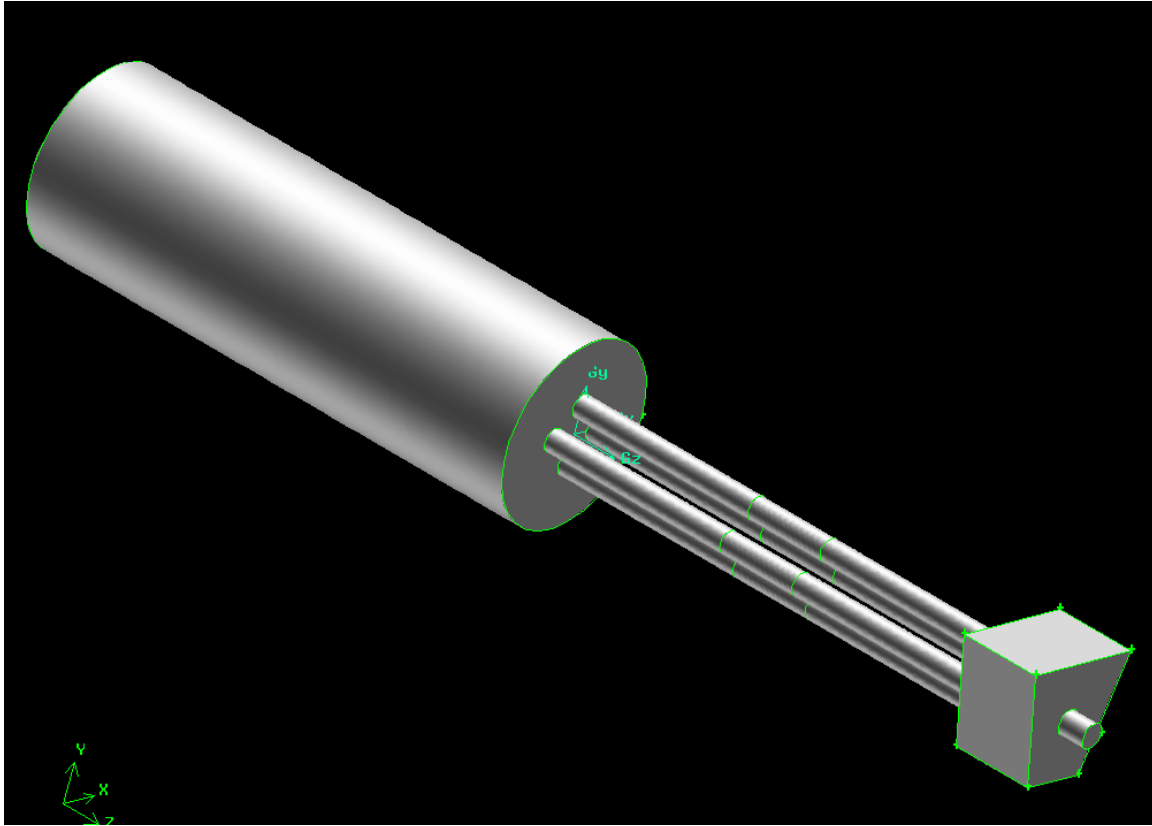


Figure 7.16 Diagram of the numeric 3-dimensional model used to confirm the analytic model.

drawing rotated about an axis (2-D axisymmetric representation), there is no way to do this with a multiple channel system. Instead, the multiple channel model is a purely 3-dimensional model containing four parallel flow channels, each containing an annular cylinder target. A picture of the model is displayed in Fig. 7.16. The simulation that is run for this model utilizes the same hydrodynamic and thermal boundary conditions established in Chapter 3. The results for the numeric and equivalent analytic simulation

are displayed in Table 7.5. The error assumes the numeric simulation provides the correct result.

Table 7.5 Comparison of the numeric and analytic data from a multiple channel simulation.

	Numeric	Analytic	Error
\dot{m}_{total} (kg/s)	5.165	5.074	1.8%
q_{total} (kW)	38.948	37.540	3.6%

While the obtained results show only a minimal difference between numeric and analytic results, more numeric simulations could be run under different boundary conditions and geometries to further establish the validity of the analytic model.

7.2.2 Optimization

Maximizing the heat transfer from an entire wedge requires an understanding not only of the trends caused by the channel diameter and drain diameter, but also of those caused by many channels in parallel. Figure 7.17 looks at the total heat transfer resulting from multiple parallel flow channels for the existing drain diameter. As the channel diameter increases, fewer channels are able to fit into the wedge. Unsurprisingly, an increase in the number of channels increases the total heat transfer of the system. The plot does reveal a diminishing return trend, as each added channel contributes less heat transfer than the previous. This is clearly displayed when the heat transfer is examined on a per channel basis in Fig. 7.18. As more channels are added, the total mass flow through the system increases, but the amount seen by each channel decreases. Moreover, since the drain diameter is being held at a small value, the flow quickly becomes choked, as confirmed by Fig. 7.19.

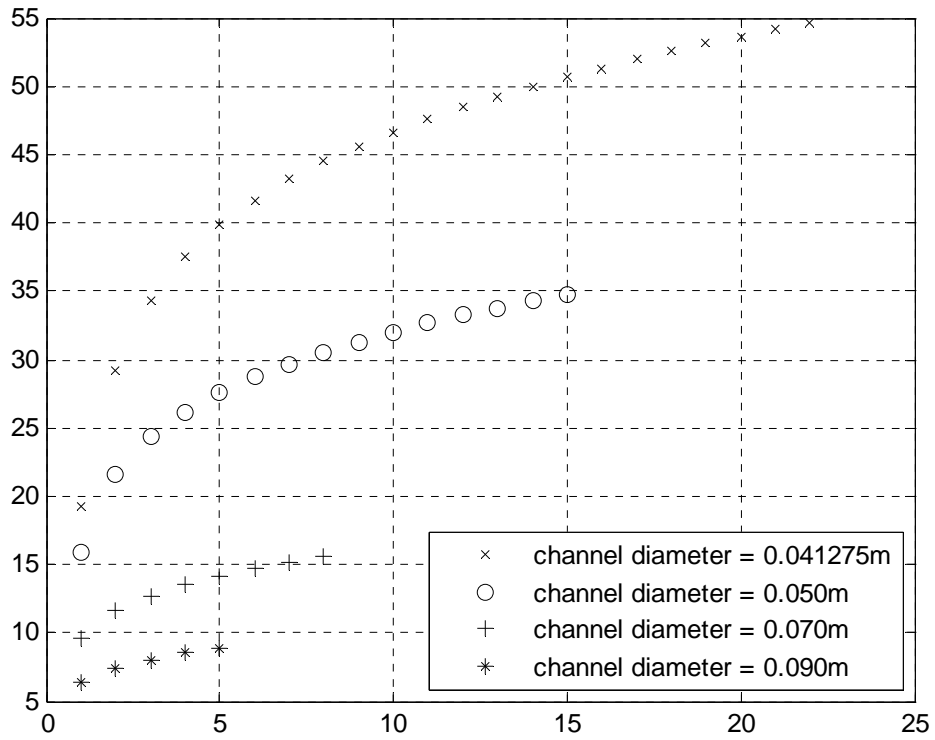


Figure 7.17 Total heat transfer vs. number of channels using the existing drain diameter.

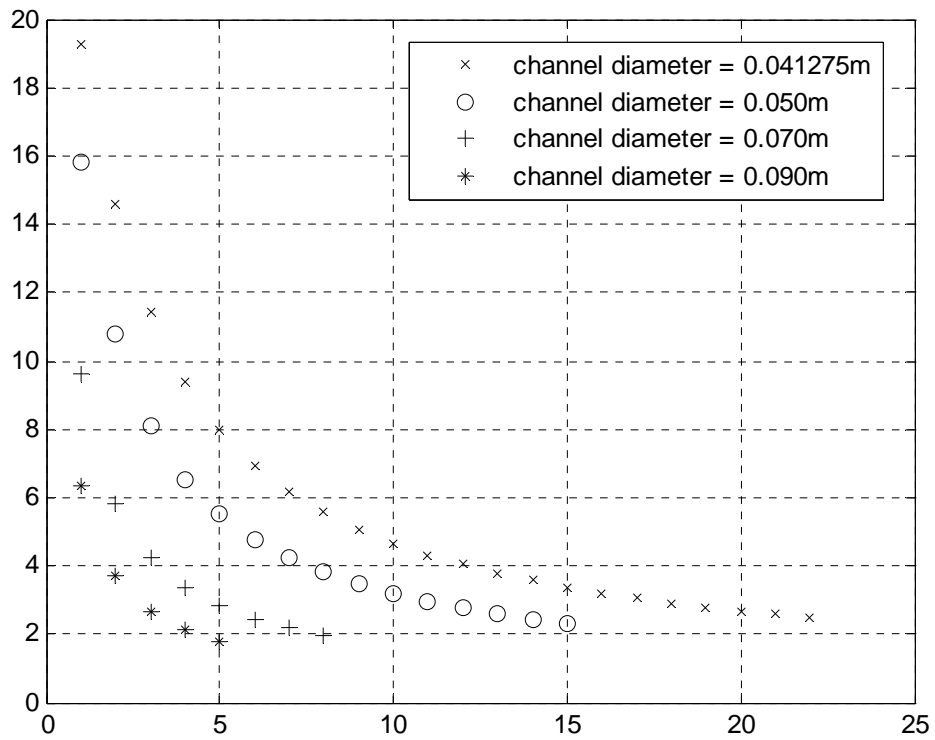


Figure 7.18 Heat transfer per channel vs. number of channels using the existing drain diameter.

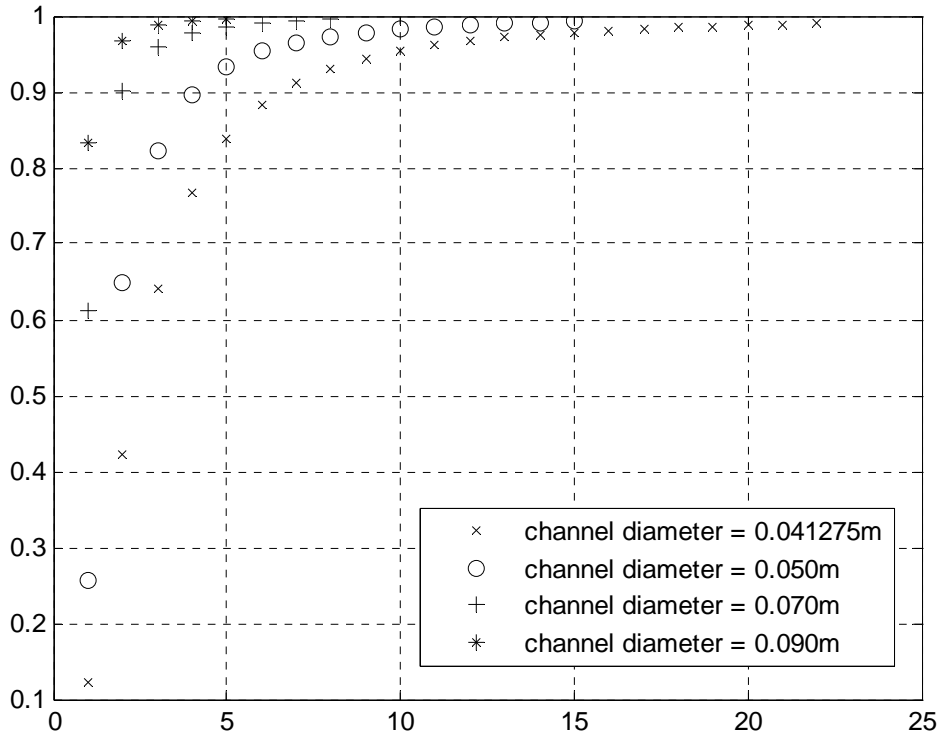


Figure 7.19 Resistor ratio vs. number of channels for the existing drain diameter.

To show the potential increase in heat transfer, the channel diameter is fixed and a few different values of the drain diameter are examined in Fig. 7.20. Each of the curves shows a period of near-linear increase in the heat transfer with respect to the number of channels. As the drain diameter increases, this linear regime remains for more channels before beginning to drop off, thus resulting in a higher heat transfer. Again, looking at the plot of the ratio of the exit resistance to the total resistance, it is clear why this behavior exists. In Fig. 7.21, for the existing drain diameter, a large majority of the resistance is generated across the drain when there are five channels in parallel, and this only increases with more channels. As the drain expands to 2x and 3x the original diameter, the drain has less of an effect on the flow, and most of the resistance occurs inside the channel.

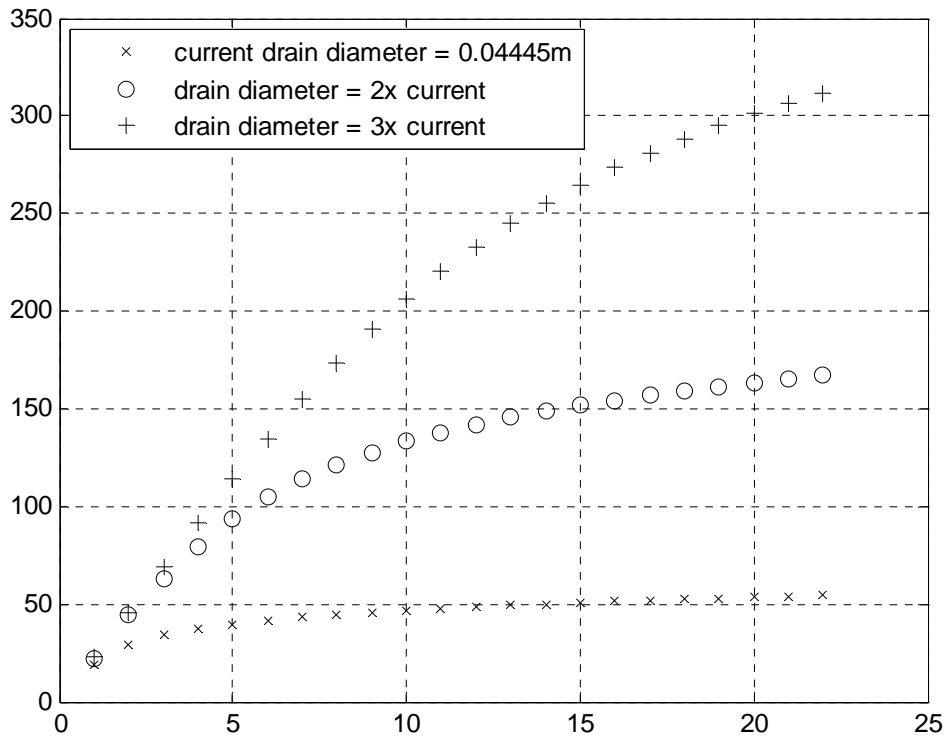


Figure 7.20 Total heat transfer vs. number of channels for the existing channel diameter.

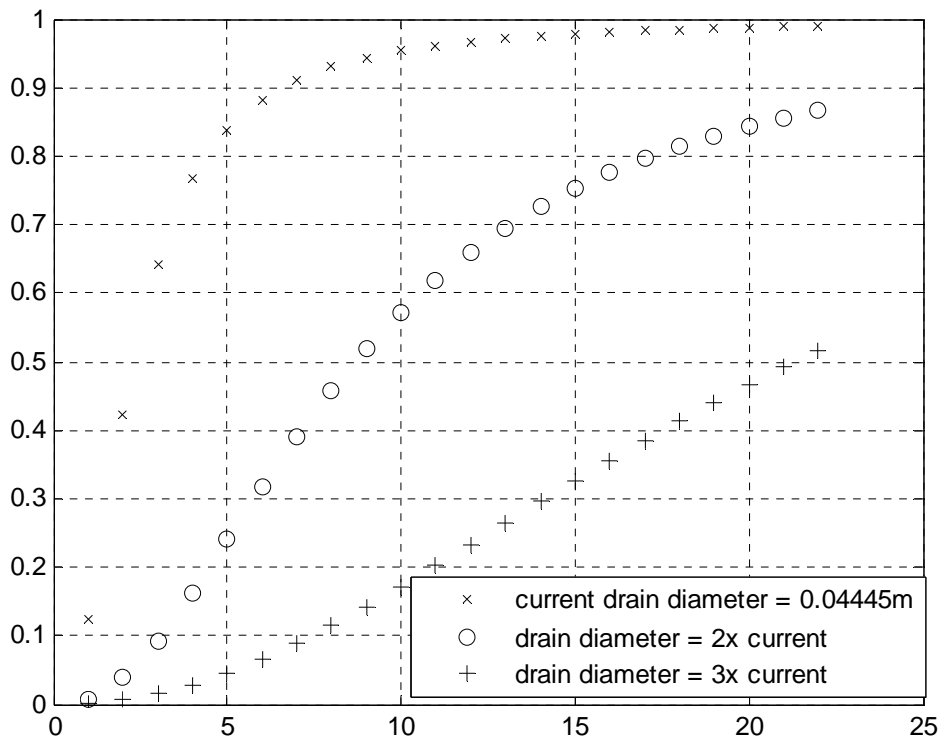


Figure 7.21 Resistor ratio vs. number of channels for existing channel diameter.

With the importance of the drain diameter established, the next step is to examine the changes caused by the channel diameter. If the total heat transfer is plotted against the channel diameter for a fixed drain diameter, as in Figs. 7.22 and 7.23, a trend quickly arises. Regardless of the number of channels, the maximum heat transfer is reached

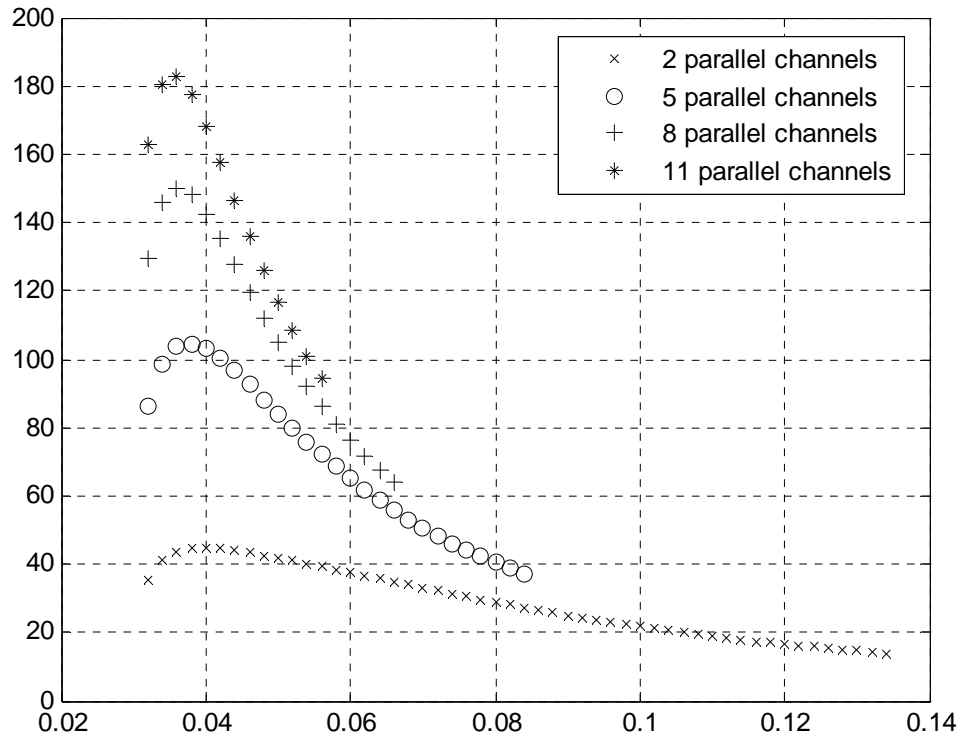


Figure 7.22 Total heat transfer vs. channel diameter for multiple channels. Drain = 0.100 m.

between a channel diameter of 0.035 m and 0.050 m. As the number of channels increases, the optimal point occurs at smaller channel diameters. This is a result of the system trying to match total flow areas in the channels and drain. However, at a certain point, the channel encroaches too near the target. Consequently, the annular flow becomes severely restricted, and the heat transfer suffers. As the drain diameter increases, the maximum total heat transfer possible increases greatly. The optimal channel diameter that results in the maximum also slightly increases as the drain increases.

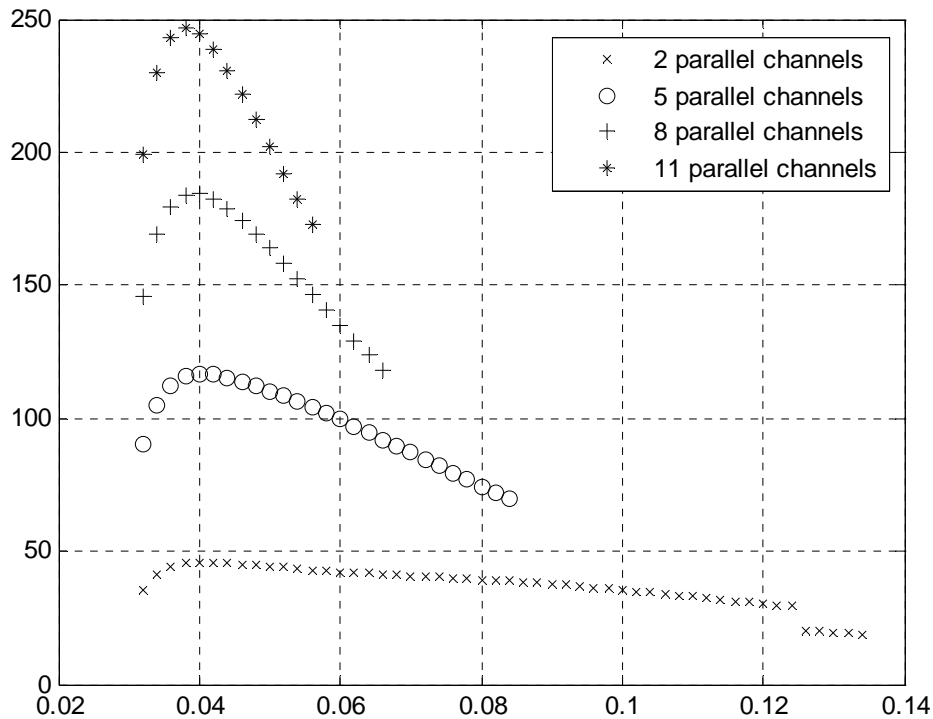


Figure 7.23 Total heat transfer vs. channel diameter for multiple channels. Drain = 0.150 m.

An interesting result of the data from Figs. 7.22 and 7.23 is seen when the heat transfer per channel is studied. The heat transfer per channel in Fig. 7.24 is always greater for a smaller number of parallel channels at a given channel diameter. In Fig. 7.25, the heat transfer per channel is greater for 5 parallel channels than for 2 while the channel diameter is less than 0.050 m. Together, these plots collectively demonstrate that for drain diameters above a certain value, the heat transfer per channel can actually increase as the number of channels increases, thus reaffirming the importance of a large drain diameter. A clearer picture of this arises when the heat transfer per channel is plotted against the drain diameter for a specified channel diameter, as in Fig. 7.26.

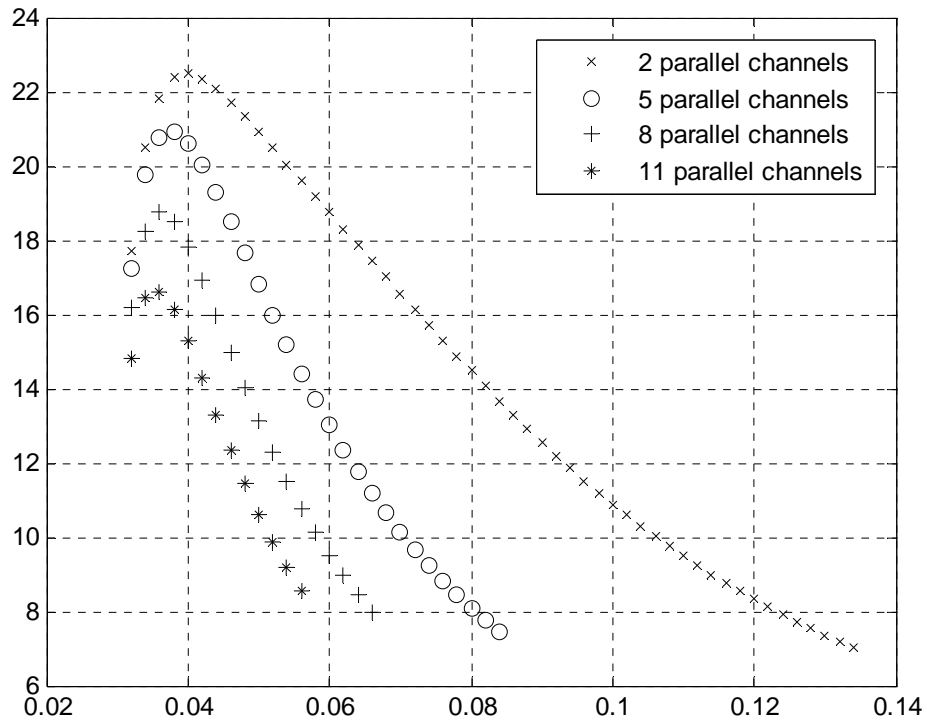


Figure 7.24 Heat transfer per channel vs. channel diameter for multiple channels. Drain = 0.100 m.

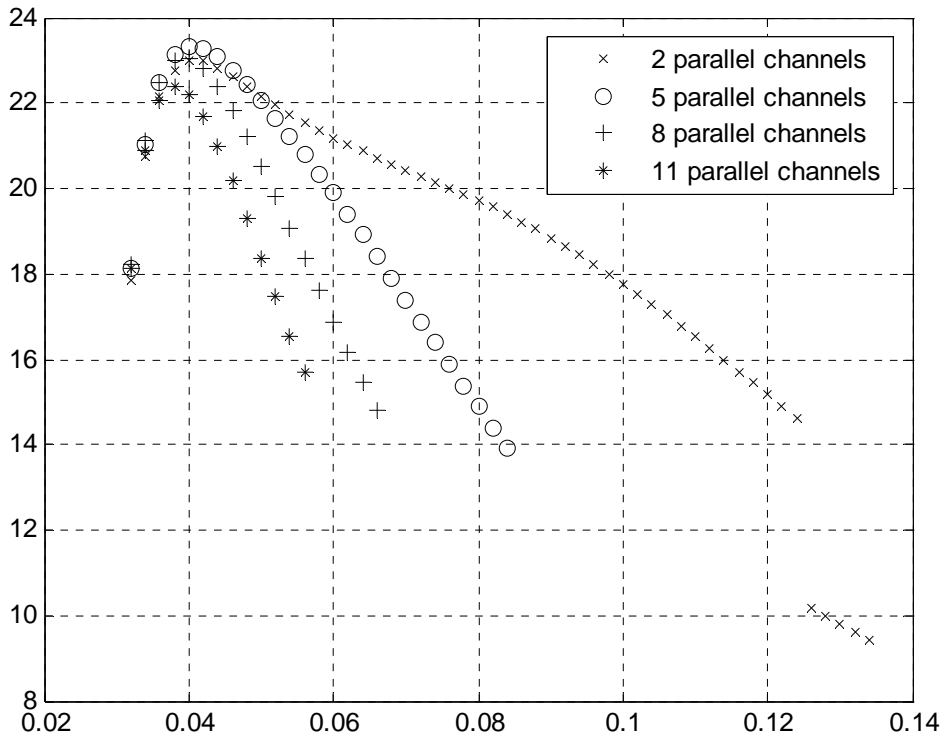


Figure 7.25 Heat transfer per channel vs. channel diameter for multiple channels. Drain = 0.150 m.

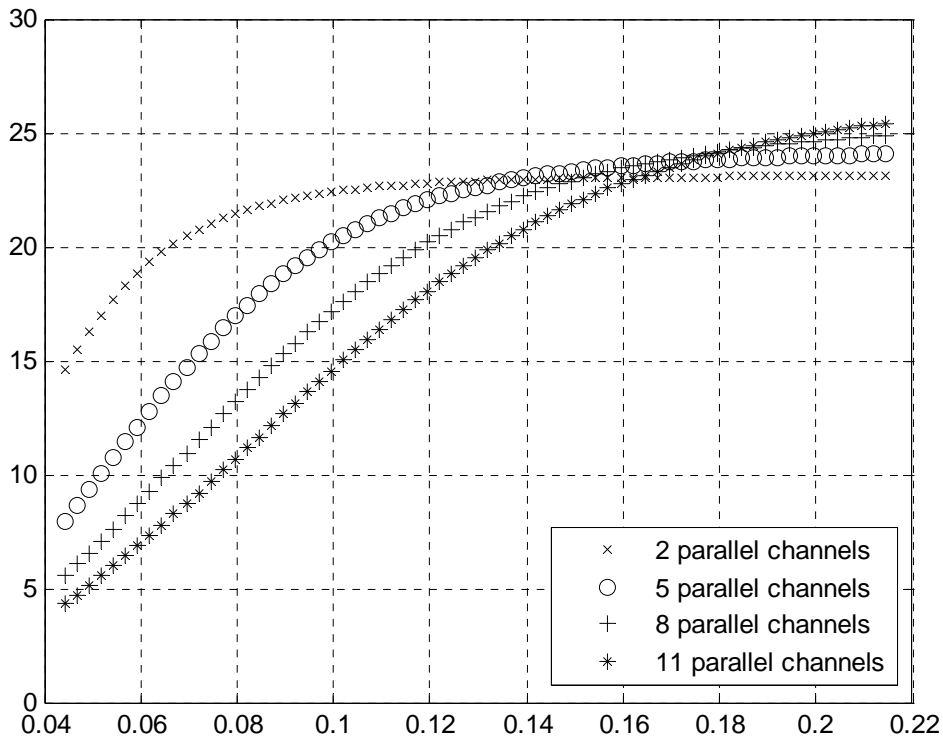


Figure 7.26 Heat transfer per channel vs. drain diameter for multiple channels.

This result seems counterintuitive until the hydrodynamic model is revisited. In this model, there were two main contractions and one main expansion. (The expansions and contractions around the targets are much smaller.) One of these contractions is into the drain. As the drain is expanded, this contraction disappears, causing the heat transfer to increase. The expansion occurs when the coolant leaves the channel and flows into a common area prior to the drain. As the number of channels, and hence total channel flow area, increases, this expansion disappears as well. Because of this, models with a larger number of channels are able to support a higher heat transfer per channel, as long as the drain is not significantly choking the flow.

In summary, the maximum heat transfer exists when the drain is eliminated. The optimal channel diameter ranges between 0.035 m and 0.050 m and varies depending on

the number of parallel channels in the system. To give a concrete example of these effects, Fig. 7.17 is once again referenced. It is seen that if the channel and drain diameters are left as the existing dimensions, the maximum rate of heat transfer from 10 parallel channels is approximately 47 kW. If the drain is removed entirely and the channel diameter is slightly expanded to 0.0435 m, the analytic model predicts that the maximum heat transfer jumps to 253.16 kW. This translates to more than a 400% increase in production.

7.2.3 Plate Targets

Recently, the topic of flat plate targets has resurfaced, with a desire to compare their performance against the annular cylinder targets. From neutronics calculations, it was found that three channels, each containing eight plate targets, would achieve enough neutron flux to produce a sufficient fission rate. In each channel, the eight plates would be arranged in two square configurations, with the second being located directly downstream from the first. A diagram of the setup is displayed in Fig. 7.27. To assimilate this target arrangement into the existing analytic model, the square configuration is approximated as an annular cylinder with an equivalent surface area. As the dimensions of the foil inside each plate are 24mm x 230mm, the outer diameter of an equivalent annular cylinder is 0.032m. Although the value of this is similar to that of the actual annular cylinder target, the length of the plates is significantly longer.

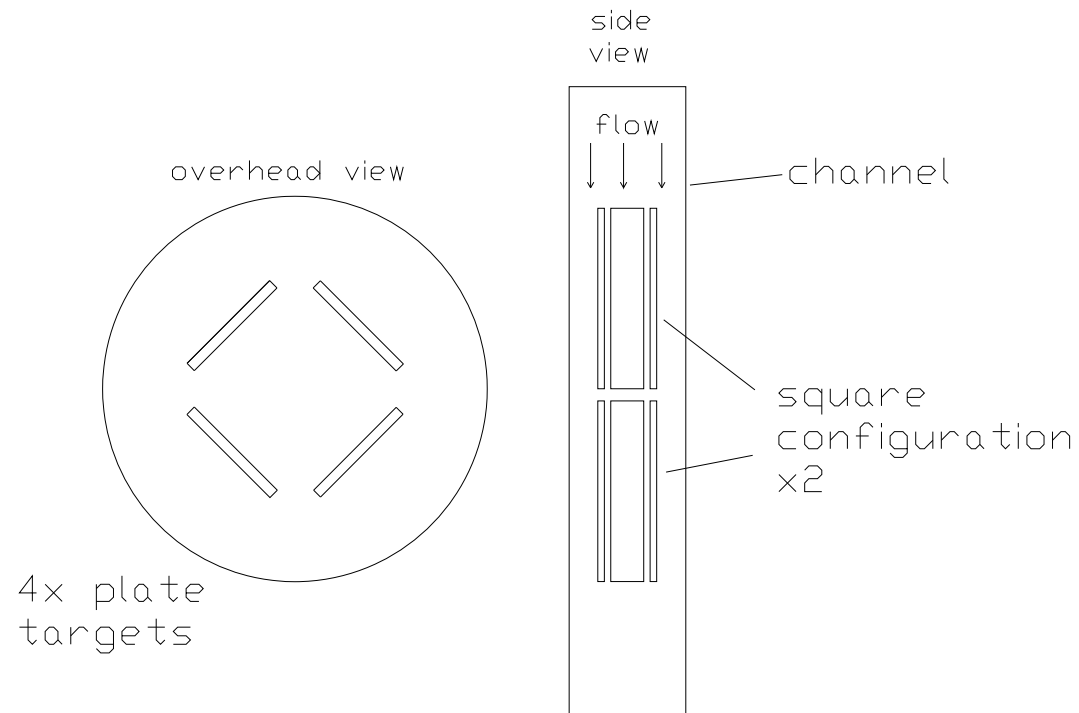


Figure 7.27 Diagram of in-channel plate target configuration.

To find the geometric values that result in the maximum heat transfer from the targets, the effect of the drain diameter is first examined. A plot containing the heat transfer curves for a few different channel diameters is shown in Fig. 7.28. Like all models previous, the heat transfer increases as the drain diameter increases, without exception. As the highest heat transfer is seen for a channel diameter that is neither the highest nor lowest plotted, Fig. 7.28 also displays that an optimal channel diameter does exist.

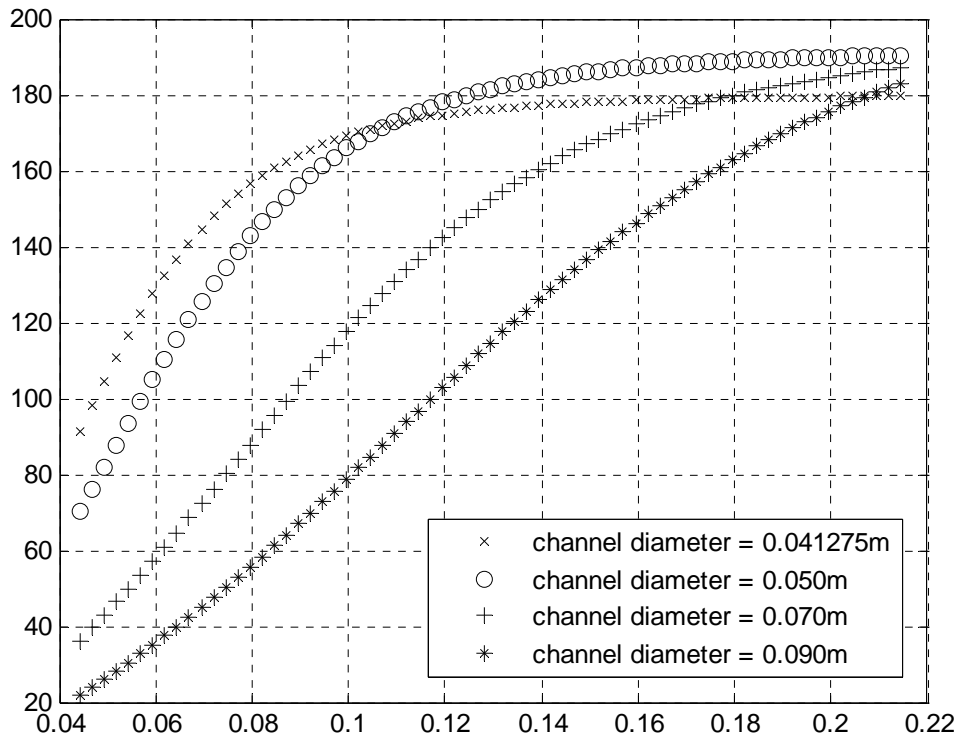


Figure 7.28 Total heat transfer vs. drain diameter for plate target model.

To find this optimal value, the channel diameter is iterated upon for four different values of the drain diameter, featured in Fig. 7.29. As suspected, the largest drain diameter results in the largest heat transfer rate. From this graph, the maximum rate of heat transfer is found to be 190.34 kW, occurring at a channel diameter of 0.0515 m. If the drain is unable to be completely eliminated, a majority of the heat transfer can still be retained as long as the drain can be opened to a diameter of 0.150 m. In this case, a heat transfer rate of 186.12 kW is possible when the channel diameter is fixed at a value of 0.0485 m.

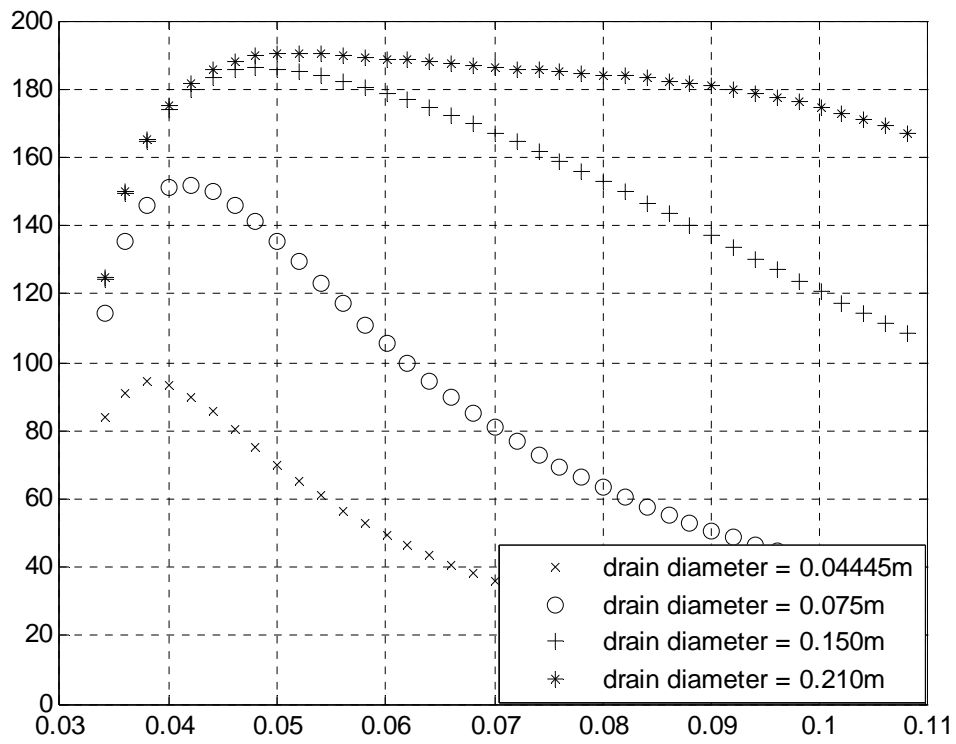


Figure 7.29 Total heat transfer vs. channel diameter for plate target model.

Chapter 8

CONCLUSIONS

After examination of the current reactor geometry, as well as improvements that can be made to improve the heat transfer rate and increase production of molybdenum-99, it is recommended that the current reactor configuration should be altered in favor of multiple parallel flow channels.

The current wedge geometry for a single channel provides a heat transfer rate of 19.18 kW. This is relatively near the optimum, though it can be increased to 22.77 kW by decreasing the flow channel diameter to 0.0405 m and eliminating the constriction of the drain. As heat transfer rate is directly related to molybdenum-99 production, this is an 18.7% potential increase in production.

The inclusion of multiple channels into the model significantly increases the heat transfer from the target. If the drain and channel diameters are left at their current values of 0.04445 m and 0.041275 m, respectively, 10 parallel channels will result in a heat transfer of approximately 47 kW. If the drain is removed and the channel diameter is slightly expanded to 0.0435 m, the heat transfer rate for these same 10 channels jumps to 253.16 kW. Consequently, when multiple parallel channels are used, it is imperative that the drain diameter is increased, if not removed altogether. Also, increasing the number of parallel channels always increases the total heat transfer. The increase in heat transfer

with the addition of more channels will be diminished as the sum of the channel area approaches the drain area.

The maximum heat transfer from a configuration of plate targets as described in Section 7.2.3 is 190.34 kW. This is accomplished when the channel diameter is 0.0515 m and the drain is fully opened. As long as the drain can be opened to at least a diameter of 0.150 m, 97.8% of the maximum heat transfer rate can be achieved. In this situation, the channel diameter has to decrease in size to minimize choking of the flow.

Chapter 9 RECOMMENDATIONS

9.1 Enhanced Cylinder Geometry

The research detailed in this report focuses primarily on examining two main factors: the number of channels present in the wedge and the diameter of those channels. While these two parameters are enough to generate rudimentary trends for optimization, there exist a number of additional studies that could have been performed to further approach a truly optimal design.

One notable possibility that is not thoroughly examined is the alteration of the annular cylinder geometry. In order to ensure simplicity in the manufacturing process, all dimensions of the target remained fixed; however, their values are not necessarily ideal in their current state. This can easily be demonstrated by looking at a temperature profile of the water as it passes around the heated annular cylinder. As seen in Fig. 9.1, the thermal

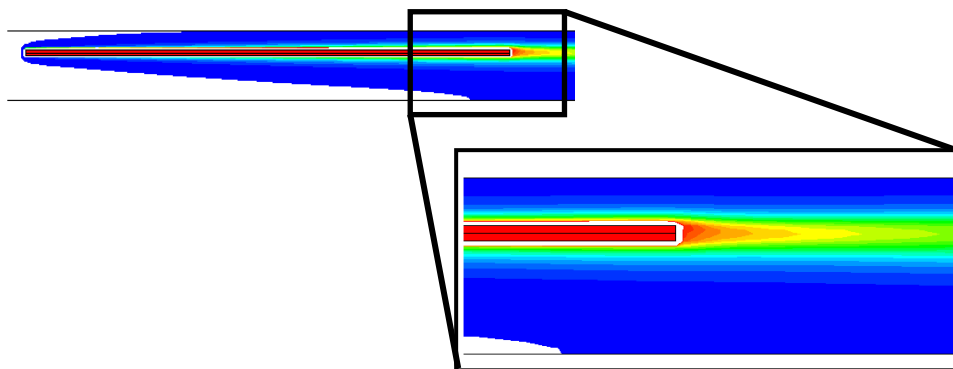


Figure 9.1 Temperature contour around heated annular cylinder

boundary layer around the annular cylinder is very thin. It is not much wider than the target itself. This is reiterated in Fig. 9.2, a plot of the temperatures across the channel at

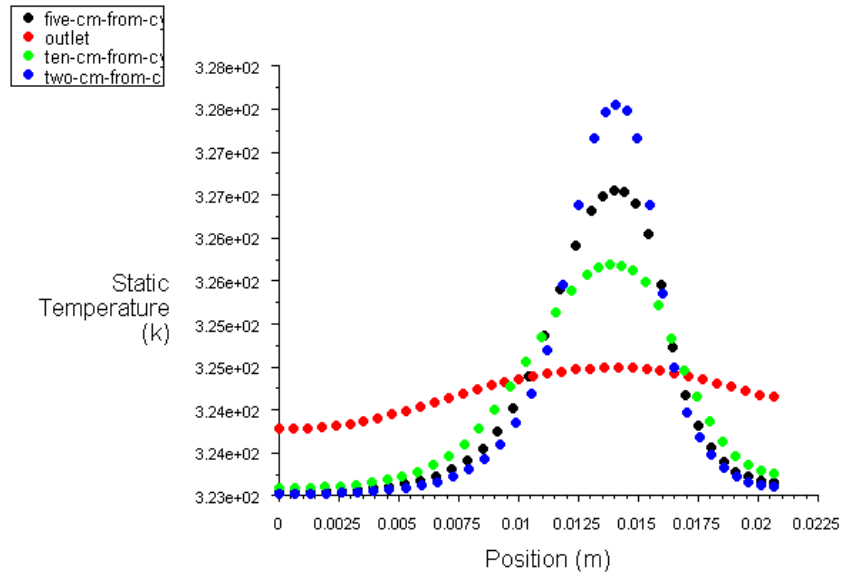


Figure 9.2 Temperature distribution of the flow at varying downstream distances from the annular cylinder

different lengths downstream. At two centimeters past the heated target, much of the water in the channel feels only a very slight increase in temperature. Even at ten centimeters, this is still the case, meaning there is a severe lack of mixing in the flow.

While a lack of mixing does not intrinsically mean there is a problem, it does show that the heat transfer is not as effective as it could be. All heat transfer works off a temperature difference. The larger the temperature difference is between two items, the more heat there will be transferred from one to the other. If the water mixes as it flows past the heated annular cylinder, the temperature distribution would look more like that of the outlet profile than of the two, five, or ten centimeter profiles. This means that the water adjacent to the annulus would be cooler, as it will have dispersed its heat to other parts of the flow. Then, with a colder flow near the annular cylinder, there would be a larger temperature difference and more heat transferred.

There are many ways to achieve a mixed flow by altering the geometry of the target. Entire books and papers are written on the subject (Raza and Kim, 2008). Most involve adding extended surfaces such as pins, fins, or ridges to the surface, but some involve changing the shape of the annular cylinder itself. While almost all of these will increase the heat transfer coefficient, they will also increase the pressure drop across the target. This will lead to a decreased mass flow rate, canceling some of the positive impact of the increased heat transfer coefficient. It is a trade-off that must be watched, but somewhere within the hundreds of ideas that have been proposed, an optimal solution does exist.

9.2 Utilization of Surroundings

All of the models, numeric and analytic, presented in this report describe the heated annular cylinder as floating in the channel of its own accord, but this must obviously omit some part of reality. The actual setup requires the use of a holder, displayed with the cylinder in Fig. 9.3. Currently, the holder exists only as means by which to support the target as it is irradiated, with the bulk of the holder being located downstream. As such, it causes no significant change in the flow as it passes over the annular cylinder, with the exception of an increased pressure drop. This increased pressure drop will translate to a decreased mass flow rate, and without any increase in heat transfer coefficient to compensate, the result will be an overall decrease in total heat transferred.

While the holder may appear to pose a problem, it actually presents an interesting engineering design opportunity. By making some adjustments to the geometry of the

holder, one could alter the flow profile ahead of the annular cylinder. Any additional turbulence that could be caused prior to or around the cylinder would increase the heat transfer coefficient, leading to better performance. This could possibly be accomplished by attaching a coiled wire or turbine blades to the holder just in front of the target. Therefore, even though the added pressure drop would still exist across the holder, the added turbulence would increase the heat transfer coefficient, potentially leading to a greater amount of heat transferred.

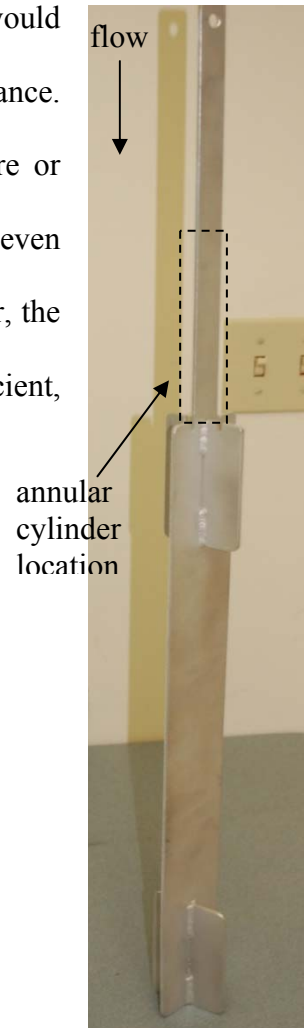


Figure 9.3 Picture of target holder

Appendix A

FLUENT TUTORIAL

Throughout the research presented in this report, FLUENT is repeatedly mentioned as the program in which numeric simulations are performed. While FLUENT does in fact solve the flow and temperature fields to obtain all the hydrodynamic and thermal properties, it is not the only computer program utilized. As with any numeric simulation, a general series of steps is followed. First, all of the setup geometry is created in Gambit. Next, this geometry is meshed, also done in Gambit. Meshing consists of breaking up the geometry into thousands or even millions of pieces. Essentially, each of these pieces is considered a differential element, for which a continuity equation and energy balance are applied. The geometry and mesh are then imported into the solver program, FLUENT, where an initial guess for the flow and temperature fields is iterated upon until the system of equations converges on a single solution. In order to replicate or expand on the results presented in this report, giving directions for the entire process is thought to be warranted.

In order to form the geometry that would be meshed and solved, it first has to be decided exactly how the geometry is to be represented. While all of the sub-problems in this project can certainly be solved by creating a 3-dimensional model, this analysis in FLUENT can take a day or more to converge, depending on the number of cells in the mesh. To combat this extended solving time, the earlier models can be reduced. This is

done by forcing the 3-dimensional model to become a 2-dimensional axisymmetric one. This means that a 2-D section of the model is created and then rotated about some axis to form the final 3-D model. This greatly reduces computation time because the rotation around the axis does not really occur. Instead, FLUENT understands what the axis means

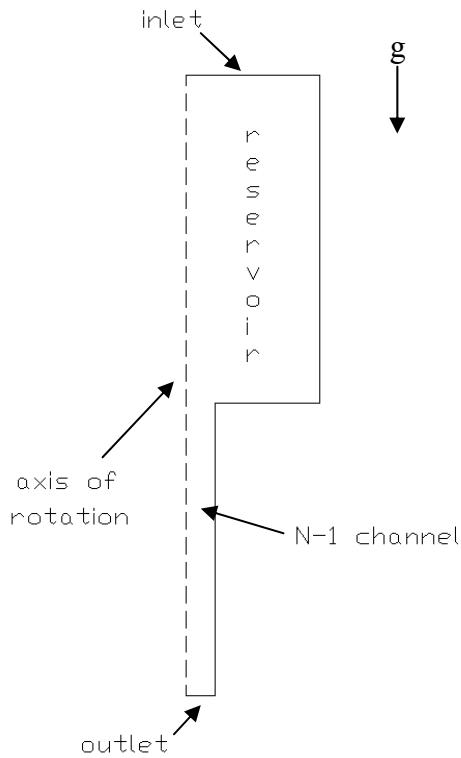


Figure A.1 A 2-D axis-symmetric diagram of the reservoir with an empty N-1 channel

and solves the simulation for only one unit angle of rotation, as compared to all 360°. The 2-D section is exhibited in Fig. A.1, and the reduction displayed is possible for a few reasons. First, the N-1 channel is a cylinder with a radius that is independent of the angle of rotation. The anemometer probe and holder, as well as the aluminum cylinder, are also symmetric in the angular dimension, though these may or may not be present depending on which of the three models is being simulated.

Secondly, since the N-6 channel is plugged up during all operation for this project, it is assumed that all the water around the test wedge is flowing through the N-1 channel. In terms of the model, this becomes the justification for the reservoir. Because of the isolation of the N-1 channel, it is known that the size and shape of the reservoir are not critical to the flow, as long as the reservoir encapsulates all inlet effects that occur due to the transition from the reservoir to the N-1 channel. Also, it is necessary that the cross-sectional area of the reservoir is made large enough that the frictional losses and pressure drop across the

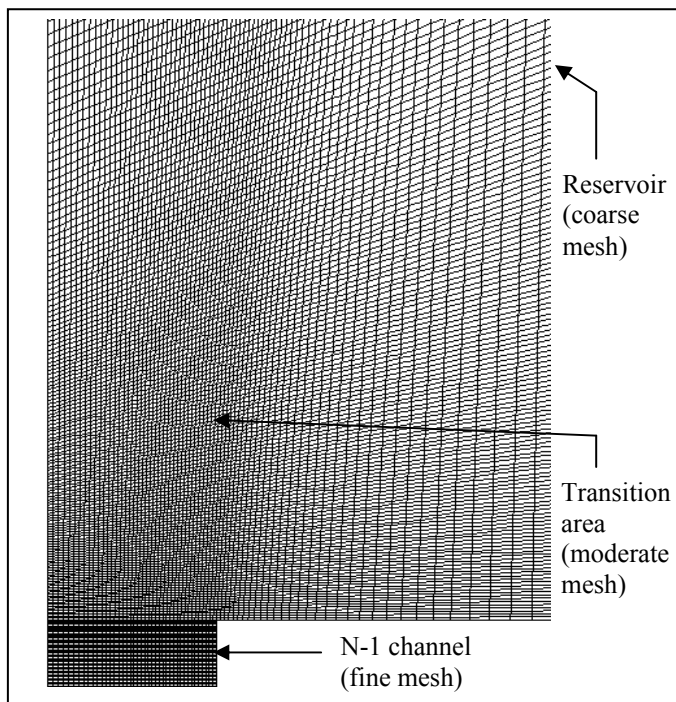
reservoir itself can be ignored. In the end, the reservoir is chosen to be a cylinder with a cross section that is 8x the diameter of the channel. The shape is picked to allow the axisymmetric analysis, but the diameter can only be picked arbitrarily and then confirmed post-selection as fitting both criteria through trial and error. It should also be mentioned at this point that a 2-D axisymmetric simulation is only possible for single channel analyses. When the topic of discussion shifts to optimization through use of multiple channels, this simplification will no longer be available.

Once the representation is established, the actual creation of the geometry in Gambit is straightforward. There is one thing that should be noted, though. If the surfaces are formed by joining separate shapes, such as rectangles, Gambit will not recognize the geometry as connected unless it is forced to do so. This can be accomplished by “splitting” the surfaces together. This is especially important in the models that have smaller geometry elements fully contained by larger ones. An example of this is seen in the third model type, displayed in Fig. 3.2 in Chapter 3. When the rectangle that represents the cylinder is created in the N-1 channel, initially, Gambit will see one setup of an empty N-1 channel and then a separate setup that only involves the rectangle. Until they are forced into the same setup using the “split” function, the two entities will not “see” each other.

With the physical geometry of the model in place, the final step before analysis is meshing. Unfortunately, this is the least-established step in the entire process. There is no step-by-step formula that can be taken to arrive at the perfect mesh; however, there are a few general principles that should be adhered to. The first of these simply consists of knowing what the mesh actually means and how it will work in FLUENT. As stated

before, each cell in the mesh means the application of the continuity and energy equation once in that volume per iteration. (All cells have volume, even in 2-D and 2-D axisymmetric simulations. In these two, there is an implied unit depth or unit rotation angle. This is important to remember when examining properties which are based off unit depth or rotation angle, such as the Reynolds number.) Therefore, it can be deduced that, in general, a more dense mesh will have a higher accuracy than a coarse one. But this improvement does not come without a price. Logically, while more cells mean a greater accuracy, it also means more equations to be solved, and hence a longer computation time. Fortunately, the mesh does not have to be uniform over the entire model. Critical areas can be made to have a dense

mesh, while areas of little activity can afford to have a coarse mesh. An example of this is given in Fig. A.2. The most reliable way to go about making a selectively dense mesh is to build the mesh from scratch as much as possible. Ideally, this would involve placing each node, or mesh point,



manually along the edge of a **Figure A.2 Demonstration of coarse and fine meshes** geometry, forming an edge mesh out of a sequence of nodes, and then forming the surface mesh out of a sequence of edge meshes. Practically, though, placing each node takes far too long. Therefore, the process can be sped up by using the built-in Gambit

function to generate edge meshes without first placing the nodes. When an edge mesh is created in this way, it defaults to a successive ratio type with a ratio of 1, meaning that the nodes along the line are equally spaced. A successive ratio greater than one translates to an increasing distance between the nodes, with the ratio specifying the fractional increase in the distance relative to the two previous nodes. Generally, the successive ratio type is not used unless the ratio is one, as the change in size is often too drastic. More commonly used types do include the first/last ratio and the exponent.

At this point, it should be mentioned that the edge meshes may not be able to be created independently of each other, depending on which of the two surface meshing schemes is employed. For a quad mesh, this is the case. Since it is composed completely of quadrilateral shapes, any edges that run parallel to each other must have the same number of nodes. If this is not the case, there will exist a location where there will not be four nodes. Consequently, a quadrilateral will not be able to be formed. Being constructed of triangles, the tri mesh does not face this same problem. The edge meshes can be designed with any number of nodes, without any regard to other edge meshes. Although it may only seem a matter of convenience, this does have a deeper impact when taking into account cell skew. Though it is not going to be covered in great depth here, there are a few things that should be known about skew. Briefly, it is a comparison of the angles in the cell. If the cell contains a large angle and a small angle, it is said to have a high skew. On the other hand, having exactly four right angles, a perfect rectangle has no skew. Very high skews (values between 0.9 and 1.0) cause errors in the equations applied to each of the cells, leading to convergence issues in FLUENT. To be on the safe side, it is recommended that the skew values be kept under 0.7 for all cells in the model, with at

least 75% of the total number of cells achieving a value under 0.15. While the factors up until now have an important impact on the surface mesh type chosen, there are still a few other ones considered. Because of the way the quadrilateral cells match up with each other to form what can essentially be thought of as rows and columns, the equations for a quad mesh are easier for FLUENT to solve than for a tri mesh. The final factor in deciding which surface mesh to use is the realization that they are not necessarily mutually exclusive. If the model benefits from it, both types can be implemented in

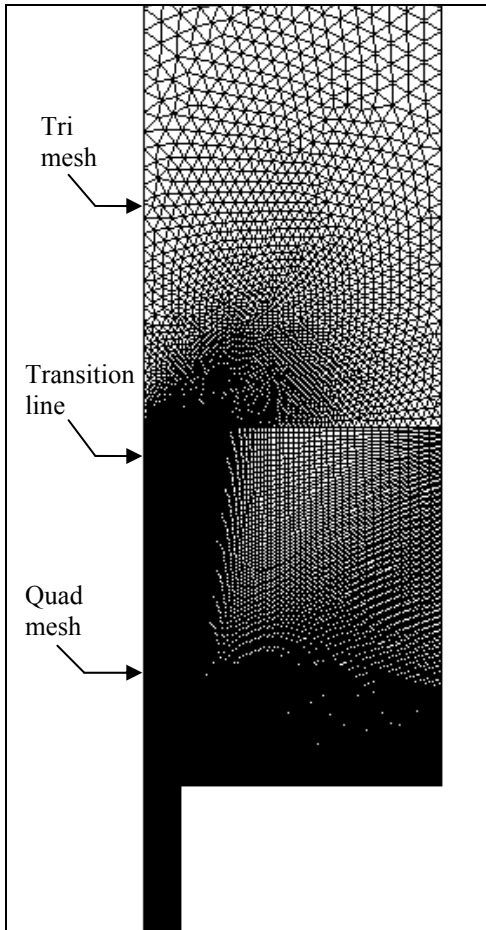


Figure A.3 Union of quad and tri meshes

different sections. Figure A.3 shows a location where this is done. A quad mesh is used near the entrance to the N-1 channel for accuracy, and a tri pattern is used in the rest of the reservoir to minimize cells in uneventful locations.

The alternative to this “bottom-up” method is simply to use the mesh surface command without meshing any of the edges. While it is certainly quicker, this strategy allows the user little control over where the mesh is dense and where it is coarse, most likely resulting in either accuracy or convergence issues once in FLUENT. Regardless of the method, the final step in Gambit is to export the model as an

“.msh” file so that it can be read into FLUENT.

After the desired mesh has been achieved, the model is finally ready to be imported into FLUENT. The first task that should always be performed when using FLUENT is to ensure the geometry and mesh are imported correctly. Fortunately, FLUENT has a built-in checker under the **Grid/Check** menu. While this allows FLUENT to complete numerous internal checks, there are two main pieces of information that are output upon the check. The first of these is the domain extent. As would be expected, the domain extents are the maximum and minimum x and y coordinate values for the geometry, i.e. the extent of the domain. (If the geometry was created in Gambit in some unit that was not meters, it can be adjusted in the **Grid/Scale...** menu.) Though it certainly does not guarantee that all of the geometry made the transfer from Gambit to FLUENT, it is a quick first step to finding if there is anything wrong with the geometry. A more detailed method would be to display the geometry under the **Display/Grid...** menu and do a piece-by-piece checklist for each of the features. The second value of interest that the check displays is the volume of the smallest cell in the entire mesh. If this number is negative, the meshing process did not entirely work, and FLUENT will not be able to begin a simulation. If both of these “tests” are passed, it is a good sign that no critical errors were made in Gambit.

Once it is confirmed that the model is as intended, specific values and solver options can start to be assigned, beginning with the solver. When starting FLUENT in the 2-dimensional double precision mode (2ddp), the 2-D solver is naturally the default. Since one of the walls was identified in Gambit as an axis, FLUENT should display an error regarding this as soon as the model is imported. The reason behind this is because in the 2-D solver, FLUENT assumes the model has a unit depth of 1 meter directly into the

screen. There would be no axis of rotation in this case. To rectify this, the axisymmetric solver must be toggled simply by choosing it in the **Define/Models/Solver...** menu.

Following the solver selection, turbulence and, if necessary, the heat equation must be enabled in the **Define/Models...** menu. For the turbulence, the k- ϵ model is chosen, primarily because there is not a large amount of computational resources available for the simulation. (For more information on choosing a turbulence model, see section 12.2 of the FLUENT documentation.) From here, the realizable k- ϵ model is chosen because the RNG k- ϵ model has some problems near the centerline in axisymmetric simulations. Also, the realizable k- ϵ model more accurately describes round jets and flow separation than the standard k- ϵ model. This is important as both effects could occur from a sudden contraction, such as the transition from the reservoir to the N-1 channel.

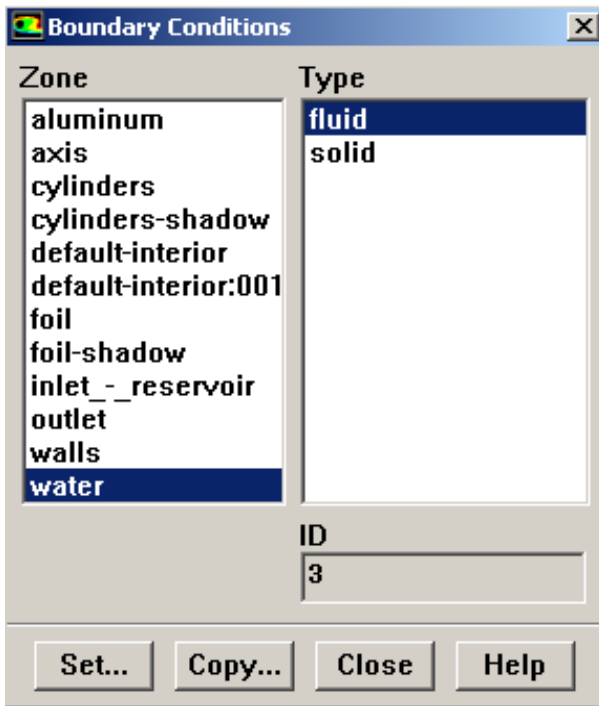
After the desired turbulence is enabled, the material properties are then picked in the **Define/Materials...** menu. For the fluid, FLUENT defaults to air, and for the solid, aluminum. Since there is no interest in conduction in this project, the solid material may be left alone. To simplify things, FLUENT has a built-in database of commonly used materials, one of which being liquid water. Since these properties are based at room temperature, and the actual temperature of the water in the reactor will be around 50 °C, the built-in properties should be slightly altered. Table A.1 lists the original and updated properties.

Table A.1 Default vs. updated properties of water in FLUENT

	Original	Updated
Density (kg/m ³)	998.2	988

Specific Heat (J/kg-K)	4182	4182
Thermal conductivity (W/m-K)	0.6	0.58
Kinematic viscosity (kg/m-s)	1.003×10^{-3}	0.547×10^{-3}

At this point, it should be explained how FLUENT recognizes the materials that are defined in the manner previously mentioned. By specifying properties of a solid or fluid in the materials window, it does not mean FLUENT is applying those numbers to any part of the model. Instead, it is just making the newly defined material available for use. Actually informing FLUENT that a certain feature of the model consists of a certain material is done in the **Define/Boundary Conditions...** menu. When this window is opened, one of the items listed should be the continuum that was defined in Gambit. Figure A.4 displays the window, and in this case, the continuum is water. At this point,



the material is switched from the default (air) to water, and the same should be repeated for any solids that experience conduction. After the materials are assigned, the other boundary conditions are applied. This includes the pressures at the inlet and outlet, turbulence parameters for the inlet and outlet, the inlet water temperature, and the cylinder wall temperature. The turbulence parameters require the knowledge of two

Figure A.4 FLUENT boundary condition window

individual properties that describe the turbulence at that boundary. Any of the 4 pairs FLUENT provides can be implemented, but for this research, the intensity and hydraulic diameter of the flow are picked. Since the reservoir and N-1 channel are both cylinders, the hydraulic diameter of each is just their diameters. The intensity is slightly more complicated. Technically, it is defined by the formula (FLUENT documentation)

$$I = 0.16(Re_{D_h})^{-\frac{1}{8}}. \quad (\text{A.1})$$

Unfortunately, since the Reynolds number requires prior knowledge of the flow velocity, this is difficult to acquire. There is, however, a general guideline that the intensity follows. If the flow does not yet have a boundary layer at the walls, generally characterized as underdeveloped, the intensity can be given a low value. On the other hand, if the flow at the boundary is fully developed, the intensity will be higher, likely around a few percent.

At this point, a step needs to be taken that will reduce the error during the simulation. In the **Solve/Controls/Solution...** menu, there is an option for the discretization of each of the parameters that will be converged. Initially, they are all set to “first order upwind,” except for pressure, which is set to “standard.” The momentum and energy should be changed to “second order upwind” and the pressure to “presto” in an attempt to combat numerical diffusion. Also known as “false diffusion,” numerical diffusion is a source of error that is a byproduct of representing the flow equations in a discrete form. It is most prevalent when the convection is the dominant transport mode, such as the cases described in this report. While switching the discretization to second

order for momentum and energy helps to minimize this, the turbulent kinetic energy and dissipation rate should almost always be left at just a first order, according to the FLUENT staff. On a side note, this menu also contains a way to expedite the convergence process. By unselecting the energy equation here, the flow and turbulence fields will be solved while the energy equation will be left alone. Then, once the hydraulic fields have converged, the energy equation can be re-enabled and the thermal field can be solved. (Do not re-initialize the solution between these two steps or the hydraulic solution will be lost.) The reason that this decreases computation time is due to the speeds at which the thermal and hydraulic fields converge. Because the energy converges very quickly compared to that of the other parameters, leaving it enabled throughout the entire iteration process is unnecessary. After it converges, the energy equation is still solved every iteration, but for no real reason. By leaving it off until the end, the energy calculations do not tie up computational resources.

Up to this point in the report, there has been repeated use of “convergence,” with little description as to what it actually is. As explained before, the mesh is constructed from many cells, and to each, the governing equations are applied once per iteration. The solutions are then fed back into the governing equations during the next

Pressure-Based Segregated Algorithm

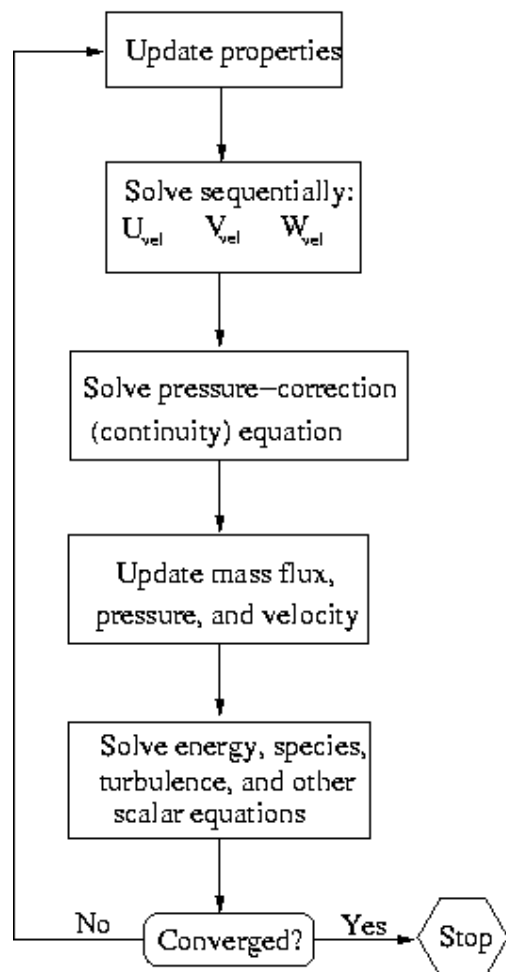


Figure A.5 Iteration process in Fluent

iteration. This process is diagrammed in Fig. A.5 (Fluent documentation). As the iterations progress, the solution to the governing equation begins to change less and less in between each iteration, meaning that the true flow or thermal field is being converged upon. As FLUENT will never result in a perfect solution, the iterations can go on forever, so certain criteria must be established that tell FLUENT that the difference between iterations is small enough to be considered accurate. These criteria are called residuals. In FLUENT, residuals exist for velocity, continuity, energy, turbulent kinetic energy and dissipation rate, and they can be found in the **Solve/Monitors/Residuals...** menu. Initially, the values for the residuals are set at 10^{-3} , except for energy which is at 10^{-6} . To obtain a more accurate solution, they are lowered to at least 10^{-8} . Also, the option is checked for the residuals to be monitored and plotted in real time. During iteration, the general trend of the residuals helps to determine if there are convergence issues. For a full definition and explanation of residuals, it is recommended that the user see the FLUENT documentation, specifically section 25.18.1.

As with any numeric approximation, FLUENT can iterate toward a solution only if it has a place to begin. Since FLUENT cannot know where to begin every problem, this “initial guess” must be input by the user. Located in the **Solve/Initialize/Initialize...** menu, there are two main options in initializing the flow. The first is done by using specific values from an identified zone. The initial values are calculated from the boundary conditions at that location and are calculated for the rest of the model based off these input values. The second option involves providing a value for all zones in the model. This is done by averaging each of the boundary conditions and then applying that to all zones. Neither option is intrinsically better than the other, and either choice should

eventually result in the same solution. One may take a few more iterations than the other to arrive at this destination. Additionally, any of the initial values may be changed manually if the user believes there is a better starting point.

The final step before the iteration begins is one last check of the entire model. FLUENT scans through the grid details, the options that have been selected, and any numbers that have been left as the default and tries to detect potential problems. It then makes recommendations on ways to preemptively solve the problem, though they should not just be blindly followed. For example, since the discretizations for the turbulent kinetic energy and dissipation rate were left as first order upwind, FLUENT will present this as a potential issue; however, as this was intentional, it can be ignored. This checking feature is located in **Solve/Case Check...**, and once completed, the iterations can begin.

Even if all the steps up to this point have been followed, it is no guarantee that the simulation is going to converge without any problems. Sometimes, the residuals may actually begin to increase. This is not necessarily an indication that the simulation has failed. Allow them to settle at a value for at least a few hundred iterations before concluding that they are stagnant. Other times, the residuals decrease for a while and do reach a constant value, but the values are still above the desired level. Frequently, this situation is due to problems with the mesh near the wall. These problems arise because of the complications involved in mathematically describing turbulence near a wall. In general, flow near a wall can be split up into three regions: the viscous sublayer, the outer layer, and the region in between. These are located on Fig. A.6, which demonstrates the relationship between y^+ and the ratio of mean fluid velocity to frictional velocity. Here, y^+ is defined as (Fluent documentation)

$$y^+ \equiv \frac{\rho U_\tau y_P}{\mu}, \tag{A.2}$$

where y_P is the distance from a given point P to the wall. Therefore, y^+ gets smaller the farther from the wall it is considered. The frictional velocity, U_τ , is defined as (Fluent documentation)

$$U_\tau = \sqrt{\frac{\tau_w}{\rho}}. \tag{A.3}$$

In the viscous sublayer, the layer closest to the wall, there is not much turbulence. As a result, viscosity is the major factor in the transport equation. Contrastingly, in the outer

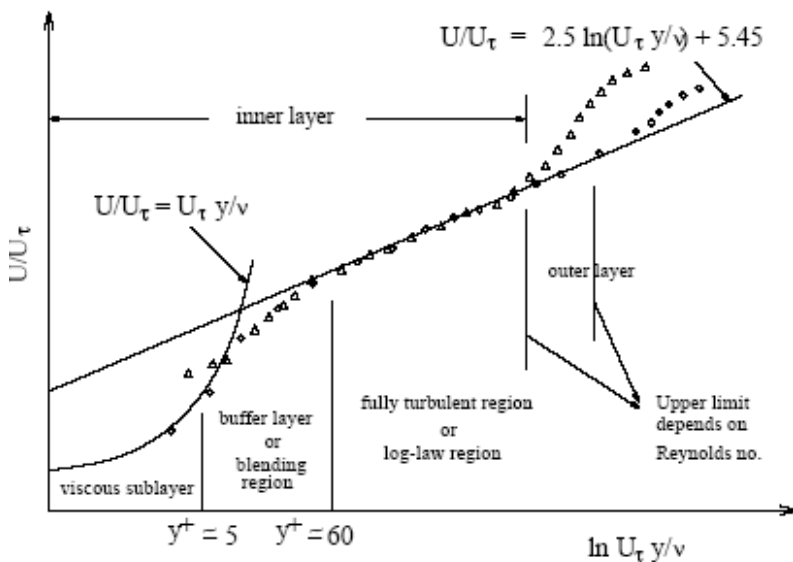


Figure A.6 Divisions of turbulent flow near wall (Fluent documentation)

layer, turbulence is the primary transport mechanism.

Unsurprisingly, the region between the viscous sublayer and the outer layer contains a mixture of

both viscosity and turbulence. In order to effectively model the

complexities of this region, one of two options must be chosen. The first option is to

create a near-wall mesh that is extremely dense, with enough cells to resolve any turbulence that occurs in the middle region. Since this can significantly increase the computation time, it is not used in the bounds of this paper. The second option requires invoking “wall functions.” These are pre-defined correlations based off of experimental trials, and the standard wall function, the default of FLUENT, is based off the work of Launder and Spalding (1974). Frequently dubbed the “log-law,” all of the momentum and energy equations describing this wall function can be found in section 12.10.2 of the FLUENT documentation. The important parameter in these equations is the variable y^* , defined by

$$y^* \equiv \frac{\rho C_{\mu}^{1/4} k_P^{1/2} y_P}{\mu}. \quad (\text{A.4})$$

The y^* value is noteworthy because it determines if the logarithmic law is valid, and it is a plot-able post-processing option that is already available in FLUENT. The range of y^* for which the log-law is valid is from 30 to 300. Despite this range, FLUENT applies the log-law as long as the $y^* > 11.225$, but y^* values less than 30 should be strongly avoided for the standard wall function case because they cause convergence issues.

Appendix B

SINGLE CHANNEL MATLAB CODE

```
% Translational notes:
% Re* denotes a Reynolds number, where the '*' describes the flow
location.
% 'a' denotes annular cylinder flow, '23' denotes flow before the
cylinder,
% 'i' denotes inner cylinder flow.
%
% Similarly, f* usually denotes a friction factor. These use the same
key
% as the Reynolds numbers. The exception is when '*' is a 1,2 or 3.
These
% denote part of the function matrix for the iterative solving.
%
% df*dv* infers a partial derivative of a function 'f*' with respect to
a
% velocity 'v*'.
% 'va' denotes annular velocity, 'v2' denotes velocity before or after
the
% cylinder, etc.

% Appearance
clear
clc
format long
format compact

% Operational/Material constants
dP = 8430;           % driving pressure
rho = 988;          % density
nu = 0.553*10^(-6); % kinematic viscosity
cp = 4182;          % specific heat
k = 0.58;           % thermal conductivity
Pr = nu*rho*cp/k;  % Prandtl number

% Reservoir constants
D1 = 0.3302;        % diameter of reservoir
A1 = 0.25*3.14159*D1^2; % area of reservoir

% Around target flow
Dinn = 0.0265;     % inner diameter of cylinder
Dout = 0.03;       % outer diameter of cylinder
```

```

Ct = 0.5*(Dout - Dinn);           % cylinder thickness
Lc = 0.152;                       % length of cylinder
SAi = pi*Dinn*Lc;                 % inner surface area of cylinder
SAa = pi*Dout*Lc;                 % outer surface area of cylinder
Twi = 323;                       % initial water temperature
Tc = 373;                         % cylinder wall temperature
K2i = 0.15;                      % inlet coefficient for inner flow
K3i = 0.1;                       % exit coefficient for inner flow
K2a = 0.035;                     % inlet coefficient for annular
flow
K3a = 0.03;                       % exit coefficient for annular flow
Awedge = 0.036260;               % total wedge area
L23 = (0.889 - Lc)/2;            % length of channel prior to
cylinder

% User-defined variables: number of flow channels and their diameters
display('Each channel contains 1 annular cylinder target.')
display('Please do not exceed 20 parallel channels. ')
m = input('How many parallel channels are there?');
m = floor(m);

while m > 20
    clc
    display('Each channel contains 1 annular cylinder target.')
    display('Please do not exceed 20 parallel channels. ')
    m = input('How many parallel channels are there?');
    m = floor(m);
end

while m < 1
    clc
    display('No channels for flow. There must be at least 1 channel.')
    m = input('How many parallel channels are there? ');
    m = floor(m);
end

clc
display('The diameter of each flow channel must be greater than:')
D2min = Dout
display(' ')
display('but less than:')
D2max = sqrt(Awedge/m)
% Packing efficiency of channels in wedge is < 100%. The factor of
(4/pi) was dropped to reserve a square area for each channel.
display(' ')
D2 = input('What is the diameter of each flow channel (in meters)? ');

while D2 <= D2min
    clc
    display('The diameter of each flow channel must be greater than:')
    D2min = Dout
    display(' ')
    D2 = input('What is the diameter of each flow channel (in meters)?
');
end

```

```

while D2 >= D2max
    clc
    display('The diameter of each flow channel must be less than:')
    D2max = sqrt(Awedge/m)
    display(' ')
    D2 = input('What is the diameter of each flow channel (in meters)?
');
end

Ratio = A1/m; % entrance area allotted for each channel
Dh1 = sqrt(4*Ratio/pi); % hydraulic diameter
K1 = 0.42*(1-(D2^2/Dh1^2)); % inlet coefficient for each channel

A2 = 0.25*pi*D2^2;
A3 = A2;
A3i = 0.25*pi*(Dinn + Ct)^2;
A3a = 0.25*pi*(D2^2 - (Dinn + Ct)^2);
Ainn = 0.25*pi*Dinn^2;
Dann = D2 - Dout;
Aann = 0.25*pi*(D2^2 - Dout^2);
A4 = A2;
L45 = 0.889 - Lc - L23;
K4 = (1 - (A2*m/Awedge))^2; % exit coefficient out of flow channel

D6min = 0.04445; % Smallest value = current reactor
diameter
D6max = sqrt(Awedge*4/pi); % Largest value is limited by wedge
area
i1 = 0; % loop counter

for D6 = D6min:0.0025:D6max
    i1 = i1 + 1;
    A6 = 0.25*pi*D6^2; % area of exit drain
    K5 = 0.41*(1-(A6/Awedge)); % inlet coefficient into common
drain

    % Initial Conditions
    va = 0.1/m^0.6;
    v2 = 0.1/m^0.6;
    f3 = 1;
    iteration1 = 0;

    while f3 > 10^(-8)
        iteration1 = iteration1 + 1;
        Rea = va*Dann/nu;
        if Rea > 10^5 % high turbulence case
            fa = (1.8*log10(Rea/6.9))^(-2);
            dfadva = (-3.6/log(10))*fa^(3/2)*(1/va);
        elseif Rea < 2300 % laminar case
            fa = 64/Rea;
            dfadva = -64*Rea^(-2)*(Dann/nu);
        else % low turbulence case
            fa = 0.316*Rea^(-1/4);
            dfadva = (-0.316/4)*(Dann/nu)*Rea^(-5/4);
        end
    end
end

```

```

Re23 = v2*D2/nu;
if Re23 > 10^5 % high turbulence case
    f23 = (1.8*log10(Re23/6.9))^(-2);
    df23dv2 = (-3.6/log(10))*f23^(3/2)*(1/v2);
elseif Re23 < 2300 % laminar case
    f23 = 64/Re23;
    df23dv2 = -64*Re23^(-2)*(D2/nu);
else % low turbulence case
    f23 = 0.316*Re23^(-1/4);
    df23dv2 = (-0.316/4)*(D2/nu)*Re23^(-5/4);
end

% Velocities before and after the cylinder are identical
f45 = f23;
df45dv2 = df23dv2;

vi = (A2/Ainn)*v2 - (Aann/Ainn)*va;
Rei = vi*Dinn/nu;
if Rei > 10^5 % high turbulence case
    fi = (1.8*log10(Rei/6.9))^(-2);
    dfidv2 = (-3.6/log(10))*fi^(3/2)*(1/vi)*(A2/Ainn);
    dfidva = (-3.6/log(10))*fi^(3/2)*(-Aann/Ainn)*(1/vi);
elseif Rei < 2300 % laminar case
    fi = 64/Rei;
    dfidv2 = -64*Rei^(-2)*(Dinn/nu)*(A2/Ainn);
    dfidva = -64*Rei^(-2)*(Dinn/nu)*(-Aann/Ainn);
else % low turbulence case
    fi = 0.316*Rei^(-1/4);
    dfidv2 = (-0.316/4)*Rei^(-5/4)*(Dinn/nu)*(A2/Ainn);
    dfidva = (-0.316/4)*Rei^(-5/4)*(-Dinn/nu)*(Aann/Ainn);
end

f1 = -(2*dP/rho) + (K1 + f23*(L23/D2) + f45*(L45/D2) + K4)*v2^2
+ (1 + K5)*(m*(A2/A6)*v2)^2 + (K2a + fa*(Lc/Dann) + K3a)*va^2;
f2 = (K2a + fa*(Lc/Dann) + K3a)*va^2 - (K2i + fi*(Lc/Dinn) +
K3i)*vi^2;
df1dva = (K2a + fa*(Lc/Dann) + K3a)*2*va +
(Lc/Dann)*va^2*dfadva;
df1dv2 = (K1 + f23*(L23/D2) + f45*(L45/D2) + K4)*2*v2 +
((L23/D2)*df23dv2 + (L45/D2)*df45dv2)*v2^2 + (1 + K5)*(m*A2/A6)^2*2*v2;
df2dva = df1dva - ((K2i + fi*(Lc/Dinn) + K3i)*2*vi*(-Aann/Ainn)
+ vi^2*(Lc/Dann)*dfidva);
df2dv2 = -(K2i + fi*(Lc/Dinn) + K3i)*2*vi*(A2/Ainn) -
vi^2*(Lc/Dinn)*dfidv2;

x = [v2 va]'; % initial guess
f = [f1 f2]'; % function matrix
J = [df1dv2 df1dva; df2dv2 df2dva]; % Jacobian

x = x - inv(J)*f; % new guess

v2 = x(1);
va = x(2);

```

```

        f3 = abs(f1) + abs(f2);      % convergence variable
    end

    % Temporary substitutions for value storage
    D6opt(i1) = D6;
    v2opt(i1) = v2;
    vaopt(i1) = va;
    iter(i1) = iteration1;
    K5opt(i1) = K5;
end

% Re-substitution to initial names
D6 = D6opt;      % drain diameter
v2 = v2opt;      % velocity prior to target
va = vaopt;      % velocity at annular part of channel
iteration1 = iter; % number of iterations until
convergence
K5 = K5opt;

%%%%%%%%%%%%%%%%%%%%%%%%%%%%%%%%%%%%%%%%%%%%%%%%%%%%%%%%%%%%%%%%%%%%%%%%
%% Flow calculations %%
%%%%%%%%%%%%%%%%%%%%%%%%%%%%%%%%%%%%%%%%%%%%%%%%%%%%%%%%%%%%%%%%%%%%%%%%
A6 = 0.25*pi*D6.^2;      % area of exit drain

% Velocity
v3 = v2;
vi = (A2/Ainn)*v2 - (Aann/Ainn)*va;
v3a = (Aann/A3a)*va;
v3i = (Ainn/A3i)*vi;
v4 = v2;
v5 = v2;
v5common = m*(A2/Awedge)*v2;
v6 = m*(A2./A6).*v2;

% Pressure Gradient
dp12 = 0.5*(1 + K1)*rho*v2.^2;
Re23 = v2*D2/nu;
Rei = vi*Dinn/nu;
Rea = va*Dann/nu;
Re45 = v4*D2/nu;

size = nnz(iteration1);

for i3 = 1:size
    if Re23(i3) >= 10^5
        f23 = (1.8*log10(Re23(i3)/6.9))^(-2);
    elseif Re23(i3) <= 2300
        f23 = 64/Re23(i3);
        display('Re23 is not turbulent anymore.')
    else
        f23 = 0.316*Re23(i3)^(-0.25);
    end
    f23i(i3) = f23;
end

```

```

if Re1(i3) >= 10^5
    fi = (1.8*log10(Re1(i3)/6.9))^(-2);
elseif Re1(i3) <= 2300
    fi = 64/Re1(i3);
    display('Re1 is not turbulent anymore.')
else
    fi = 0.316*Re1(i3)^(-0.25);
end
fii(i3) = fi;

if Rea(i3) >= 10^5
    fa = (1.8*log10(Rea(i3)/6.9))^(-2);
elseif Rea(i3) <= 2300
    fa = 64/Rea(i3);
    display('Rea is not turbulent anymore.')
else
    fa = 0.316*Rea(i3)^(-0.25);
end
fai(i3) = fa;

if Re45(i3) >= 10^5
    f45 = (1.8*log10(Re45(i3)/6.9))^(-2);
elseif Re45(i3) <= 2300
    f45 = 64/Re45(i3);
    display('Re45 is not turbulent anymore.')
else
    f45 = 0.316*Re45(i3)^(-0.25);
end
f45i(i3) = f45;
end

f23 = f23i;
fi = fii;
fa = fai;
f45 = f45i;

dp23 = 0.5*rho*v2.^2.*f23*(L23/D2);
dp34 = 0.5*rho*va.^2.*(K2a + fa*(Lc/Dann) + K3a);
dp34i = 0.5*rho*vi.^2.*(K2i + fi*(Lc/Dinn) + K3i);
check34 = abs(dp34i - dp34);
dp45 = f45*(L45/D2)*0.5*rho.*v2.^2;
dp55common = (K4 - 1)*0.5*rho*v2.^2 + 0.5*rho*v5common.^2;
dp5common6 = (1 + K5)*0.5*rho.*v6.^2 - 0.5*rho*v5common.^2;

% Static Pressure
Ps1 = dP;
Ps2 = Ps1 - dp12;
Ps3 = Ps2 - dp23;
Ps4 = Ps3 - dp34;
Ps5 = Ps4 - dp45;
Ps5common = Ps5 - dp55common;
Ps6 = Ps5common - dp5common6;

% Total Pressure
Pt1 = Ps1;
Pt2 = Ps2 + 0.5*rho*v2.^2;

```

```

Pt3i = Ps3 + 0.5*rho*v3i.^2;
Pt3a = Ps3 + 0.5*rho*v3a.^2;
Pt3 = Ps3 + 0.5*rho*v3.^2;
Pt4 = Ps4 + 0.5*rho*v4.^2;
Pt5 = Ps5 + 0.5*rho*v5.^2;
Pt5common = Ps5common + 0.5*rho*v5common.^2;
Pt6 = Ps6 + 0.5*rho*v6.^2;

% Mass flow rate
mdoti = rho*vi*Ainn;
mdota = rho*va*Aann;
mdot2 = rho*v2*A2;
checkmdot = abs(mdoti + mdota - mdot2);
mdot5common = rho*v5common.*Awedge;
mdot6 = rho*v6.*A6;
checkmdot56 = mdot6 - mdot5common;

% Resistance
R12 = (Pt1 - Pt2)./mdot2;
R23 = (Pt2 - Pt3)./mdot2;
R34i = dp34./mdoti;
R34a = dp34./mdota;
R34 = (1./R34i + 1./R34a).^(-1);
% checkR34 = abs((Pt3 - Pt4)./mdot2 - R34);
R45 = (Pt4 - Pt5)./mdot2;
R55common = (Pt5 - Pt5common)./mdot5common;
R5common6 = (Pt5common - Pt6)./mdot6;

RN1 = R12 + R23 + R34 + R45 + R55common;
%checkRN1 = abs((dp23 + dp34 + dp45)./mdot2 - RN1);
Rtot = RN1/m + R5common6;
mdottot = (dP - Pt6)./Rtot;
Rrat = R5common6./Rtot;

%%%%%%%%%%%%%%%%%%%%%%%%%%%%%%%%%%%%%%%%%%%%%%%%%%%%%%%%%%%%%%%%%%%%%%%%
%%% Heat Transfer calculations %%%
%%%%%%%%%%%%%%%%%%%%%%%%%%%%%%%%%%%%%%%%%%%%%%%%%%%%%%%%%%%%%%%%%%%%%%%%

% Heat transfer from inner surface of heated cylinder
if Rei <= 2300
    Nui = 3.66;
else
    Nui = 0.023*(Rei.^0.8)*(Pr^0.4)*(1+(Dinn/Lc)^(2/3));
end
hi = Nui*k/Dinn;
dT_i = (Tc - Twi)*(1 - exp(-hi*SAi./(cp*mdoti)));
qi = mdoti*cp.*dT_i;

% Heat transfer from annular surface of heated cylinder
Nua = 0.023*(Rea.^0.8)*(Pr^0.4)*(1+(Dann/Lc)^(2/3));
ha = Nua*k/Dann;
dT_a = (Tc - Twi)*(1 - exp(-ha*SAa./(cp*mdota)));
qa = mdota*cp.*dT_a;

```

```

SAf = 0.25*pi*(Dout^2 - Dinn^2);      % front surface area of
cylinder
qcyl = ((SAi + SAa + 2*SAf)/(SAi + SAa))*(qi + qa);
qtot = m.*qcyl;

%%%%%%%%%%%%%%%%%%%%%%%%%%%%%%%%%%%%%%%%%%%%%%%%%%%%%%%%%%%%%%%%%%%%%%%%
%%% Entropy Generation calculations %%%
%%%%%%%%%%%%%%%%%%%%%%%%%%%%%%%%%%%%%%%%%%%%%%%%%%%%%%%%%%%%%%%%%%%%%%%%

% Thermally generated entropy
Sgen1 = mdoti*cp.*log((dT_i + T_wi)/T_wi) + mdota*cp.*log((dT_a +
T_wi)/T_wi);
Sgentherm = m.*Sgen1;

% Hydrodynamically generated entropy
Sgen2 = (mdot2/(rho*T_wi)).*(Pt1 - Pt2) + (mdot2/(rho*T_wi)).*(Pt2 -
Pt3) + (mdoti/(rho*T_wi)).*(Pt3 - Pt4) + (mdota/(rho*T_wi)).*(Pt3 - Pt4)
+ (mdot2./(rho*(T_wi + (mdoti.*dT_i + mdota.*dT_a)./mdot2))).*(Pt4 - Pt5)
+ (mdot2/(rho*T_wi)).*(Pt5 - Pt5common);
Sgenhydro = m.*Sgen2 + (mdot6/(rho*T_wi)).*(Pt5common - Ps6);

Sgentot = Sgentherm + Sgenhydro;

```

Appendix C

MULTIPLE CHANNEL MATLAB CODE

```
% Translational notes:
% Re* denotes a Reynolds number, where the '*' describes the flow
location.
% 'a' denotes annular cylinder flow, '23' denotes flow before the
cylinder,
% 'i' denotes inner cylinder flow.
%
% Similarly, f* usually denotes a friction factor. These use the same
key
% as the Reynolds numbers. The exception is when '*' is a 1,2 or 3.
These
% denote part of the function matrix for the iterative solving.
%
% df*dv* infers a partial derivative of a function 'f*' with respect to
a
% velocity 'v*'.
% 'va' denotes annular velocity, 'v2' denotes velocity before or after
the
% cylinder, etc.

% Appearance
clear
clc
format long
format compact

% Operational/Material constants
dP = 8430;           % driving pressure
rho = 988;          % density
nu = 0.553*10^(-6); % kinematic viscosity
cp = 4182;          % specific heat
k = 0.58;           % thermal conductivity
Pr = nu*rho*cp/k;   % Prandtl number

% Reservoir constants
D1 = 0.3302;        % diameter of reservoir
A1 = 0.25*3.14159*D1^2; % area of reservoir

% Around target flow
Dinn = 0.0265;     % inner diameter of cylinder
Dout = 0.03;       % outer diameter of cylinder
Ct = 0.5*(Dout - Dinn); % cylinder thickness
Lc = 0.152;        % length of cylinder
SAi = pi*Dinn*Lc;  % inner surface area of cylinder
SAa = pi*Dout*Lc; % outer surface area of cylinder
Twi = 323;         % initial water temperature
```

```

Tc = 373; % cylinder wall temperature
K2i = 0.15; % inlet coefficient for inner flow
K3i = 0.1; % exit coefficient for inner flow
K2a = 0.035; % inlet coefficient for annular
flow
K3a = 0.03; % exit coefficient for annular flow
Awedge = 0.036260; % total wedge area
L23 = (0.889 - Lc)/2; % length of channel prior to
cylinder

% Wedge exit constants
factor = input('How many factors larger than the existing diameter
should the exit diameter to the wedge be?');
D6 = 0.04445*(1 + factor); % diameter of exit drain
A6 = 0.25*pi*D6^2; % area of exit drain

while A6 > Awedge
    display('Exit drain cannot exceed wedge area.')
    factor = input('How many factors larger than the existing diameter
should the exit diameter to the wedge be?');
    D6 = 0.04445*(1 + factor); % diameter of exit drain
    A6 = 0.25*pi*D6^2; % area of exit drain
    clc
end

K5 = 0.41*(1-(A6/Awedge)); % inlet coefficient into common
drain

% Determining what variables the program will prompt for
display('Will you be testing a specific case or performing general
optimization?')
choice = input('1 = specific case, 2 = optimizing, 3 = help ');

if choice == 3 % Provides a brief description of options
    clc
    display('"SPECIFIC CASE" requires the user to set the number of
channels with cylinders and the diameters.')
    display('"OPTIMIZATION" automatically assumes all channels contain
a cylinder and iterates on the total number of channels. The user input
for this option is the diameter of the channels.')
    display('Please restart this .m file from the beginning.')
    pause

elseif choice == 1 % When a specific case is desired
% User inputs
clc
m = input('How many channels contain a cylinder?');
m = floor(m);

% Initial sanity checks on user inputs
while m < 1
    clc
    display('Number of channels does not allow for flow.')
    m = input('How many channels contain a cylinder?');
    m = floor(m);

```

```

end

D2 = input('What is the diameter of the channel that contains a
cylinder (in meters)?');
while D2 <= Dout
    clc
    display('Channel must be larger than the cylinder it contains.')
    D2 = input('What is the diameter of the channel that contains a
cylinder (in meters)?');
end

A2 = 0.25*pi*D2^2;           % area of channels with cylinders
Areacheck = m*A2;          % total area of all channels

while Areacheck > Awedge
    clc
    display('Either too many channels or channels are too big.')
    display('Remember, the total channel area cannot exceed the wedge
area.')
    display('Please select from the following options:')
    fix = input('1 = Change the number of channels, 2 = Change the
diameter of the channels, 3 = change both');

    if fix == 1
        clc
        m = input('How many channels contain a cylinder?');
        m = floor(m);
    elseif fix == 2
        clc
        D2 = input('What is the diameter of the channel that contains a
cylinder (in meters)?');
    elseif fix == 3
        clc
        m = input('How many channels contain cylinders?');
        m = floor(m);
        D2 = input('What is the diameter of the channel that contains a
cylinder (in meters)?');
    else
        clc
        display('invalid syntax')
        display('Please restart this .m file from the beginning.')
        pause
    end

    A2 = 0.25*pi*D2^2;           % area of channels with cylinders
    Areacheck = m*A2;          % total area of all channels
end

% Entrance coefficient
Rat1 = A1/m;                   % area allotted to each cylinder
channel
Dh1 = sqrt(4*Rat1/pi);         % hydraulic diameter for cylinder
channels
K1 = 0.42*(1-(D2^2/Dh1^2));    % entrance coefficient for cylinder
channels

```

```

% Around target flow
Dann = D2 - Dout; % diameter of annulus
A3 = A2; % area of channel before cylinder
A3i = 0.25*pi*(Dinn + Ct)^2;
A3a = 0.25*pi*(D2^2 - (Dinn + Ct)^2);
Ainn = 0.25*pi*Dinn^2; % cross-section area of inner flow
Aann = 0.25*pi*(D2^2 - Dout^2); % cross-section area of annular
flow
% Post-target flow
A4 = A2; % area of channel after cylinder
L45 = 0.889 - Lc - L23; % length after cylinder to exit
K4 = (1 - (m*A2/Awedge))^2; % expansion coefficient before
drain

% Initial Conditions
v2m = 0.1/m; % velocity in empty channel
va = 0.1/m; % velocity of annular flow
v2 = 0.1/m; % velocity in front of cylinder
f3 = 1; % convergence variable
i1 = 0; % loop counter 1

% Iterative Newton-Raphson Loop
while f3 > 10^(-6)
    i1 = i1 + 1;

    Rea = va*Dann/nu;
    if Rea > 10^5 % high turbulence case
        fa = (1.8*log10(Rea/6.9))^(-2);
        dfadva = (-3.6/log(10))*fa^(3/2)*(1/va);
    elseif Rea < 2300 % laminar case
        fa = 64/Rea;
        dfadva = -64*Rea^(-2)*(Dann/nu);
    else % low turbulence case
        fa = 0.316*Rea^(-1/4);
        dfadva = (-0.316/4)*(Dann/nu)*Rea^(-5/4);
    end

    Re23 = v2*D2/nu;
    if Re23 > 10^5 % high turbulence case
        f23 = (1.8*log10(Re23/6.9))^(-2);
        df23dv2 = (-3.6/log(10))*f23^(3/2)*(1/v2);
    elseif Re23 < 2300 % laminar case
        f23 = 64/Re23;
        df23dv2 = -64*Re23^(-2)*(D2/nu);
    else % low turbulence case
        f23 = 0.316*Re23^(-1/4);
        df23dv2 = (-0.316/4)*(D2/nu)*Re23^(-5/4);
    end

    f45 = f23;
    df45dv2 = df23dv2;

    Rei = (Dinn/nu)*((A2/Ainn)*v2 - (Aann/Ainn)*va);
    if Rei > 10^5 % high turbulence case

```

```

        fi = (1.8*log10(Rei/6.9))^( -2);
        dfidv2 = (-3.6/log(10))*fi^(3/2)*((A2/Ainn)*v2 -
(Aann/Ainn)*va)^(-1)*(A2/Ainn);
        dfidva = (-3.6/log(10))*fi^(3/2)*(-Aann/Ainn)*((A2/Ainn)*v2 -
(Aann/Ainn)*va)^(-1);
        elseif Rei < 2300                                % laminar case
            fi = 64/Rei;
            dfidv2 = -64*Rei^(-2)*(Dinn/nu)*(A2/Ainn);
            dfidva = -64*Rei^(-2)*(Dinn/nu)*(-Aann/Ainn);
        else                                              % low turbulence case
            fi = 0.316*Rei^(-1/4);
            dfidv2 = (-0.316/4)*Rei^(-5/4)*(Dinn/nu)*(A2/Ainn);
            dfidva = (-0.316/4)*Rei^(-5/4)*(-Dinn/nu)*(Aann/Ainn);
        end

        f1 = -(2*dP/rho) + (K1 + f23*(L23/D2) + f45*(L45/D2) + K4)*v2^2 +
(1 + K5)*(m*(A2/A6)*v2)^2 + (K2a + fa*(Lc/Dann) + K3a)*va^2;
        f2 = (K2a + fa*(Lc/Dann) + K3a)*va^2 - (K2i + fi*(Lc/Dinn) +
K3i)*((A2/Ainn)*v2 - (Aann/Ainn)*va)^2;
        dfldva = (K2a + fa*(Lc/Dann) + K3a)*2*va + (Lc/Dann)*va^2*dfadva;
        dfldv2 = (K1 + f23*(L23/D2) + f45*(L45/D2) + K4)*2*v2 +
((L23/D2)*df23dv2 + (L45/D2)*df45dv2)*v2^2 + (1 + K5)*(m*A2/A6)^2*2*v2;
        df2dva = dfldva - (2*(K2i + fi*(Lc/Dinn) + K3i)*((A2/Ainn)*v2 -
(Aann/Ainn)*va)*(-Aann/Ainn) + ((A2/Ainn)*v2 -
(Aann/Ainn)*va)^2*(Lc/Dann)*dfidva);
        df2dv2 = -2*(K2i + fi*(Lc/Dinn) + K3i)*((A2/Ainn)*v2 -
(Aann/Ainn)*va)*(A2/Ainn) - ((A2/Ainn)*v2 -
(Aann/Ainn)*va)^2*(Lc/Dinn)*dfidv2;

        x = [v2 va]';                                     % initial guess
        f = [f1 f2]';                                     % function matrix
        J = [dfldv2 dfldva; df2dv2 df2dva];             % Jacobian

        x = x - inv(J)*f;                                 % new guess

        v2 = x(1);
        va = x(2);

        f3 = abs(f1) + abs(f2);                          % convergence variable
    end

elseif choice == 2                                     % When optimization is desired
    D2 = input('What is the diameter of the channel that contains a
cylinder (in meters)?');
    A2 = 0.25*pi*D2^2;
    maxm = Awedge/D2^2;                                  % Packing efficiency of channels in
wedge is < 100%.
    % The factor of (4/pi) was dropped to reserve a square area for
each channel.

    Dann = D2 - Dout;
    A3 = A2;
    A3i = 0.25*pi*(Dinn + Ct)^2;
    A3a = 0.25*pi*(D2^2 - (Dinn + Ct)^2);

```

```

Ainn = 0.25*pi*Dinn^2;
Aann = 0.25*pi*(D2^2 - Dout^2);
A4 = A2;
L45 = 0.889 - Lc - L23;

m = 0;
i2 = 0; % loop counter 2
while m < maxm
    m = m + 1;
    i2 = i2 + 1;

    Ratio = A1/m; % entrance area allotted for each
channel Dh1 = sqrt(4*Ratio/pi); % hydraulic diameter
channel K1 = 0.42*(1-(D2^2/Dh1^2)); % inlet coefficient for each
channel K4 = (1 - (m*A2/Awedge))^2; % expansion coefficient in front of
drain

    % Initial Conditions
    va = 0.1/m^0.6;
    v2 = 0.1/m^0.6;
    f3 = 1;
    v2m = 0;

    while f3 > 10^(-6)
        Rea = va*Dann/nu;
        if Rea > 10^5 % high turbulence case
            fa = (1.8*log10(Rea/6.9))^(-2);
            dfadva = (-3.6/log(10))*fa^(3/2)/va;
        elseif Rea < 2300 % laminar case
            fa = 64/Rea;
            dfadva = -64*Rea^(-2)*(Dann/nu);
        else % low turbulence case
            fa = 0.316*Rea^(-1/4);
            dfadva = (-0.316/4)*(Dann/nu)*Rea^(-5/4);
        end

        Re23 = v2*D2/nu;
        if Re23 > 10^5 % high turbulence case
            f23 = (1.8*log10(Re23/6.9))^(-2);
            df23dv2 = (-3.6/log(10))*f23^(3/2)*(1/v2);
        elseif Re23 < 2300 % laminar case
            f23 = 64/Re23;
            df23dv2 = -64*Re23^(-2)*(D2/nu);
        else % low turbulence case
            f23 = 0.316*Re23^(-1/4);
            df23dv2 = (-0.316/4)*(D2/nu)*Re23^(-5/4);
        end

        % Velocities before and after the cylinder are identical
        f45 = f23;
        df45dv2 = df23dv2;
    end
end

```

```

    f1 = -(2*dP/rho) + (K1 + f23*(L23/D2) + f45*(L45/D2) + K4)*v2^2
+ (1 + K5)*(m*(A2/A6)*v2)^2 + (K2a + fa*(Lc/Dann) + K3a)*va^2;
    df1dv2 = (K1 + f23*(L23/D2) + f45*(L45/D2) + K4)*2*v2 +
((L23/D2)*df23dv2 + (L45/D2)*df45dv2)*v2^2 + (1 + K5)*(m*A2/A6)^2*2*v2;
    df1dva = (K2a + fa*(Lc/Dann) + K3a)*2*va +
(Lc/Dann)*va^2*dfadva;
    df2dv2 = (K1 + f23*(L23/D2) + f45*(L45/D2) + K4)*2*v2 +
((L23/D2)*df23dv2 + (L45/D2)*df45dv2)*v2^2 + (1 + K5)*(m*A2/A6)^2*2*v2;

vi = (A2/Ainn)*v2 - (Aann/Ainn)*va;
Rei = vi*Dinn/nu;
if Rei > 10^5 % high turbulence case
    fi = (1.8*log10(Rei/6.9))^(-2);
    dfidv2 = (-3.6/log(10))*fi^(3/2)*(1/vi)*(A2/Ainn);
    dfidva = (-3.6/log(10))*fi^(3/2)*(-Aann/Ainn)*(1/vi);
elseif Rei < 2300 % laminar case
    fi = 64/Rei;
    dfidv2 = -64*Rei^(-2)*(Dinn/nu)*(A2/Ainn);
    dfidva = -64*Rei^(-2)*(Dinn/nu)*(-Aann/Ainn);
else % low turbulence case
    fi = 0.316*Rei^(-1/4);
    dfidv2 = (-0.316/4)*Rei^(-5/4)*(Dinn/nu)*(A2/Ainn);
    dfidva = (-0.316/4)*Rei^(-5/4)*(-Dinn/nu)*(Aann/Ainn);
end

f2 = (K2a + fa*(Lc/Dann) + K3a)*va^2 - (K2i + fi*(Lc/Dinn) +
K3i)*vi^2;
df2dva = df1dva - ((K2i + fi*(Lc/Dinn) + K3i)*2*vi*(-Aann/Ainn)
+ vi^2*(Lc/Dann)*dfidva);
df2dv2 = -(K2i + fi*(Lc/Dinn) + K3i)*2*vi*(A2/Ainn) -
vi^2*(Lc/Dinn)*dfidv2;

x = [v2 va]'; % initial guess
f = [f1 f2]'; % function matrix
J = [df1dv2 df1dva; df2dv2 df2dva]; % Jacobian

x = x - inv(J)*f; % new guess

v2 = x(1);
va = x(2);

f3 = abs(f1) + abs(f2); % convergence variable
end

% Temporary substitutions for value storage
K1opt(i2) = K1;
v2opt(i2) = v2;
vaopt(i2) = va;
channels(i2) = m;
K4opt(i2) = K4;
end

% Re-substitution to initial names
K1 = K1opt;
v2 = v2opt;
va = vaopt;
m = channels;

```

```

    K4 = K4opt;

else
    clc
    display('invalid syntax')
    display('Please restart this .m file from the beginning.')
    pause
end

%%%%%%%%%%%%%%%%%%%%%%%%%%%%%%%%%%%%%%%%%%%%%%%%%%%%%%%%%%%%%%%%%%%%%%%%
%%% Flow calculations %%%
%%%%%%%%%%%%%%%%%%%%%%%%%%%%%%%%%%%%%%%%%%%%%%%%%%%%%%%%%%%%%%%%%%%%%%%%

% Velocity
v3 = v2;
vi = (A2/Ainn)*v2 - (Aann/Ainn)*va;
v3a = (Aann/A3a)*va;
v3i = (Ainn/A3i)*vi;
v4 = v2;
v5 = v2;
v5common = m*(A2/Awedge).*v2;
v6 = m*(A2/A6).*v2;

% Pressure Gradient
dp12 = 0.5*(1 + K1)*rho.*v2.^2;
Re23 = v2*D2/nu;
Rei = vi*Dinn/nu;
Rea = va*Dann/nu;
Re45 = v4*D2/nu;

size = nnz(m);

for i3 = 1:size
    if Re23(i3) >= 10^5
        f23 = (1.8*log10(Re23(i3)/6.9))^(-2);
    elseif Re23(i3) <= 2300
        f23 = 64/Re23(i3);
        display('Re23 is not turbulent anymore.')
    else
        f23 = 0.316*Re23(i3)^(-0.25);
    end
    f23i(i3) = f23;

    if Rei(i3) >= 10^5
        fi = (1.8*log10(Rei(i3)/6.9))^(-2);
    elseif Rei(i3) <= 2300
        fi = 64/Rei(i3);
        display('Rei is not turbulent anymore.')
    else
        fi = 0.316*Rei(i3)^(-0.25);
    end
    fii(i3) = fi;

    if Rea(i3) >= 10^5

```

```

        fa = (1.8*log10(Rea(i3)/6.9))^(-2);
elseif Rea(i3) <= 2300
    fa = 64/Rea(i3);
    display('Rea is not turbulent anymore.')
```

```

else
    fa = 0.316*Rea(i3)^(-0.25);
end
fai(i3) = fa;

if Re45(i3) >= 10^5
    f45 = (1.8*log10(Re45(i3)/6.9))^(-2);
elseif Re45(i3) <= 2300
    f45 = 64/Re45(i3);
    display('Re45 is not turbulent anymore.')
```

```

else
    f45 = 0.316*Re45(i3)^(-0.25);
end
f45i(i3) = f45;
end

f23 = f23i;
fi = fii;
fa = fai;
f45 = f45i;

dp23 = 0.5*rho*v2.^2.*f23*(L23/D2);
dp34 = 0.5*rho*va.^2.*(K2a + fa*(Lc/Dann) + K3a);
%dp34 = 0.5*rho*vi.^2.*(K2i + fi*(Lc/Dinn) + K3i);
check34 = abs(0.5*rho*va.^2.*(K2a + fa*(Lc/Dann) + K3a) - dp34);
dp45 = f45*(L45/D2)*0.5*rho.*v2.^2;
dp55common = (K4 - 1)*0.5*rho.*v2.^2 + 0.5*rho*v5common.^2;
dp5common6 = (1 + K5)*0.5*rho*v6.^2 - 0.5*rho*v5common.^2;

% Static Pressure
Ps1 = dP;
Ps2 = Ps1 - dp12;
Ps3 = Ps2 - dp23;
Ps4 = Ps3 - dp34;
Ps5 = Ps4 - dp45;
Ps5common = Ps5 - dp55common;
Ps6 = Ps5common - dp5common6;

% Total Pressure
Pt1 = Ps1;
Pt2 = Ps2 + 0.5*rho*v2.^2;
Pt3i = Ps3 + 0.5*rho*v3i.^2;
Pt3a = Ps3 + 0.5*rho*v3a.^2;
Pt3 = Ps3 + 0.5*rho*v3.^2;
Pt4 = Ps4 + 0.5*rho*v4.^2;
Pt5 = Ps5 + 0.5*rho*v5.^2;
Pt5common = Ps5common + 0.5*rho*v5common.^2;
Pt6 = Ps6 + 0.5*rho*v6.^2;

% Mass flow rate
mdoti = rho*vi*Ainn;
mdota = rho*va*Aann;

```

```

mdot2 = rho*v2*A2;
checkmdot = abs(mdoti + mdota - mdot2);
mdot5common = rho*v5common*Awedge;
mdot6 = rho*v6*A6;
checkmdot56 = mdot6 - mdot5common;

% Resistance
R12 = (Pt1 - Pt2)./mdot2;
R23 = (Pt2 - Pt3)./mdot2;
R34i = dp34./mdoti;
R34a = dp34./mdota;
R34 = ((1./R34i)+(1./R34a)).^(-1);
%checkR34 = abs((Pt3 - Pt4)./mdot2 - R34);
R45 = (Pt4 - Pt5)./mdot2;
R55common = (Pt5 - Pt5common)./mdot5common;
R5common6 = (Pt5common - Pt6)./mdot6;

RN1 = R12 + R23 + R34 + R45 + R55common;
% checkRN1 = abs((dp12 + dp23 + dp34 + dp45)./mdot2 - RN1);
%checkR56 = abs((dP - Pt5)./mdot6 - R55common - R5common6);
Rtot = RN1./m + R5common6;
mdottot = (dP - Pt6)./Rtot;
Rrat = R5common6./Rtot;

%%%%%%%%%%%%%%%%%%%%%%%%%%%%%%%%%%%%%%%%%%%%%%%%%%%%%%%%%%%%%%%%%%%%%%%%
%%% Heat Transfer calculations %%%
%%%%%%%%%%%%%%%%%%%%%%%%%%%%%%%%%%%%%%%%%%%%%%%%%%%%%%%%%%%%%%%%%%%%%%%%
% Heat transfer from inner surface of heated cylinder
Nui = 0.023*(Rei.^0.8)*(Pr.^0.4)*(1+(Dinn/Lc)^(2/3));
hi = Nui*k/Dinn;
dT_i = (Tc - Twi)*(1 - exp(-hi*SAi./(cp*mdoti)));
qi = mdoti*cp.*dT_i;

% Heat transfer from annular surface of heated cylinder
Nua = 0.023*(Rea.^0.8)*(Pr.^0.4)*(1+(Dann/Lc)^(2/3));
ha = Nua*k/Dann;
dT_a = (Tc - Twi)*(1 - exp(-ha*SAa./(cp*mdota)));
qa = mdota*cp.*dT_a;

SAf = 0.25*pi*(Dout^2 - Dinn^2); % front surface area of cylinder
qcyl = ((SAi + SAa + 2*SAf)/(SAi + SAa))*(qi + qa);
qtot = m.*qcyl;

%%%%%%%%%%%%%%%%%%%%%%%%%%%%%%%%%%%%%%%%%%%%%%%%%%%%%%%%%%%%%%%%%%%%%%%%
%%% Entropy Generation calculations %%%
%%%%%%%%%%%%%%%%%%%%%%%%%%%%%%%%%%%%%%%%%%%%%%%%%%%%%%%%%%%%%%%%%%%%%%%%

% Thermally generated entropy
Sgen1 = mdoti*cp.*log((dT_i + Twi)/Twi) + mdota*cp.*log((dT_a + Twi)/Twi);
Sgentherm = m.*Sgen1;

% Hydrodynamically generated entropy

```

```

Sgen2 = (mdot2/(rho*Twi)).*(Pt1 - Pt2) + (mdot2/(rho*Twi)).*(Pt2 -
Pt3) + (mdoti/(rho*Twi)).*(Pt3 - Pt4) + (mdota/(rho*Twi)).*(Pt3 - Pt4)
+ (mdot2./(rho*(Twi + (mdoti.*dT_i + mdota.*dTa)./mdot2))).*(Pt4 - Pt5)
+ (mdot2/(rho*Twi)).*(Pt5 - Pt5common);
Sgenhydro = m.*Sgen2 + (mdot6/(rho*Twi)).*(Pt5common - Ps6);

Sgentot = Sgentherm + Sgenhydro;

```

REFERENCES

- Allen, C.W., Butler, R.A., Jarousse, C.A., Falgoux, J.L., 2007, "Feasibility development program, LEU foil plate target for the production of molybdenum-99," *RERTR 2007 International Meeting, Prague, Czech Republic*.
- Allen, C. and Peters, N., 2008, Columbia, MO (personal communication).
- Bejan, A., 2006, *Advanced Engineering Thermodynamics*, 3rd edition, John Wiley & Sons, Hoboken, 44-65.
- Bruun, H. H., 1995, *Hot-Wire Anemometry: Principles and Signal Analysis*, Oxford University Press, 19-41.
- CANDU Fundamentals, Chapter 7. *Fission*, 2004, <http://canteach.candu.org/>, (2008).
- Cengel, Y.A., 2003, *Heat Transfer: A Practical Approach*, 2nd edition, McGraw-Hill Professional, New York, 443-444.
- Connolly, H.W. and Clancy, B.E., 1993, "The Science and Engineering of HIFAR Safety," ANSTO report, 5-1 – 5-11.
- Dishongh, T., Kelly, P.J., Kelkar, K.M., and Patankar, S.V., 2000, *Rapid and Accurate System-Level Design for Electronics Packaging and Production using Flow Network Modeling (FNM) – A Case Study for the Design of a Burn-In Oven*, Intel, Hillsboro, 1-8.
- FLUENT documentation, FLUENT 6.3.26 (2008).
- Gnielinski, V., 1976, "New Equations for Heat and Mass Transfer in Turbulent Pipe and Channel Flow," *Int. Chem. Engng.*, **16**, 359-368.
- Hari, S., Tu, J., and Hassan, Y.A., April 19-23, 1999, "Analysis of a Research Reactor Under ATWS Events Using the RELAP5/MOD3.2 Computer Code," *7th Int. Conference on Nuclear Engineering*, Tokyo.
- Hausen, H., 1959, "New Equations for Heat Transfer in Free or Forced Flow," *Allg. Warmetechn.* **9**, No. 4/5, 75-79.
- Hayat, M.A., 2008, *Cancer Imaging: Instrumentation and Applications Volume 2*, Elsevier Academic Press, Burlington.
- Huang, K., 1987, *Statistical Mechanics*, 2nd edition, John Wiley & Sons, New York, 3-29.
- Incropera, F.P. and DeWitt, D.P., 2002, *Introduction to Heat Transfer*, 4th edition, John Wiley & Sons, New York, 364-645.
- Kelkar, K.M., Radmehr, A., Kelly, P.J., Patankar, S.V., and Belady, C., January 11-13, 1999, "Use of Flow Network Modeling (FNM) for Enhancing the Design Process of Electronic Cooling Systems," *Proc. International Systems Packaging Symposium (ISPS)*, 58-63, San Diego.
- Kowalski, T. and Radmehr, A., 2000, "Thermal Analysis of an Electronics Enclosure: Coupling Flow Network Model (FNM) and Computational Fluid Dynamics (CFD)," *16th IEEE SEMI-THERM*, 60-67.
- Lauder, B.E. and Spalding, D.B., 1974, "The Numerical Computation of Turbulent Flows." *Computer Methods in Applied Mechanics and Engineering*, **3**, 269-289.
- Meftah, B., Zidi, T., and Bousbia-Salah, A., 2006, "Neutron Flux Optimization in Irradiation Channels at NUR Research Reactor," *Annals of Nuclear Energy*, **33**, 1164-1175.
- Meftah, B., Zidi, T., Zergoug, T., Mammou, L., Mokeddem, M.Y., and Bousbia-Salah, A., 2006 "Typical Safety Analysis Application for a Nuclear Research Reactor," *Proc. Nuclear Energy for New Europe*.
- Minichiello, A. and Belady, C., 2002, "Thermal Design Methodology for Electronic Systems," *Proceedings of the 8th InterSociety on Thermal and Thermomechanical Phenomena in Electronic Systems (ITHERM)*, 696-704.
- Minichiello, A., May 2000, "Flow Network Modeling: A Case Study in Expedient System Prototyping", *Proc. of IOTHERM 2000 Conference*, **1**, 70-77.
- Mushtaq, A., Iqbal, M., Bokhari, I.H., Mahmood, T., Mahmood, T., Ahmad, Z., and Zaman, Q., 2008, "Neutronic and Thermal Hydraulic Analysis for Production of Fission Molybdenum-99 at Pakistan Research Reactor-1," *Annals of Nuclear Energy*, **35**, 345-352.
- Orselli, R.M. and De Lemos, M.J.S., 2005, "Sudden Contraction in a Turbulent Flow with a Porous Insert," *Latin American Journal of Solids and Structures*, **2**, 269-290.

- Ozlap, C., Pinarbasi, A., Fakilar, and Sahin, B., 2007, "PIV Measurements of Flow Through a Sudden Contraction," *Flow Measurement and Instrumentation*, **18**, 121-128.
- Radmehr, A., Kelkar, K.M., Kelly, P., Patankar, S.V., and Kang, S.S., March 9-11, 1999, "Analysis of the Effect of Bypass on the Performance of Heat Sinks Using Flow Network Modeling (FNM)," *Proc. Semiconductor Thermal Measurement and Management Symposium (SEMI-THERM)*, 42-47, San Diego.
- Radmehr, A. and Patankar, S.V., 2004, "A Flow Network Analysis of a Liquid Cooling System that Incorporates Microchannel Heat Sinks," *Proceedings of the 9th InterSociety on Thermal and Thermalmechanical Phenomena in Electronic Systems (ITHERM)*, 714-721.
- Raza, W. and Kim, K., 2008, "Multiobjective Optimization of a Wire-Wrapped LMR Fuel Assembly," *Nuc. Tech.*, **162**, 45.
- Sisavath, S., Jing, X., Pain, C., and Zimmerman, R.W., 2002, "Creeping Flow Through an Axisymmetric Sudden Contraction or Expansion," *Journal of Fluids Engineering*, **124**, 273-278.
- Snelgrove, J.L., Vandegrift, G.F., and Hofman, G.L., 1997, *Development and Processing of LEU Targets for ⁹⁹Mo Production*, Argonne National Laboratory, Argonne.
- Solbrekken, G.L., Scott, J., and Allen, C., October 5-9, 2008, "Hydrodynamic Measurements In Irradiation Position For Mo-99 Production Leu Target," *Proc. of the 30th International Meeting on Reduced Enrichment for Research and Test Reactors (RETR)*, Washington DC, USA.
- Streeter, V.L., 1961, *Handbook of Fluid Dynamics*, 1st edition, McGraw-Hill, New York, 3.18-3.23.
- Table of Nuclides, National Nuclear Data Center (NNDC), <http://www.nndc.bnl.gov/chart/>, (2008).
- Tu, J.Y., 1997, "Modeling of HIFAR Thermal-Hydraulics Using RELAP5/MOD2," *Proc. Int. Cong. on Modeling and Simulation*, **2**, 972.
- Vandegrift, G.F., Koma, Y., Cols, H., Conner, C., Aase, S., Peter, M., Walker, D., Leonard, R.A., and Snelgrove, J.L., October 1-6, 2000, "Production of Mo-99 from LEU Targets Base-Side Processing," *Meeting on Reduced Enrichment for Research and Test Reactors*, Las Vegas.
- Vandegrift, G.F., Conner, C.J., Sedlet, J., and Wygmans, D.G., 1997 "Converting ⁹⁹Mo Production from High- to Low-Enriched Uranium," *American Nuclear Society 1997 Winter Meeting*, 1-3.
- Verma, N., 2002, "Use of Flow Network Modeling for the Design of an Intricate Cooling Manifold," *Proceedings of SPIE – The International Society for Optical Engineering*, 408-413.
- White, F.M., 2003, *Fluid Mechanics*, 5th edition, McGraw-Hill, New York, 176-177, 384-392.
- Williams, R.W., 1976, *Technetium-99m Production from Uranium-235 Fission*, University of Missouri-Columbia, Columbia, 1-6.
- Yeh, J.J. and Short, Jr., B.E., 2000, "Design of a Coldplate Using Flow Network Modeling (FNM)," *16th IEEE Semi-Therm Symposium*, 80-85.
- Yeoh, G.H. and Wassink, D., 2003, "Utilisation of Computational Fluid Dynamic Techniques for Design of Molybdenum Target Specifications," *9th Meeting of the International Group on Research Reactors*, Sydney.
- Zolle, I., 2007, *Technetium-99m Pharmaceuticals*, Springer, New York., 77-78.